Thesis

Using Convection-Allowing Ensembles to Understand the Predictability of Extreme Rainfall

Submitted by

Erik R. Nielsen

Department of Atmospheric Science

In partial fulfillment of the requirements

For the Degree of Master of Science

Colorado State University

Fort Collins, Colorado

Spring 2016

Master's Committee:

Advisor: Russ Schumacher

Susan van den Heever
Jorge Ramirez

Abstract

Using Convection-Allowing Ensembles to Understand the Predictability of Extreme Rainfall

The meteorological community has well established the usefulness of ensemble-based numerical weather prediction for precipitation guidance, since trusting one possible atmospheric solution can lead to, in some cases, particularly bad forecasts for precipitation guidance, owing to inherent uncertainties in precipitation processes that make deterministic prediction impractical. However, continued predictive challenges associated with intense convective rainfall has led to an increasing need to determine the most effective use of these ensemble systems in high impact, extreme precipitation events. Further, it cannot be assumed that ensembles will evolve similarly in both extreme precipitation and more benign events, due to the importance and error growth associated with convective-scale motions. This error growth associated with the chaotic nature of moist convective dynamics can also serve to limit the predictability of an extreme rainfall event (known as intrinsic predictability), in addition to predictability limits imposed by deficiencies in observing systems and numerical models (known as practical predictability). This research will focus on using a recently developed, operationally based ensemble dataset, specifically the National Oceanic and Atmospheric Administration's (NOAA) Second Generation Global Medium-Range Ensemble Reforecast Dataset (Reforecast-2), to create downscaled ensemble reforecasts of the extreme precipitation events. Some events examined during the course of this research are the inland movement of tropical storm Erin in 2007 and flooding associated with mesoscale convective vortices in Arkansas in 2010 and San Antonio, Texas in 2013.

The global reforecasts are used to force an ensemble of convection-allowing WRF-ARW numerical simulations for the purpose of evaluating ensemble-based precipitation forecasts associated with specific extreme rainfall events. Using these ensemble forecasts, we address several questions related to the practical versus the intrinsic predictability of the extreme rainfall events examined. Experiments that vary the magnitude of the perturbations to the initial and lateral boundary conditions (ICs and LBCs) reveal a seemingly proportional scaling of ensemble spread early in the simulations associated with the magnitude of the perturbation, but this scaling is not maintained throughout the simulations. Additionally, a diurnal cycle in ensemble spread growth is observed with large growth associated with afternoon convection, but the growth rate then reduced after convection dissipates the next morning rather than continuing to grow. The specific characteristics of the diurnal cycle, however, vary based upon region and flow regime. Lastly, the ensemble spread was found to be influenced by the size of the IC perturbations out to at least 48 hours. These spread evolution characteristics speak to the viability of running convection-allowing ensembles for prediction on multi-day timescales, since no saturation of the ensemble spread is seen despite extreme precipitation within the modeled time period. In addition to the overall ensemble characteristics, terrain-induced precipitation variability associated with the terrain feature known as the Balcones Escarpment, located in central Texas, is analyzed in multiple instances of heavy rainfall in San Antonio and the surrounding area. Simulations in which the Balcones Escarpment is removed reveal that when the synoptic to mesoscale forcing for heavy rainfall are in place over the Balcones Escarpment, the terrain does not directly affect the occurrence or magnitude of precipitation. It does affect the spatial distribution of the precipitation in a small but consistent way. This shift in precipitation associated with removing the Balcones

Escarpment, when compared to a WRF-ARW ensemble for the event, is smaller than shifts associated with typical atmospheric variability.

The combined results of these experiments demonstrate that downscaled ensemble NWP systems using readily available global ensemble forecasts can faithfully represent previously unresolved mesoscale features, precipitation totals, and depict ensemble-spread characteristics associated with moist convection.

Acknowledgements

This research was supported by National Science Foundation Grant AGS-1157425; National Science Foundation Graduate Research Fellowship Grant DGE-1321845, Amendment 3; the National Science Foundation Science and Technology Center for Multi-Scale Modeling of Atmospheric Processes (CMMAP), managed by Colorado State University under cooperative agreement No. AGS-04252473; and a one year American Meteorological Society Graduate Fellowship.

Access to the full model output of NOAA's Second-Generation Global Medium-Range Ensemble Reforecast Dataset (Reforcast-2) was provided by the Department of Energy (DOE). High-performance computing resources from Yellowstone (ark:/85065/d7wd3xhc) were provided by the National Center for Atmospheric Research's (NCAR) Computational and Information Systems Laboratory, which is sponsored by the National Science Foundation. North American Regional Reanalyses (NARR) were obtained from the NOAA/Physical Sciences Division, and Stage-IV analyses were provided by NCAR. Observational sounding data was provided by the University of Wyoming Department of Atmospheric Science. Flood damage estimates and reported fatalities for the extreme precipitation events examined were provided by the Storm Events Database of the National Climate Data Center (NCDC).

I would like to express my thanks to the members of my masters thesis committee, Dr. Sue van den Heever and Dr. Jorge Ramirez, for their review of this work and many helpful suggestions. I would like to especially thank my advisor Dr. Russ Schumacher for his support in this research, as well as his unwavering willingness to help with many conceptual and technical challenges that have occurred along the way.

Thanks to the members, both past and present, of the Schumacher research group – Greg Herman, John Peters, Robert Tournay, Stacey Hitchcock, Vanessa Vincente, Matt Palaus, Nathan Kelly, Sam Childs, and Peter Goble – for valuable discussion, motivation, and technical assistance throughout this research. I also would like to profusely thank my family and friends for their constant encouragement and willingness to listen and deal with the various aspects of graduate school life. Further, I would like to express thanks to past research advisors, including Jamie R. Rhome and Dr. Don Conlee, for helping shape my thought process and research acumen. Finally, I would like to thank Timothy Theodore Duncan, Gregory Popovich, A-Vac, and J. J. Jr. for providing continued distraction, improved mental health, and many stories.

This thesis is typset in LaTeX using a document class designed by Leif Anderson.

Table of Contents

List of Tables

LIST OF FIGURES

CHAPTER 1

Introduction

In many parts of the world, including the United States, flooding continues to pose a serious threat to human life, property, and infrastructure. Flooding is defined by the National Weather Service (NWS) as "any high flow, overflow, or inundation by water which causes or threatens damage," while a flash flood is defined as "a rapid and extreme flow of high water into a normally dry area, or a rapid water level rise in a stream or creek above a predetermined flood level, beginning within six hours of the causative event (e.g., intense rainfall, dam failure, ice jam)" (NOAA cited 2015a). Additionally, flooding is usually a longer duration event (i.e., it may last days or weeks) than flash flooding. The occurrence of floods and flash floods in any particular region is not solely dependent upon the rainfall amount or rate, but also local hydrologic factors, such as topography, catchment size, soil type, and soil moisture. Furthermore, storm motion characteristics play a central role in influencing the rainfall accumulation totals. The forecasting of floods is a complicated interplay between hydrologic and meteorological forcing, where not only the occurrence of an event, but also the magnitude, are essential to evaluate potential impacts (e.g., Doswell et al. 1996).

During the time period from 1959 to 2005, Ashley and Ashley (2008) found that 4586 flood-related fatalities occurred in the continental United States with the most fatal events being flash flood or tropical cyclone related. The study also did not find any significant decrease in flood-related fatalities or risk over the 47-year period, despite modern advancements in communication and flood mitigation. Compared to other weather-related threats over this time period, only flood-related fatalities failed to show improvement even with the number of flood events per year staying relatively constant. This underscores the danger that floods, especially flash floods, still pose to people across the United States.

The accurate prediction of these extreme rainfall events remains a significant challenge for the weather forecast community. Since their advent in the early to mid 1990s, the meteorological forecast community has established the usefulness of ensemble-based numerical weather prediction (NWP) for precipitation forecasting. The reliance of operational forecasters on these systems for precipitation guidance has led to an increasing need to determine the most effective use of ensemble prediction systems in high impact, flooding events. Recent efforts have led to development of global medium range ensemble reforecast datasets based upon operational NWP models, which provide a framework to investigate a variety of ensemble related research questions, including those related to extreme rainfall.

In the following chapters, the predictability of extreme precipitation events are examined in convection-allowing NWP ensemble forecasts. The general ensemble precipitation spread evolution will be examined for several recent flooding events that have occurred in the United States. This will speak to the forecast viability of using convection-allowing ensemble forecast systems to predict extreme rainfall on multi-day timescales. Additionally, a case study on terrain-induced precipitation variability will be carried out on several instances of flooding on a feature located in central Texas known as the Balcones Escarpment. The sum of these results will reflect the ability of convection-allowing ensembles to accurately reproduce mesoscale features previously unresolved by ensembles, observed precipitation totals, and illustrate spread characteristics associated with moist convection.

CHAPTER 2

Background and Motivation

2.1. Extreme Precipitation and Flash Flooding

Despite modern flood mitigation strategies and increased awareness, flash flooding still produces the most deaths on an annual basis from any convective storm related hazard in the United States (e.g., Doswell et al. 1996; Ashley and Ashley 2008). Unlike tornado forecasting where determination of event occurrence is an adequate forecast of danger, flash flood forecasting is more quantitative where the occurrence *and* magnitude of the event must be predicted in order to differentiate between benign and life-threatening rainfall (Doswell et al. 1996). The accurate prediction of the magnitude of the rainfall, known as quantitative precipitation forecasting (QPF), is still an exceptional challenge for numerical weather prediction models and human forecasters (e.g., Fritsch and Carbone 2004; Novak et al. 2011). Further compounding the forecasting complexity, the local and large-scale hydrology, areal topography, regional land use, and preceding soil moisture characteristics all play an important role in the evolution of flooding scenarios (Funk 2006). Thus, a flash flooding event can be thought of as a dependent interaction between a specific meteorological event and the hydrologic characteristics of the affected area.

From a purely meteorological perspective, large precipitation accumulations over a region is an essential ingredient for flash flooding. For large precipitation accumulations to occur, it has been found that high rain rates must occur over an extended period of time (e.g., Doswell 1994; Doswell et al. 1996). The total precipitation that falls at any point on earth,

P, can simply be expressed as:

$$P = \bar{R}D \tag{1}$$

where $\bar{R}$ is the average rainfall rate and D is the rainfall duration (Eqn.1). While the average rainfall rate, $\bar{R}$, is useful for post-event analysis of the rainfall, it does not illustrate the ingredients needed for high rain rates. The instantaneous rainfall rate, R, which can be decomposed into separate illustrative elements, is proportional to the vertical moisture flux into the thunderstorm (i.e., the simplifying assumption here is the more water vapor flux into the storm, the higher the precipitation rate) (Doswell et al. 1996). R can be expressed as:

$$R = Ewq \tag{2}$$

where E is the precipitation efficiency, q is the water vapor mixing ratio of the rising air, and w is the ascent rate (Eqn. 2). The precipitation efficiency, E, is a proportionality term relating water vapor flux to rainfall rate, which is not discussed in detail here (for explicit discussion see the Appendix in Doswell et al. (1996)). The duration of a rain event, D, is dependent on the size of the rainfall area along the motion vector and the speed of the motion (Doswell et al. 1996). While many storm types can produce high rainfall accumulations, two low predictability, flood producing event types of particular interest to this study will be discussed in detail below, as well as the characteristics of extreme rainfall in the United States.

2.1.1. Characteristics of United States Extreme Rainfall. The characteristics and temporal variability of extreme rainfall in the United States has been examined

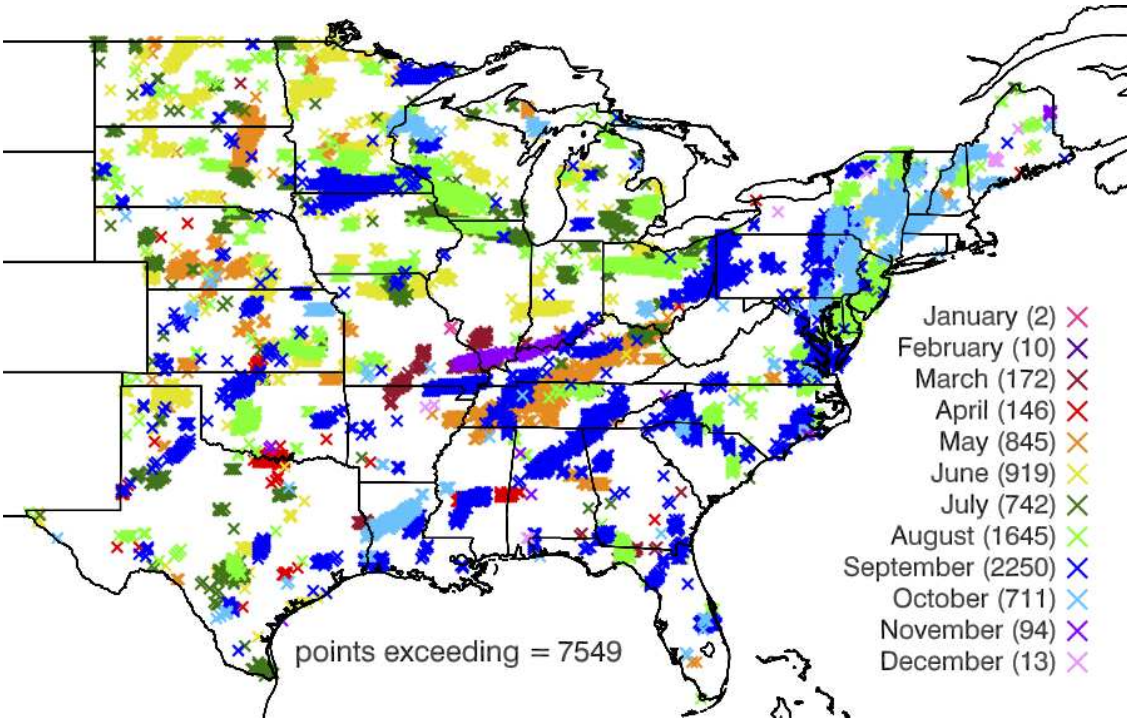

FIGURE 2.1. Spatial distribution of points for 50 year, 24 hr threshold during 2002-2011. There are 7549 total points. The color of the crisscross (X) represents the month during which the point occurred. The total number of points in each month is displayed in the legend. From Stevenson and Schumacher (2014) Fig. 10.

in several different studies, including more recently in Stevenson and Schumacher (2014) as a continuation of the work done in Schumacher and Johnson (2006). Stevenson and Schumacher (2014) used the Stage-IV gridded precipitation analysis (Lin and Mitchell 2005) to identify precipitation that exceeded the 50 and 100 year recurrence intervals for the 1-hour (hr), 6-hr, and 24-hr accumulation periods for 37 states east of the Rocky Mountains. The study showed that the geographic and seasonal pattern of the identified 50 and 100 year events were very similar, and that the geographic uniformity of events across the United States increased from the 1-hr to 24-hr rainfall accumulation thresholds (Fig. 2.1). Over the ten year period analyzed, 93 (52) events were identified to occur per year for the 50 year (100 year) recurrence interval at the 1-hr duration, 87 (55) events at the 6-hr duration, and 46 (29) at the 24-hr duration. The exact month that saw the maximum in event occurrence varied by region of the United States. The events exceeding any specific recurrence interval (e.g., 1-hr, 6-hr, and 24-hr) at the 24-hr duration had more individual points that reached the threshold than other durations, which underscores the importance of organized precipitation (Fig. 2.1). Tropical cyclones were responsible for more points exceeding a recurrence interval at the 24-hr duration than any other storm type with a maximum frequency in September, corresponding to the peak in Atlantic tropical cyclone activity. However, mesoscale convective systems (MCSs) were responsible for majority of extreme rainfall events that exceeded the 24-hr duration at the 100 year recurrence interval. Most of the events, over all three accumulation periods, occurred in the summer months (e.g., Fritsch et al. 1986), which underscores the importance of warm season precipitation forecasting in predicting extreme rainfall events. Furthermore and perhaps most dangerously, the diurnal maximum for events that exceeded the hourly 50 year recurrence interval occurred in the evening to overnight hours (1600-0000 LST).

2.1.2. Quasi-Stationary Mesoscale Convective Systems. In the United States during the warm season, the majority of heavy rainfall and flash flood events are the result of mesoscale convective systems (e.g., Bosart and Sanders 1981; Maddox and Grice 1986; Fritsch et al. 1986; Junker et al. 1999; Moore et al. 2003; Schumacher and Johnson 2005, 2006). Most MCSs occur in relatively weakly forced synoptic environments with various possible forcing mechanisms for initiation, organization, and maintenance. Linear MCSs that occur in the warm sector are associated with a surface boundary, usually a stationary or warm front, and a low-level jet providing moisture and enhanced convective activity (Fig. 2.2a) (e.g., Parker and Johnson 2000; Schumacher and Johnson 2005). Further, the nocturnal low-level jet is an important feature that determines the location and intensity of the rainfall that falls in the warm season over the central United States (e.g., Tuttle and

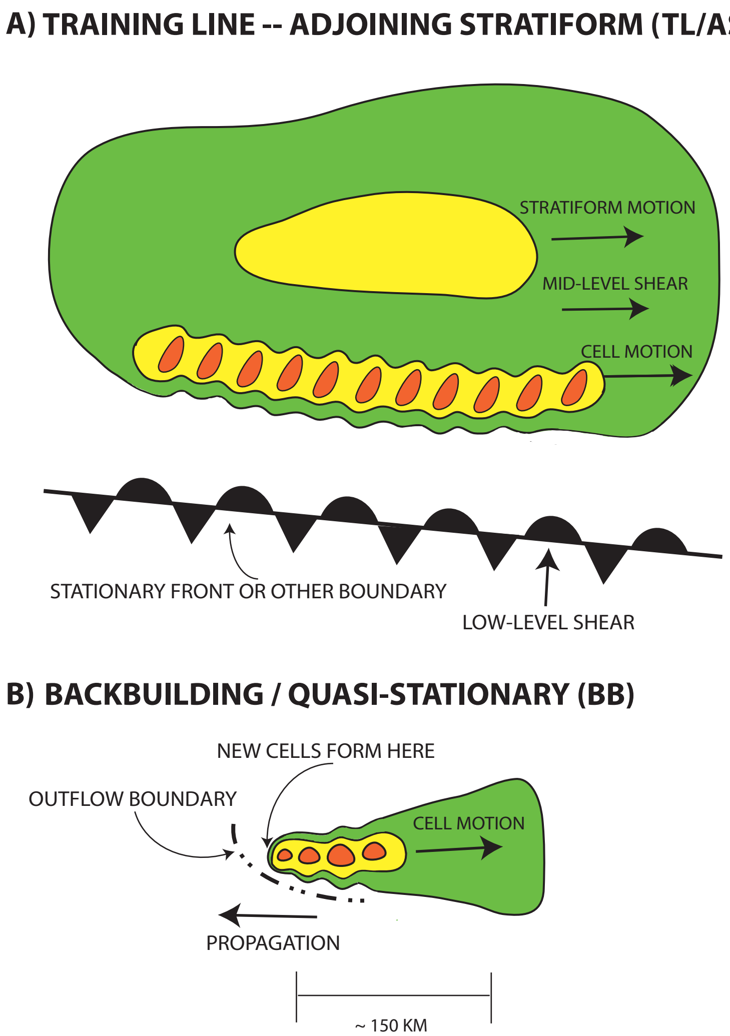

FIGURE 2.2. Schematic diagram of the radar-observed features of the (a) Training Line/Adjoined Stratiform (TL/AS) and (b) Backbuilding (BB) patterns of extreme-rain-producing MCSs. Contours (and shading) represent approximate radar reflectivity values of 20, 40, and 50 dBZ. In (a), the low-level and midlevel shear arrows refer to the shear in the surface-to-925-hPa and 92—500-hPa layers, respectively. The dash—dot line in (b) represents an outflow boundary; such boundaries were observed in many of the BB MCS cases. The length scale at the bottom is approximate and can vary substantially, especially for BB systems, depending on the number of mature convective cells present at a given time. From Schumacher and Johnson (2005) Fig. 3.

Davis 2006). The intensity of the rainfall increases with the strength of the lower-level jet through enhanced lower-level convergence, iscentropic lifting, frontogenesis, and moisture advection. Schumacher and Johnson (2009) found that the thermodynamic environment of extreme rainfall events is characterized by a very moist boundary layer, moderate convective available potential energy (CAPE) and little convective inhibition (CIN) for elevated parcels, and high moisture content through the vertical column (Fig. 2.3).

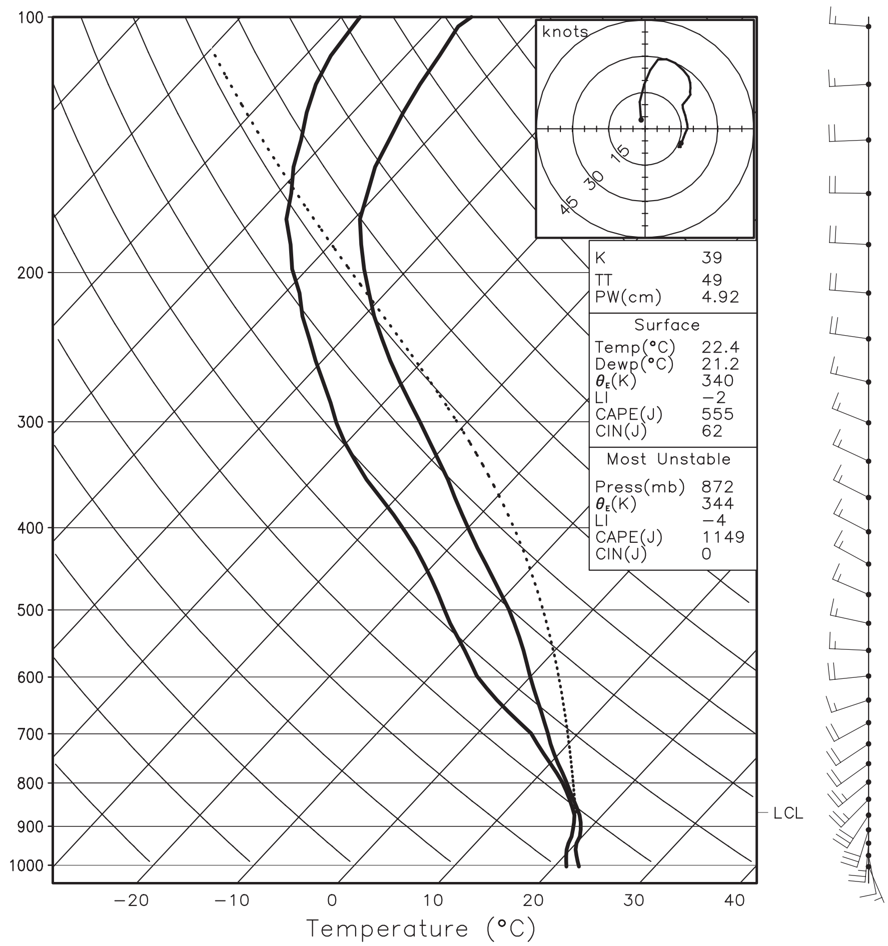

FIGURE 2.3. Composite skew T-log$p$ diagram for the extreme rainfall environment. The parcel path for the parcel with the highest θ_e in the lowest 3 km is shown by the dotted line. From Schumacher and Johnson (2009) Fig. 14.

The overall system motion and convective organization of any MCS type can lead to heavy rainfall accumulations and "echo training." Such quasi-stationary convective systems have been found to be particularly important producers of flash floods (e.g., Chappell 1986; Doswell et al. 1996), wherein convective cells producing heavy instantaneous rainfall rates

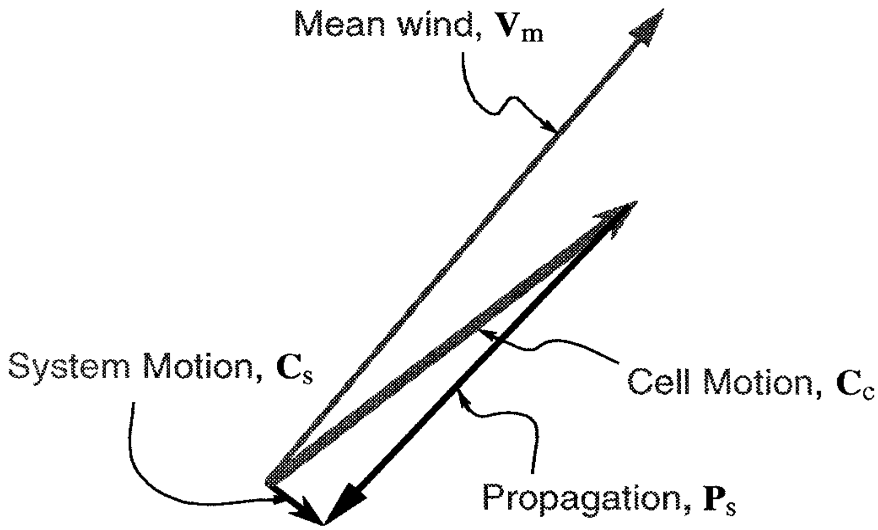

FIGURE 2.4. Diagram depicting near cancellation between cell motion and propagation. From Doswell et al. (1996) Fig. 4.

move over the same location repeatedly. Quasi-stationary or back building MCSs (Fig. 2.2b) can be particularly efficient at maximizing the accumulated precipitation that falls over a given area and increase the risk of devastating flooding (e.g., Bluestein and Jain 1985; Chappell 1986; Doswell 1994; Doswell et al. 1996; Schumacher and Johnson 2005). These storms appear stationary to a local ground observer because the new cell propagation is opposite of the cell motion vector (Fig. 2.4) (e.g., Chappell 1986; Corfidi et al. 1996; Corfidi 2003; Schumacher and Johnson 2005). Additionally, some quasi-stationary MCSs are not associated with an obvious surface boundary to initiate and maintain convection, but rather by a midlevel mesoscale convective vortex (MCV; Raymond and Jiang 1990; Bartels and Maddox 1991; Trier et al. 2000a,b; Schumacher and Johnson 2008, 2009). MCSs, especially MCVs, can be particularly challenging to forecast, since the forcing mechanisms behind the rainfall are weak, compared to the overall flow, or are not completely obvious to forecasters and/or the numerical model. While MCSs more commonly produce extreme precipitation than other storm types, flash flooding can still occur year round from other storm categories including extra-tropical cyclones, isolated convective cells, or landfalling tropical cyclones. However, from a forecasting standpoint, the prediction of warm season heavy rain events, such as the types described here, remains a significant challenge to operational forecasters (e.g., Fritsch and Carbone 2004).

2.1.3. Predecessor Rain Events associated with Tropical Cyclones. Tropical cyclones are well known as heavy rain produces in a wide range of synoptic conditions and can directly lead to inland flash flooding from the rainfall contained within the identifiable vortex. In fact for a period in the late 20th century, inland freshwater flooding was the leading cause of death associated with tropical cyclones (Rappaport 2000); however, storm surge has become the leading cause in recent years (Rappaport 2014), which is believed to be caused by increased (strong) tropical cyclone activity and lack of clear storm surge threat communication. Additional inland flash flooding scenarios can occur when the tropical cyclone interacts with terrain or pre-existing baroclinic zones (e.g., Srock and Bosart 2009). While the rainfall associated with the tropical cyclone vortex is the most well known, recent research has analyzed regions of heavy rainfall that occur in the area but are separated by a large distance (∼1000 km) from recurving tropical cyclones. These rain events, which can produce as much if not more rainfall than the identifiable vortex, are known as predecessor rain events (PREs) (e.g., Cote 2007; Galarneau et al. 2010; Schumacher et al. 2011; Schumacher and Galarneau 2012; Moore et al. 2013).

PREs are caused when deep tropical moisture is transported poleward of the tropical cyclone into an area where synoptic scale forcing is conducive for rainfall. PREs most often occur in the equatorward entrance region of a anticyclonically curved upper level jet streak where quasigeostrophic forcing for ascent is present (e.g., Uccellini and Johnson 1979). The majority of the cases identified in Galarneau et al. (2010) also had a east-west oriented, nearly-stationary baroclinic zone located under the upper-level jet streak. Additionally, southerly moist flow ahead of the recurving tropical cyclone incident on this baroclinic zone leads to enhanced ascent, through pronounced warm air advection and frontogenesis (Fig. 2.5). This upper and lower level forcing for ascent combine with a supply of deep tropical moisture to create a region with all the necessary ingredients for heavy rainfall described in Doswell et al. (1996).

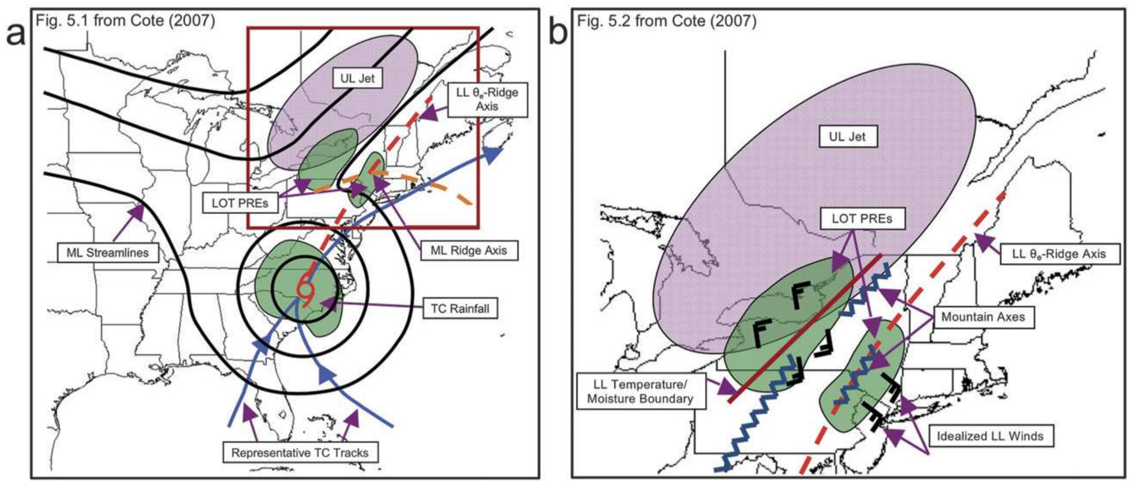

FIGURE 2.5. (a) Conceptual model of the synoptic scale environment associated with PREs in advance of tropical cyclones, revised and updated from Bosart and Carr (1978). Position of tropical cyclone is given by the tropical storm symbol. Representative tropical cyclone tracks are marked by solid blue arrows. Low-level (LL) features are representative of the 925-hPa level, midlevel (ML) features are representative of the 700-hPa level, and upper-level (UL) features are representative of the 200-hPa level. (b) Boxed region from (a) indicating the area of the mesoscale and physiographic conceptual model. [From Fig. 24 Galarneau et al. (2010), Reproduced from Figs. 5.1 and 5.2 in Cote (2007).]

The PREs associated with tropical cyclones Erin (2007) and Ike (2008) have be studied in detail to investigate the impact of the tropical moisture on rainfall totals and the predictability of the events (e.g., Schumacher et al. 2011; Schumacher and Galarneau 2012). The moisture plume originating from Erin was found by Schumacher et al. (2011) to double the maximum modeled precipitation amount and increase by 25% the area-integrated precipitation in the associated PRE in the northern Great Plains and southern Great Lakes that produced a record flood event. Additionally, the moisture plume ahead of Erin increased the total precipitable water by almost 20 mm (Fig. 2.6). However, the moisture increase in PRE ahead of Ike was present but not as identifiable, due to various interacting moisture sources. Ensemble forecasts of these two cases handled the moisture transport magnitude differently and varied the amount of recurving in the tropical cyclone tracks. The ensemble forecast differences illustrate the difficultly in predicting precipitation accumulations associated with PREs. Even if the tropical cyclone track and moisture transport are correctly represented and the lower and upper level forcing for ascent are correctly resolved, the location and timing of the event must still be accurately represented. Thus, predicting the extreme rainfall associated with PREs will remain difficult and involve the use of NWP ensembles to illustrate the many possible atmospheric solutions (e.g., Schumacher and Galarneau 2012).

2.1.4. Hydrology. If the occurrence and magnitude of heavy precipitation can be forecasted at useful lead times, proper representation of the hydrologic and hydraulic processes of the affected area is needed to determine the proportion of rainfall that runs off the surface. Static catchment characteristics including land use, permeability, soil type, and topography, as well as time dependent fields, such as soil moisture and infiltration capacity, all influence the runoff potential of a specific basin (e.g., Davis 2001). This complicates the physical information needed and increases the number of approaches, both complex and simple, available to make an accurate flash flood forecast (Fig. 2.7).

Further compacting the forecast aspects of flash flood prediction, a short but more intense rainfall event, all else being equal, will usually produce more runoff than an event producing the same amount of precipitation accumulation over a longer period (e.g., Sweeney 1992).

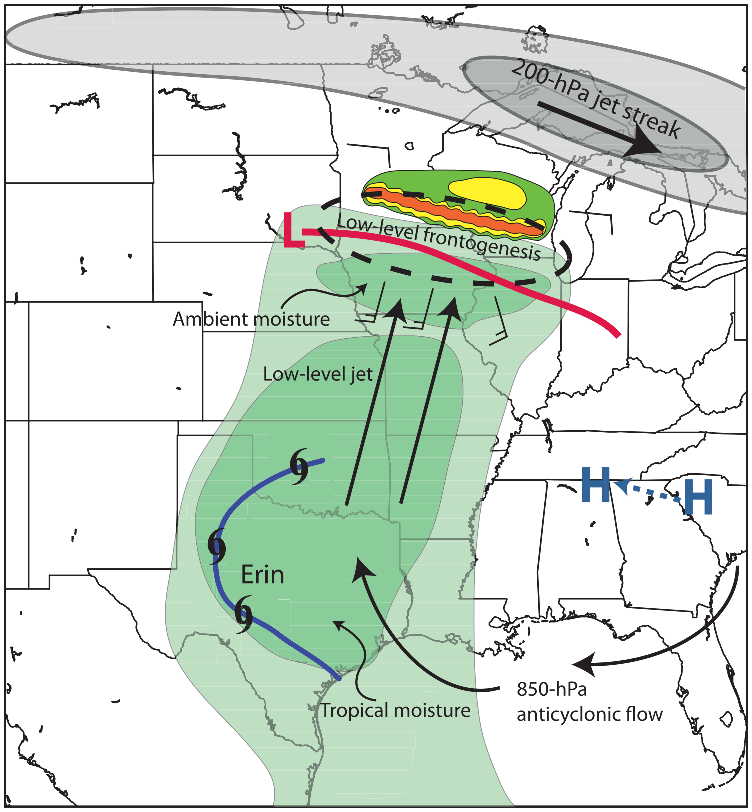

Figure 2.6. Schematic diagram showing the primary processes in the TC Erin PRE, and generally representative of a typical PRE occurring under an anticyclonically curved upper-level jet (based on the findings of GBS10). The track of TC Erin and its remnants is shown by the thick blue curve, with the position at 1200 UTC 17 Aug, 18 Aug, and 19 Aug 2007 shown by the TC symbols. The 700-hPa anticyclone, and its movement toward the west-northwest during the event, is shown by the "H" symbols. The surface low pressure center and baroclinic zone are shown by the red "L" and red line, respectively, with the associated low-level frontogenesis maximum outlined in the dashed black line. The 200-hPa isotachs of approximately 30 and 50 m s^{-1} are in gray shading. The 850-hPa flow direction is shown by the black arrows, and some representative surface wind barbs are also shown. Areas of precipitable water greater than 50 (55) mm are shaded in light green (darker green), respectively, and the radar-indicated structure of the extreme-rain-producing MCS is contoured at approximately 20, 40, and 50 dBZ. From Fig. 2 of Schumacher et al. (2011).

Small catchments on the order of a couple hundred square kilometers are more prone to flash floods than larger basins because of quick rainfall-runoff responses, due to the small catchment size, from increased influence of steep terrain, soil moisture, burn scars, and land

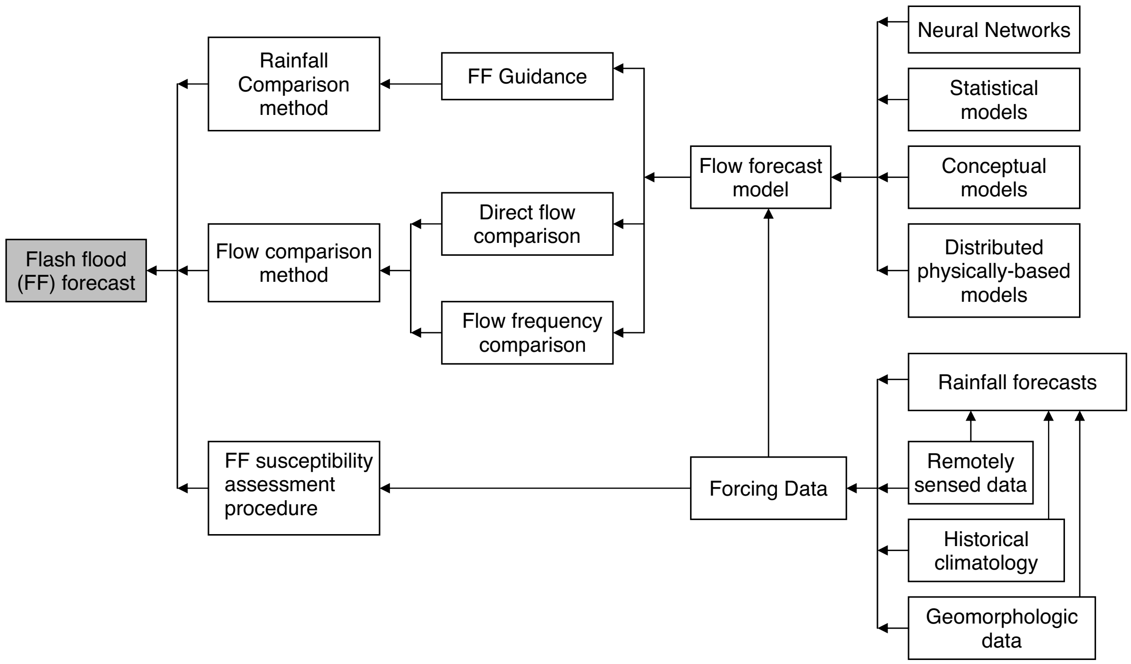

Figure 2.7. Different approaches available of making a flash flood forecast. From Hapuarachchi et al. (2011) Fig. 5.

use (e.g., Kelsch 2001). It has been suggested that in the United States catchments below about 100 square miles are most prone to flash flooding and are often poorly gauged for rainfall and soil moisture observations (Davis and Jendrowski 1998; Hapuarachchi et al. 2011). Urban areas can further enhance rainfall-runoff in catchments and increase flash flooding potential due to large impervious areas, and no hydrologic model, as of yet, has been developed that completely captures these effects (e.g., Hapuarachchi et al. 2011). While the hydrologic processes associated with flash flooding are not dealt with directly in this study, it is important to understand that accurate hydrologic and meteorological prediction is needed to completely predict flash flooding, which poses considerable challenges in both aspects (e.g., Doswell et al. 1996). The remainder of this study will focus on the predictability of the meteorological aspects of flash flood forecasting with some consideration given to the hydrology in the Balcones Escarpment case study.

Throughout the operational weather forecast community, NWP models provide the basis for precipitation forecasts in both low and high impact events. One method of NWP, know as a deterministic modeling, takes an initial representation of the atmospheric state and creates, through the integration of the atmospheric equations of motion and use of physical parameterizations, a single forecast of the future atmospheric state. The accuracy of the deterministic NWP forecast is tied to how well the initial atmospheric state, often referred to as the model initial conditions (ICs), is represented. Generally, it is believe that the more accurate the initial representation of the atmosphere, in principle, the more accurate the resulting forecast will be at longer lead times. One way that the initial atmospheric state can be improved is through more complete and accurate atmospheric observing systems. However, due to the chaotic nature of the atmospheric system, theoretical limits of the predictability of different atmospheric scales of motion, first examined by Thompson (1957); Lorenz (1963, 1969), exist. More specifically, Lorenz (1969) presented the notion that forecast errors stem from unobservable small scale atmospheric circulations. Any error in these small scale atmospheric motions can rapidly grow upscale and reduce the lead time over which a deterministic forecast is valid. Furthermore, this implies that as smaller atmospheric scales are resolved by an NWP model, the faster the forecast errors propagate upscale. This chaotic upscale model error growth creates a limit to the atmospheric predictability for deterministic forecasts where a perfect forecast is not possible. The notion of upscale error growth creating a limit on atmospheric predictability has since been more precisely investigated (e.g., Leith 1971; Leith and Kraichnan 1972; Métais and Lesieur 1986) and gained wide acceptance in the meteorology community. However, it has also been noted that the results of Lorenz (1969) could also imply that error growth from very small scales can be masked by downscale error growth from larger scales and not have any substantial impact on the practical limit of predictability (e.g., Durran and Gingrich 2014).

Predictability as applied to NWP can be broken down into two distinct, but instructive, parts: *practical predictability* and *intrinsic predictability*. Practical predictability can be thought of as how well a model can predict future atmospheric states based upon the procedures currently available in NWP. Intrinsic predictability is defined as "the extent to which prediction is possible if an optimum procedure is used" (Lorenz 1969; Zhang et al. 2006; Melhauser and Zhang 2012). Practical predictability is limited by developmental uncertainties in the creation of the atmospheric ICs and NWP model architecture that are usually identifiable (Lorenz 1996). While, intrinsic predictability is the limit of predictability that is reached with an almost perfect knowledge of the atmospheric ICs and nearly perfect NWP model. The intrinsic predictability limit cannot be overcome due to the chaotic nature of the atmosphere described in Lorenz (1969). Additionally, the practical and intrinsic predictability of the atmosphere are dependent on the scale of the motion and the specific atmospheric flow patterns that are in place (Lorenz 1996; Zhang et al. 2006).

The prediction of precipitation in NWP deterministic forecasts can be particularly challenging due to the small-scale, chaotic nature of deep moist convection. Most processes of interest that govern extreme rainfall, especially in the warm season, reside in mesoscale motions of the atmosphere. Studies conducted of upscale model spread growth in both the cold and warm season found that small scale, non-linear errors grow quickly upscale due to moist convective processes. This error growth limits the mesoscale predictability and potential forecast accuracy of deterministic NWP models in intense precipitation producing events (Zhang et al. 2002, 2003, 2006, 2007). Given that deterministic forecasts have limited predictability and skill for mesoscale features, convection, and, accordingly, precipitation accumulations (e.g., Zhang et al. 2003), trusting the output of one possible atmospheric state from a deterministic model can, in some cases, lead to particularly bad forecasts. However, NWP ensembles can be used to overcome some of these predictability problems and increase precipitation forecast accuracy. NWP ensembles are forecast systems that are composed of many individual deterministic forecasts that are created by varying model ICs and/or model physics. Ensemble NWP systems have their roots in stochastic dynamic prediction, which was developed as an attempt to deal with the inability to observe the entirety of the atmosphere, which limited forecast accuracy (Lewis 2005, and citations within). Ensembles have regularly been used for extended range forecasts (e.g., Molteni et al. 1996), but also have been shown to have utility on a one to two day lead time (e.g., Du et al. 1997; Hamill et al. 2000). Studies have shown that coarse resolution ensembles, on the order of tens of kilometers, can increases QPF predictive skill in the cold season, but do not perform well in the warm season (e.g., Du et al. 1997; Mullen and Buizza 2001; Hamill et al. 2008). Schumacher and Davis (2010) explored how accurate precipitation forecasts from the European Center for Medium-Range Weather Forecasts (ECMWF) Ensemble Prediction System (EPS) were in nine cases of extreme rainfall between 2007 and 2008. It was found that skillful precipitation forecasts were provided at five day lead timescales for flooding events associated with tropical and extratropical cyclones. However, warm season events associated with mesoscale interactions and convective systems were not well predicted, showing the need for continued ensemble development and QPF improvement.

The size and grid spacing of EPSs have long been limited by available computing power, which has restricted ensembles to a more coarse model resolution than desired. Fortunately, modern advancements in computing have made it possible to decrease grid spacing to the order of 4 km. Grid spacing on the order of 4 km has been shown to adequately resolve convective systems, but not the motions of individual convective cells (e.g., Bryan et al. 2003), thus model configurations with horizontal grid spacing from 1-5 km are commonly referred to as "convection allowing" rather than truly "convection resolving." Further, since convection allowing grid spacings explicitly represent convection, no cumulus parameterization is needed within the model. The resolving of smaller scales of motion in convection allowing ensembles should lead to increased ensemble spread growth rates that feedback from the small to larger scales (e.g., Lorenz 1969). Ensemble spread can be conceptually thought of as a measure of the envelope of possible atmospheric states encompassed by the members of the EPS. The temporal evolution of ensemble spread can be used to evaluate the propagation of model errors through the ensemble, to evaluate the predictability and skill of forecasted events (e.g., Grimit and Mass 2007), and to test the viability of the ensemble forecasts through time. The best way to design and implement convective allowing ensembles is still a topic of active research. Due to the resolution of smaller scale motions in convection permitting ensembles, thorough examination of the ensemble spread characteristics is needed to test the viability of the prediction method.

Studies have shown that small (∼5 member) convection allowing ensembles often produce more accurate forecasts of extreme precipitation than larger (∼15 member) ensembles that do not explicitly allow convection (∼20 km) (e.g., Clark et al. 2009). Clark et al. (2010) found that spread growth rates were higher in 4 km grid spacing convection allowing ensembles with mixed physics and varied ICs for mass related and all low-level fields when compared to a similar ensemble with 20 km grid spacing. This was found to be true even though the 20 km ensemble has an additional source of model uncertainty with the use of the convective parameterization, implying that the increased model resolution has a larger impact on the model spread than the convective parameterization. Further analysis showed that the 4 km ensemble had better statistical consistency of the spread-skill relationship on a two day time scale in the mass related fields, due to larger model spread and less error (Clark et al. 2010). This implies increased model dispersion and correction of the underdispersive tendencies of the analyzed 20 km ensemble (e.g., Hamill 2001). It should be noted that increased ensemble spread does not necessarily imply increased ensemble predictive skill. Additionally, Clark et al. (2011) found that convective allowing ensembles with relatively few members (3-9) produced average probabilistic QPF forecasts that were statically similar to comparable ensembles with more members (up to 17), which means adding additional ensemble members may not always add further accuracy to the precipitation forecasts. However, the less under-dispersive the EPS, the more members it takes to reach a point of diminishing returns of the ensemble size. Other studies not mentioned here have also shown that convection allowing ensembles can serve as a viable forecast tool (e.g., Gebhardt et al. 2008; Schwartz et al. 2010) and have value over coarser ensembles in convectively active flow regimes (e.g., Kain et al. 2013). Convection allowing EPS systems are currently being run on a semi-regular basis for research and non-operational forecasting purposes. The Center for Analysis and Prediction of Storms (CAPS) at the University of Oklahoma has run, at various times, a 10-member limited area convection-allowing (4 km) EPS (Xue and Coauthors 2007, 2010, 2011), which is a mixed physics ensemble with ICs and LBCs taken from the National Centers for Environmental Prediction (NCEP) Short Range Ensemble Forecast (SREF; Du et al. 2006, 2009) members. Additionally, the National Center for Atmospheric Research (NCAR) has been running since Spring 2015, a 10-member limited area convection-allowing (3 km) EPS generated from continuously cycling mesoscale ensemble Kalman filter analyses (Schwartz et al. 2015). Furthermore, the positive reaction and significant use of the NCAR ensemble makes Schwartz et al. (2015) note the importance of accelerating convection-allowing EPS research and development.

The dispersion of limited-area ensemble forecasts is of particular importance to ensure that the range of possible solutions produced by the EPS contains a representation of the verifying analysis. In other words, the range of possible atmospheric states produced by the ensemble members of the EPS need to correctly represent the amount of uncertainty in the forecast. Producing enough member dispersion in convection-allowing EPS design remains challenging. While explicitly allowing convection increases the dispersion of the EPS over convection parameterization (e.g., Hamill 2001), limited-area convection allowing ensembles still can lack sufficient ensemble spread (e.g., Schwartz et al. 2014). One possible continued cause for underdispersive tendencies in these EPS systems is coarse LBCs (e.g., Nutter et al. 2004a). The coarse LBCs for each member that are imposed on the higher-resolution grid do not contain variations on the convection-allowing (or smaller) scales. Since small-scale errors have been shown to grow faster than large-scale errors (e.g., Lorenz 1969; Zhang et al. 2003), the reduction of these initial errors on these scales by the coarse LBCs would reduce model spread growth and dispersion. This loss of dispersion is more pronounced on smaller limited-are grid because the atmospheric features are more quickly advected through the domain (e.g., Nutter et al. 2004a). Several methods have been proposed to introduce additional small scale error growth to increase the dispersion of convection-allowing limited area EPSs. Some of these techniques include stochastic physics (e.g., Berner et al. 2011; Bouttier et al. 2012), multiphysics ensembles (e.g., Clark et al. 2010; Berner et al. 2011; Gebhardt et al. 2011), and perturbed LBCs (e.g., Nutter et al. 2004a,b; Vié et al. 2011).

While the increased resolution of ensembles to explicitly represent convection has shown to have promising future implications, the smaller resolved scales of motion can lead to forecast issues relating to practical and intrinsic predictability. For a bowing mesoscale convective system on 9-10 June 2003, Melhauser and Zhang (2012) found, despite the realistic ICs for a convection allowing ensemble, members diverged into two different storm modes. This divergence of the ensemble solutions into two different storm modes shows the dependence of each simulation on the flow regime. Further, experiments linearly reducing the ensemble perturbation for the two dominate flow regimes revealed a bifurcation point in the forecasts where a slight difference in the IC perturbation in either direction favors one storm mode or the other. The case described in Melhauser and Zhang (2012) is theorized to have approached its limit of practical predictability, due to the presence of the bifurcation in the ensemble member forecasts.

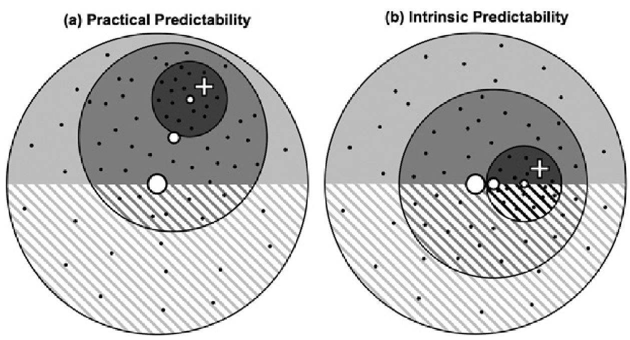

FIGURE 2.8. Idealized schematic illustrating the reduction of initial condition error by reducing the ensemble spread highlighting the (a) practical predictability representative of the 9—10 Jun 2003 squall line and bow echo and (b) intrinsic predictability representative of a theoretical ensemble forecast with the ensemble forecast having equally favorable solutions. Solid shading—flow regime 1; striped pattern—flow regime 2; black dots—ensemble members; white dots—ensemble mean; white cross—forecast truth. The line between the solid pattern (top of large circle) and striped pattern (bottom of large circle) represents the bifurcation point. The nested small circles and associated white dots represent the reduction of ensemble initial condition error. [From Fig. 18 Melhauser and Zhang (2012)]

If the error in the ensemble initial conditions is continually reduced for a case where the predictability is high (i.e., one flow regime is favored in the ensemble solutions, such as a squall line), continued improvement will be made in the practical predictability and the overall ensemble forecast (Fig. 2.8a). However, if the predictability of a specific event is low (i.e., multiple flow regimes are equally likely, such as the 9-10 June 2003 case), continued improvement of the ICs will produce both good and poor solutions on either side of the bifurcation point (Fig. 2.8b) (Melhauser and Zhang 2012). In other words, the amount in which the practical predictability can be improved and the limit of intrinsic predictability are both highly flow and forecast dependent. It is possible that in some cases, the use of convection allowing ensembles may approach the limit of intrinsic predictability, due to chaotic nature of moist convection (Melhauser and Zhang 2012).

The goal of of the ensemble predictability experiments presented in this study will be to expand the scientific knowledge on how the spread of a convection allowing ensemble evolves over time for extreme precipitation events in the United States.

2.3. Terrain Induced Variability of Extreme Precipitation

In addition to the variability associated with uncertainty in atmospheric conditions, the presence of complex terrain in the forecast area adds further uncertainty to the prediction of convection initiation, maintenance, and total precipitation accumulation. Several devastating flooding events, in some cases with little lead time (e.g., Gruntfest 1977), have and will continue to occur in mountainous areas (e.g., Maddox et al. 1978; Gochis et al. 2014) and regions with terrain features of lesser vertical extent (e.g., NWS 1999). Complex terrain can create and/or modify atmospheric motions on scales below the resolution of current NWP models. The modification of these small scales of motion can create localized regions of favorable and non-favorable development of different storm types (e.g., Soderholm et al. 2014). Additionally, the classification and prediction of stratiform and convective rainfall types over complex terrain is not as simple as over flat land. Shallow convection can be found embedded in stratiform precipitation and might be required to produce high rainfall rates that can occur in what at first seem to be stratiform events (e.g., Smith 1982). The development of cellular convection in mountainous regions is dependent not just on the environmental instability, but also the environmental wind shear, terrain width perpendicular to the upstream flow, in cloud residence time of parcels, and the depth of any unstable cap cloud (e.g., Kirshbaum and Durran 2004). The increased complexity of predicting the nature of convection and the increased hydrologic propensity for flooding (see section 2.1.4) in complex terrain make accurate QPF forecasts essential to protecting life and property. However, the exact process governing precipitation vary by terrain feature, although some processes associated with convection initiation and maintenance can be applied to most regions (see below paragraph). The Balcones Escarpment in central Texas is a highly populated, flood prone area that presents a chance to evaluate the precipitation variability associated with the terrain feature compared to that associated with the uncertainty of the atmospheric forcing mechanisms.

A significant amount of research exits that investigates the effects or orography on precipitation initiation and maintenance throughout the United States and elsewhere, especially in Europe. Orography has been shown to initiate convection if instability is present, without any required synoptic to mesoscale forcing due to upslope mechanical lift. Furthermore, the topographic feature can serve as an elevated heat source that can further enhance upslope flow (e.g., Banta 1990). The convective boundary layer over topography extends higher into the atmospheric column and can serve to reduce convective inhibition. Additionally, strong boundary layer ascent associated with topographic features can further increase the probability for convection initiation (e.g., Banta 1984; Kirshbaum 2013). Topographic features have also been found to maintain quasi-stationary convective systems that enhance the threat for flash flooding (e.g., Doswell et al. 1996). Sustained, convectively unstable low-level flow perpendicular to the terrain feature combined with weak upper level flow scenarios have been found to cause quasi-stationary convection in significant flooding cases such as the Rapid City flood of 1972, the Big Thompson Canyon flood of 1976 (Maddox et al. 1978), the Madison County flood of 1995 (Pontrelli et al. 1999), and the Fort Collins flood of 1997 (Petersen et al. 1999). In similar situations where strong flow confined to the lower levels impinges on a barrier, the upstream cold pool propagation can become balanced by the lower-level flow, which can further aide in quasi-stationary convective maintenance (e.g., Ducrocq et al. 2008). Both of these mechanisms can maintain quasi-stationary systems as long as the low-level moisture inflow is persistent, for example from the presence of a moist lower level jet (LLJ). However, it has also been shown that weak vertical shear cases with along barrier winds can also produce quasi-stationary convective events (e.g., Soderholm et al. 2014). Many case studies of the orographic effects of specific topographic features have been carried out in many different regions around the globe. Some of these features include the Massif Central and other features near the Mediterranean Sea (e.g., Ducrocq et al. 2008; Bresson et al. 2012) the Black Hills (Soderholm et al. 2014), the Rhine River valley (Weckwerth et al. 2014), the Blue Ridge in Virginia (Pontrelli et al. 1999), and southwestern England (Lean et al. 2009). Most of these features, except the last, deal with topographic features that have a larger vertical extent and gradients than the Balcones Escarpment; however, this does not necessarily mean similar mechanisms do not apply.

2.3.1. The Balcones Escarpment in Central Texas. It has been well established that more fatalities and injuries due to flooding have occurred in Texas than any other state in the contiguous United States (CONUS) (e.g., Smith et al. 2000; Ashley and Ashley 2008; Sharif et al. 2010). Floods in Texas are characterized by frequent events that result in less than 20 deaths per occurrence with large individual events yielding more fatalities. In these events, over 50% of the fatalities are associated with flash floods, and 77% of these are motor vehicle related. Population-normalized annual flood related death rates show a steady decline; however, from 1959 to 2008, Texas was the only state to record a flood related fatality in each year (Sharif et al. 2015). This highlights the vulnerability of populations in Texas to flood related dangers. Vulnerability can be thought of, in the case of flooding, as the potential loss of life and property due to the impact of a flood on a specific population with certain mitigation measures, or lack thereof, in place (Cutter 1996). In places such as Texas, the knowledge of this vulnerability has led to the implementation of flood mitigation strategies; however, due to increasing populations in flood-prone areas, loss of life and property from flooding events continue to be non-negligible despite these measures (e.g., Pielke Jr and Downton 2000; Burby 2001).

Injury and death from flash flooding occur more frequently in rural areas, due to different compounding factors. First responders are often closer to urban areas and more able to rescue those in harm's way or implement real time mitigation strategies, such as settling up road blocks. Given that flash floods are defined by their short time scales, the distant proximity and, thus, longer response time of the first responders to rural flash flood event can increase the mortality/injury rate over urban areas (e.g., Špitalar et al. 2014). Additionally, monies spent on infrastructure in rural areas is often less, which can lead to inadequate structural mitigation strategies (i.e., more low-water crossings compared to bridges) (e.g., Jonkman 2005). Rural areas (especially farmland) often are in the headwater catchments for creeks and streams, which have fast rainfall-runoff response times. However, if a flash flood does

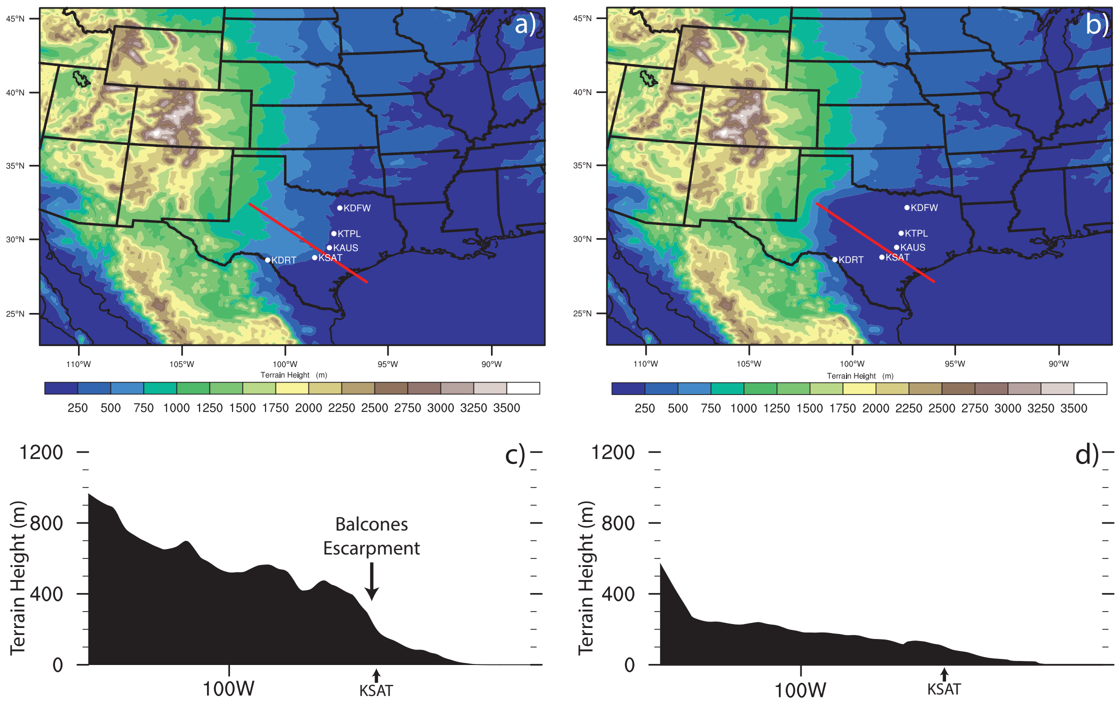

FIGURE 2.9. Model resolved terrain elevation plan view (m) and cross section for (a) the control simulations and (b) for the terrain-modification simulations over the entire WRF-ARW domain. Red line in (a) and (b) represents location of cross section in the lower part of each panel. Location labels correspond to cities (specifically airports) located on or near the Balcones Escarpment to identify its approximate location in central Texas (KDRT is Del Rio, TX; KSAT is San Antonio, TX; KAUS is Austin, TX; KTPL is Temple, TX; and KDFW is Dallas/Fort Worth, TX).

occur in an urban area, many more people per event are injured or killed, which can be partially attributed to motor related incidents (Špitalar et al. 2014). It is important to note that both substantive urban and rural areas are present in a local flash flood fatality maximum in central Texas.

Within the state itself, a maximum of flood related fatalities is located in central Texas, coincident with a topographic feature known as the Balcones Escarpment (Fig. 2.9a,c, as traced by identified cities) (e.g., Ashley and Ashley 2008; Sharif et al. 2015). The Balcones Escarpment is a region of steeply sloped terrain that separates the mainly limestone formations of the Edwards Plateau (i.e. the Texas Hill Country) from the flat clay and sand based coastal plain (Baker 1975). Several heavily populated urban areas, including San Antonio, New Braunfels, Austin, and Dallas, Texas are all located along this terrain feature. Due to this increased risk, this region, which stretches in an arc from San Antonio to Dallas, is colloquially known as "Flash Flood Alley." While there is no recognized definition or well-known origin of this term, it is used locally by meteorologists, newscasters, and civil officials (Sharif et al. 2015). The frequent use of this term highlights that the elevated flooding risk in central Texas is popular knowledge. Additionally, the increased flood danger has been formally discussed and evaluated within civil bodies such as National Weather Service (NWS) and local emergency management (e.g., NWS 1999; Martin and Edwards 1995). Furthermore, Stevenson and Schumacher (2014) showed a local clustering of rainfall events exceeding the 50-yr recurrence interval at various accumulation periods in central Texas over the ten years from 2002 to 2011, with many of the events not limited to a single season.

The effect of the Balcones Escarpment on flooding can be broken into hydrologic and meteorological forcing factors. The hydrologic effects are static and better understood than the meteorological forcing. Steep, limestone slopes with narrow river valleys and little vegetation characterize the transition from the Edwards Plateau to the coastal plain along the Balcones Escarpment. This limestone bedrock, combined with urbanization, increases rainfall–runoff and stream discharge (e.g., Baker 1975; Caran and Baker 1986). Consequently, measured stream discharges in this region typically exceed those observed for similar sized catchments in the rest of the United States. The narrow stream channels, combined with large flow discharges, lead to great flow depths, in some cases up to 15 meters, and extensive flooding (Patton and Baker 1976; Baker 1977; Costa 1987). Furthermore, floods in this region reach peak stream discharge much closer to the time of maximum precipitation, compared to the rest of the Texas coastal plain (Smith et al. 2000). All of these factors lead to the "Flash

Flood Alley" region along the Balcones Escarpment being more vulnerable to flash floods than any other region in the contiguous United States based on hydrologic rainfall–runoff characteristics alone (O'Connor and Costa 2004).

The meteorological influence of the Balcones Escarpment on extreme precipitation in central Texas is not completely understood. Orographic ascent along the escarpment has been theorized to be an important forcing mechanism for the extreme rainfall that is observed in central Texas (e.g., Baker 1975; Caran and Baker 1986). The abrupt elevation rise is believed to help initiate convection when warm, moist air from the Gulf of Mexico ascends the Balcones Escarpment. Caracena and Fritsch (1983) suggested the escarpment could serve to preserve air parcel saturation through orographic lift and potentially stall a northward moving air mass boundary. However, in the cases discussed, Caracena and Fritsch (1983) were not able to discern the importance of the Balcones Escarpment in the precipitation processes relative to other meteorological factors. Additionally, Nielsen-Gammon et al. (2005) examined in detail a flooding event that occurred in central Texas in 2002 along the Balcones Escarpment. They found that the main forcing for the extreme rainfall accumulations was from a stationary upper-level trough that remained in place for almost a week due to complex interactions of many meteorological contributions. However, smaller scale processes, including mechanical lifting along the Balcones Escarpment, were thought to serve to localize heavy precipitation along the terrain feature. The importance of the Balcones Escarpment on the location and intensity of the observed rainfall is not well known and has been identified as a topic warranting more investigation through the aforementioned and other studies (e.g., Smith et al. 2000).

One of this study's goals is to determine the influence of the Balcones Escarpment on three recent flooding events that occurred in central Texas. In three cases discussed here, radar imagery indicated regions of repeated convective development near the Balcones Escarpment and the largest precipitation accumulations occurred near the Escarpment. This led the author to suspect that orographic effects were important in enhancing or focusing the precipitation in these extreme rainfall events. Each case is examined using simulations from a numerical weather prediction (NWP) atmospheric model. A control run representing the model's interpretation of the event will be compared to a terrain-modified run in which the terrain gradient associated with the Balcones Escarpment will be altered.

CHAPTER 3

Description of Extreme Precipitation Events

3.1. Selection of Cases

Events for the ensemble predictability experiments were chosen to represent important extreme rainfall producing storms types (e.g., Quasi-Stationary MCSs and PREs) that recently occurred in the warm season and were not particularly well represented by operational forecast models. Additionally, events for the terrain variability experiments were chosen based upon recent flooding that occurred on the Balcones Escarpment in central Texas. In total, two of the events were associated with mesoscale convective vortices (MCVs), another event with the inland propagation of a tropical cyclone, a fourth event associated with a pre-frontal trough, and, lastly, a fifth event involving a fast-moving, warm-season MCS. Each chosen case represents a different synoptic or mesoscale pattern that led to the extreme rainfall. More specifically, the MCV and tropical cyclone events represent cases of quasi-stationary MCSs and PREs (see introduction chapter sections 2.1.2 and 2.1.3) that produced extreme rainfall and flooding. A concise meteorological overview of each rainfall event is presented in this chapter and is supplemented by synoptic maps valid during the period of most intense rainfall taken from the North American Regional Reanalysis (NARR) (Mesinger et al. 2006). Additionally, illustrative observed soundings from various locations and the NCEP Stage-IV gridded precipitation analysis (Lin and Mitchell 2005) for each event are presented. The precipitation accumulation of the control ensemble members is later evaluated by comparison to the NCEP Stage-IV gridded precipitation analysis. The NCEP Stage-IV uses a multi-sensor approach that includes both rain gauge and radar accumulation data to create the gridded analysis (Lin and Mitchell 2005). This precipitation analysis was chosen because of the high spatial (4km) and temporal (hourly) coverage of the product, which would not be possible from a reanalysis (e.g., the NARR). While issues with the accuracy of Stage-IV analysis arise in complex terrain and regions with sparse gauge coverage, the regions examined here are heavily populated with many gauges and contain relatively simple terrain (when compared to the Rocky Mountains for instance) that causes little radar interference and beam blockage, which reduces these possible inaccuracies. Although, as with any gridded precipitation analysis, there are uncertainties in the exact quantitative precipitation estimate; however, the Stage-IV analysis should create a representative depiction of the accumulated precipitation in these specific cases.

3.2. Tropical Storm Erin August 2007

Tropical storm Erin formed in the central Gulf of Mexico 375 n mi to the east-southeast of Brownsville, Texas the on 15 August 2007 after spending about 12-hr at tropical depression strength. Erin continued on a northwestward tack and made landfall with maximum winds of 30 kt at tropical depression strength near San Jose Island, Texas at 1030 UTC 16 August 2007 (Brennan et al. 2009). Erin's inland track continued northwestward until reaching west Texas where the upper-level ridge to the east (Fig. 3.1a) steered the storm northward and then northeastward into southwestern Oklahoma on 19 August (Fig. 3.1a). Erin showed signs of reintensification at this time with some sustained wind reports approaching 50 kt (Brennan et al. 2009). The overland reintensification was due to a combination of unseasonably high land surface fluxes associated with evapotranspiration, due to an unseasonably wet spring an early summer in 2007, (e.g., Arndt et al. 2009; Evans et al. 2011) and the development of deep convection related to lift from the vortex in vertical shear (Fig. 3.1d) (e.g., Trier and Davis 2002) or quasigeostrophic forcing for ascent from a upper-level short wave trough to the north of Erin (Brennan et al. 2009). Tropical Storm Erin's vortex was responsible for a total of 16 fatalities (9 direct, 7 indirect); most of which were caused by inland flooding. Many homes in the Houston and Oklahoma city area were flooded, and almost $25 million dollars of damage was associated with the vortex (Brennan et al. 2009).

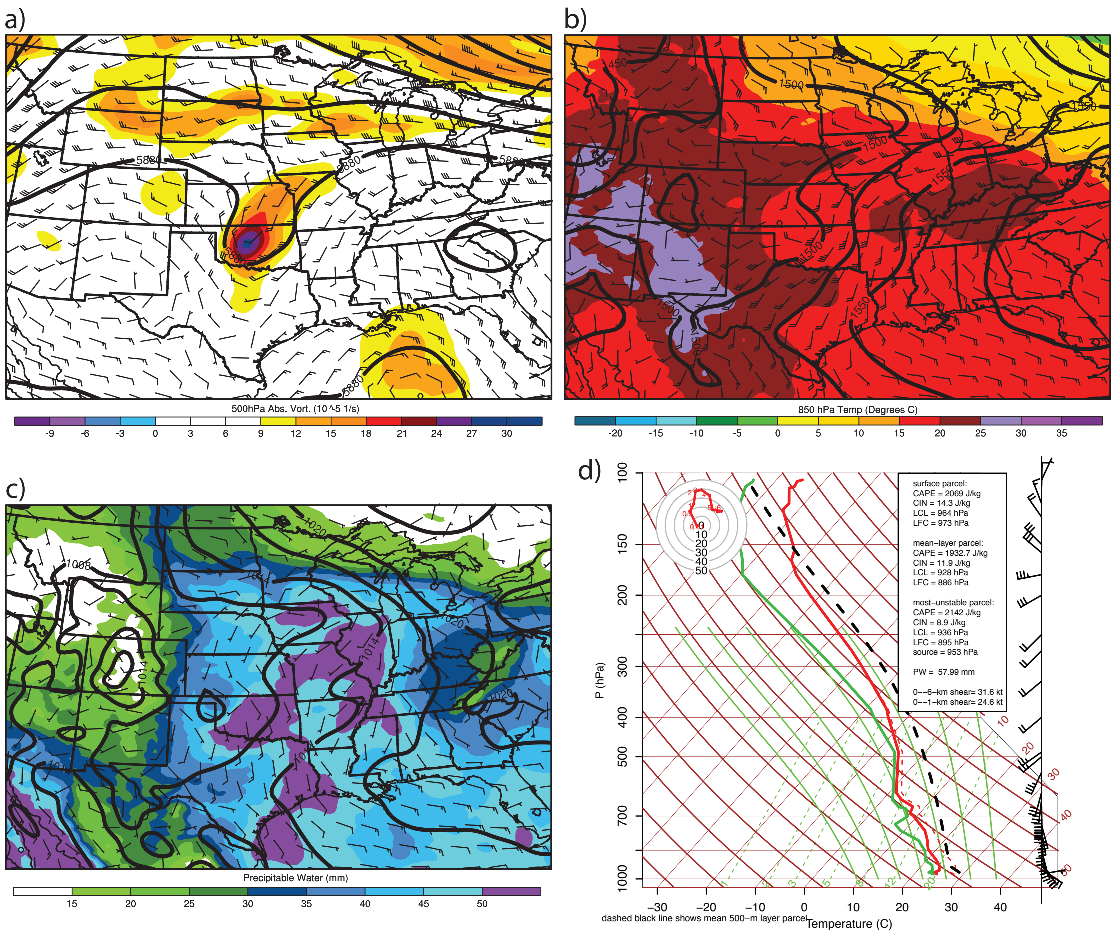

FIGURE 3.1. (a)–(c) NARR analyses at 1200 UTC 19 August 2007, and (d) skewT–logp diagram showing sounding from Norman, Oklahoma (OUN) at 0000 UTC 19 August 2007. (a) Absolute vorticity at 500-hPa ($\times 10^{-5}\mathrm{s}^{-1}$), shaded every $3 \times 10^{-5}\mathrm{s}^{-1}$ above $-9 \times 10^{-5}\mathrm{s}^{-1}$), 500-hPa geopotential height (contoured every 60 m), and 500-hPa wind barbs(half barb = 5 kt, full barb = 10kt, pennant = 50 kt, 1 kt = 0.5144 ms^{-1}). (b) 850-hPa geopotential height (contoured every 25 m), 850-hPa wind barbs, and 850-hPa temperature (shaded every 5°C from -20°C to 35°C). (c) precipitable water (shaded contours every 5 mm for values from 10 mm to 50 mm), 10m wind barbs, and mean sea level pressure (MSLP) (contoured every 3 hPa). Dashed black line in (d) shows the temperature of a lifted parcel with the mean characteristics of the lowest 500 m.

Precipitation totals associated with the vortex itself in the 12-hr period ending 1200 UTC 19 August exceeded 250 mm in central Oklahoma (Fig. 3.2d); however, higher rainfall maximums (over 300 mm) and a much larger area of accumulation in the southern Great Lakes region over the same period were caused by a PRE related to Erin (Fig. 3.2d). Deep tropical moisture, with precipitable water values over 50 mm, was transported northward into the Great Lakes region by a southerly low-level jet (Fig. 3.1b,c). The precipitable water transport north from Erin was enhanced by the presence of moisture already located in the Great lakes region (Fig. 2.6). The warm moist air impinged upon a low-level baroclinic zone in a northwest to southeast orientation over the Great Lakes located south of an upper-level jet maximum (Figs. 3.1b, 2.6). The low-level jet aided in frontogenesis along the baroclinic zone and strengthened the synoptic to mesoscale forcing for ascent. The presence of favorable ingredients for extreme rainfall (e.g., Doswell et al. 1996) led to the formation of a MCS late on 18 August. A nearly stationary MCS was created at times when the convective storm motion and new cell propagation vectors opposed one another (e.g., Corfidi 2003). A total of 8 fatalities and over $280 million dollars in damage were caused by flooding along the Mississippi River Valley associated with the Erin PRE (NOAA 2007).

3.3. MCV Event: 9-11 June 2010

The intense rainfall during the early morning hours on 9 June 2010 was associated with a mesoscale convective vortex (MCV) that migrated through Texas (Fig. 3.4a) and into Arkansas over an unusually long period of time from 3-11 June 2010. This event has been previously covered in great detail by Schumacher et al. (2013) and Schumacher and Clark (2014). Isolated rainfall associated with the northward moving MCV and pronounced warm air advection (Fig. 3.4b) initiated to the northeast of the San Antonio, Texas (KSAT) area

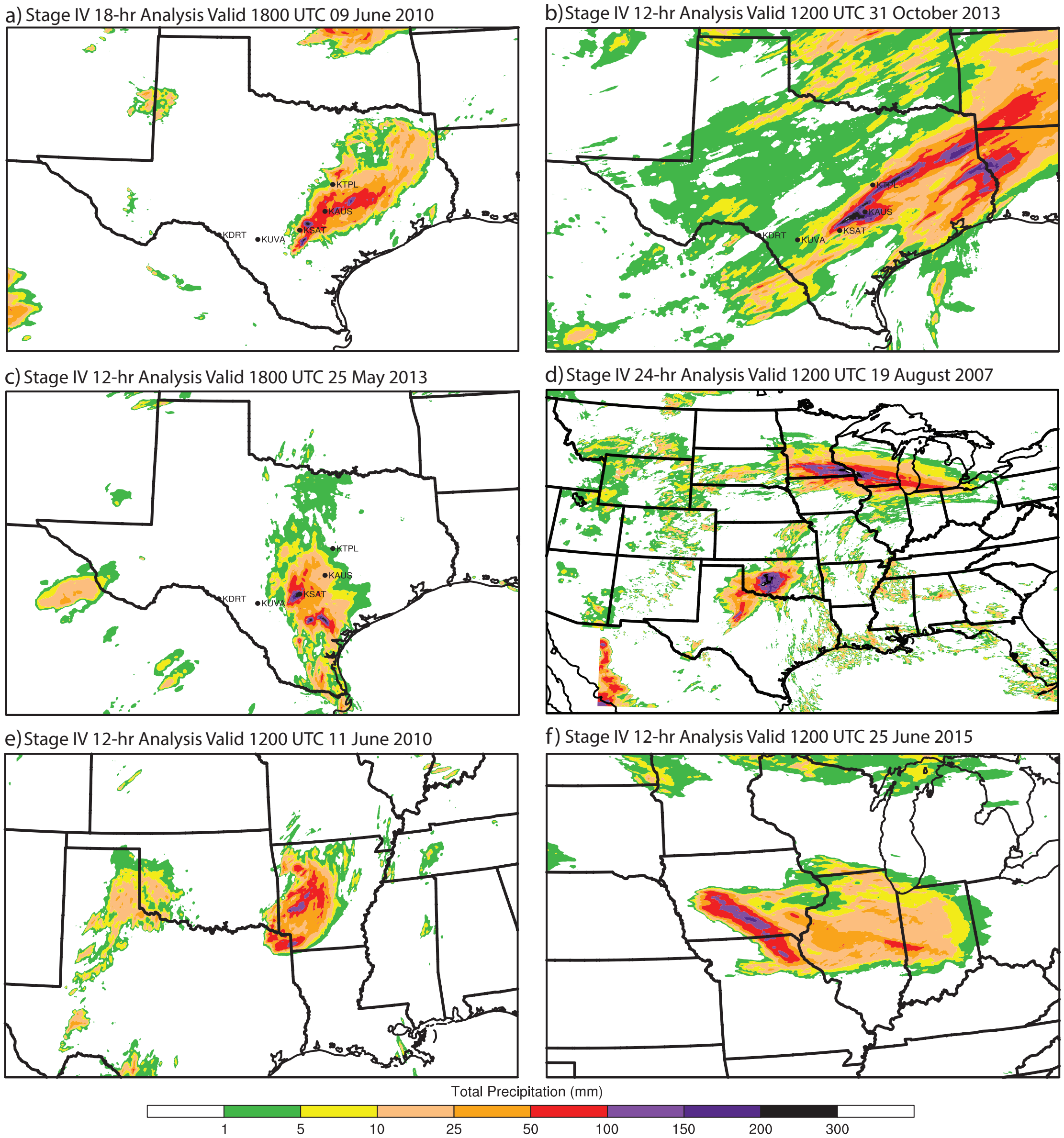

FIGURE 3.2. NCEP Stage IV precipitation analysis accumulation for each flooding event valid (a) the 18-hr period ending 1800 UTC 09 June 2010, (b) the 12-hr period ending 1200 UTC 31 October 2013, (c) the 12-hr period ending 1800 UTC 25 May 2013, (d) 24-hr period ending 1200 UTC 19 August 2007, (e) the 12-hr period ending 1200 UTC 11 June 2010, and (f) the 12-hr period ending 1200 UTC 25 June 2015. Locations labels refer to same cities as described in Fig. 2.9 with the addition of KUVA for Uvalde, TX.

around 0000 UTC on 9 June. Heavy rain continued to fall, fed by moist inflow, at both the surface and 850 hPa, from the Gulf of Mexico (Fig. 3.4c,d) with small storm motions in and around central Texas until 1800 UTC on the same day (Fig. 3.2a), at which point the

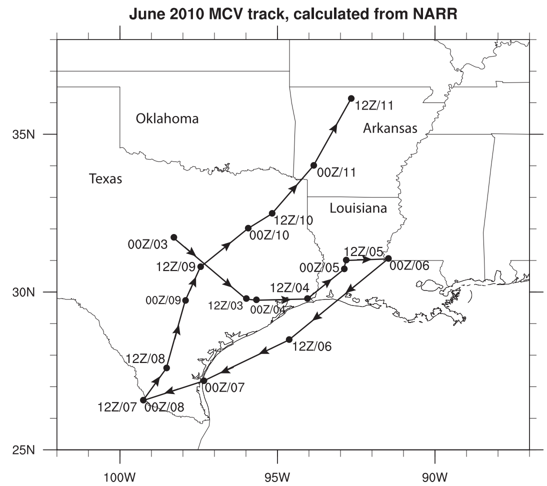

FIGURE 3.3. Objectively analyzed track of the long-lived MCV in June 2010. The track was determined by finding the 288 km X 288 km (9 X 9 grid point) box with the largest total 700–500-hPa layer-averaged relative vorticity in the NARR, and defining the center of that box as the MCV location. MCV locations are plotted every 12-hr, with the notation of, e.g., "00Z/03" indicating 0000 UTC 3 Jun 2010. Names of states mentioned in the text are also shown. From Fig. 1a of Schumacher and Clark (2014).

MCV began moving out of the region to the northeast. Precipitable water values from the 1200 UTC Corpus Christi (CRP) sounding (Fig. 3.4d) were above the 90th climatological percentile for that day (NOAA 2015b) . A maximum rainfall amount of 287 mm (11.3 inches) for the event was observed by multiple stations to the northwest of New Braunfels, Texas by the Community Collaborative Rain, Hail, and Snow network (CoCoRaHs; Cifelli et al. 2005). The flash flooding caused property damage totaling $10 million and one fatality, with the heaviest damage in the Guadalupe River Basin. The MCV associated with this event went on to produce a deadly flash flood in Arkansas that resulted in twenty fatalities (NOAA 2015a) .

The latent heat release from the deep convection associated with the flooding near KSAT intensified the MCV, and the feature continued to move north and east over the next day (Fig. 3.3). The MCV produced another MCS in northeast Texas on 10 June 2010 with flooding reported in some communities (NOAA 2015a) . This convection again strengthened the MCV

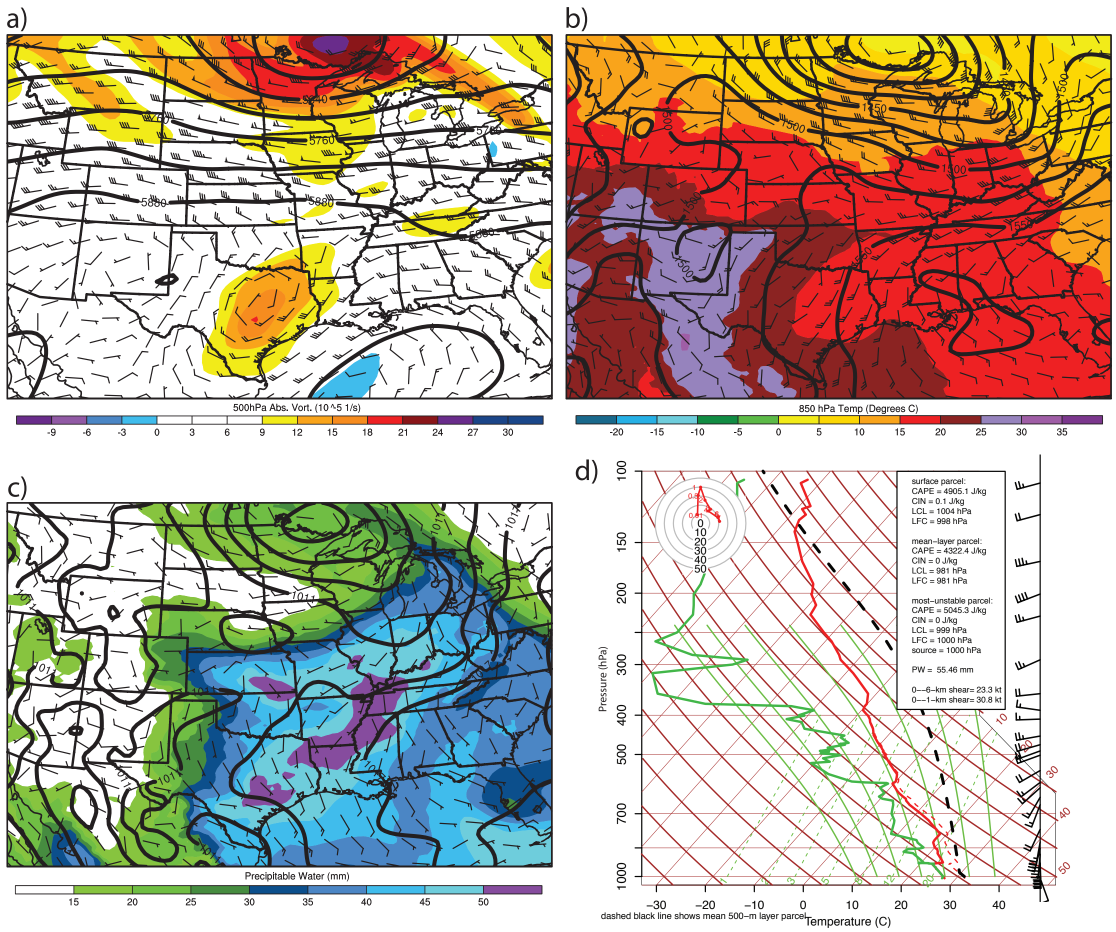

FIGURE 3.4. As in Fig. 3.1 except (a)–(c) NARR analyses at 0900 UTC 9 June 2010, and (d) skewT–logp diagram showing sounding from Corpus Christi, Texas (CRP) at 1200 UTC 9 June 2010.

(Fig. 3.5a) as the feature moved into western Arkansas early on 11 June 2010. Convection again formed over night on 11 June fed by southerly low-level jet and high precipitable water values (over 50 mm) (Fig. 3.5c,d). The 0000 UTC 11 June 2010 Shreveport, Louisiana sounding also had almost 2000 J/Kg of most unstable CAPE (Fig. 3.5d). The convection produced over 100 mm of rainfall over the rugged terrain in western Arkansas (Fig. 3.2e). This rainfall produced a deadly flash flood along the Little Missouri and Caddo Rivers that resulted in twenty fatalities (NOAA 2015a) .

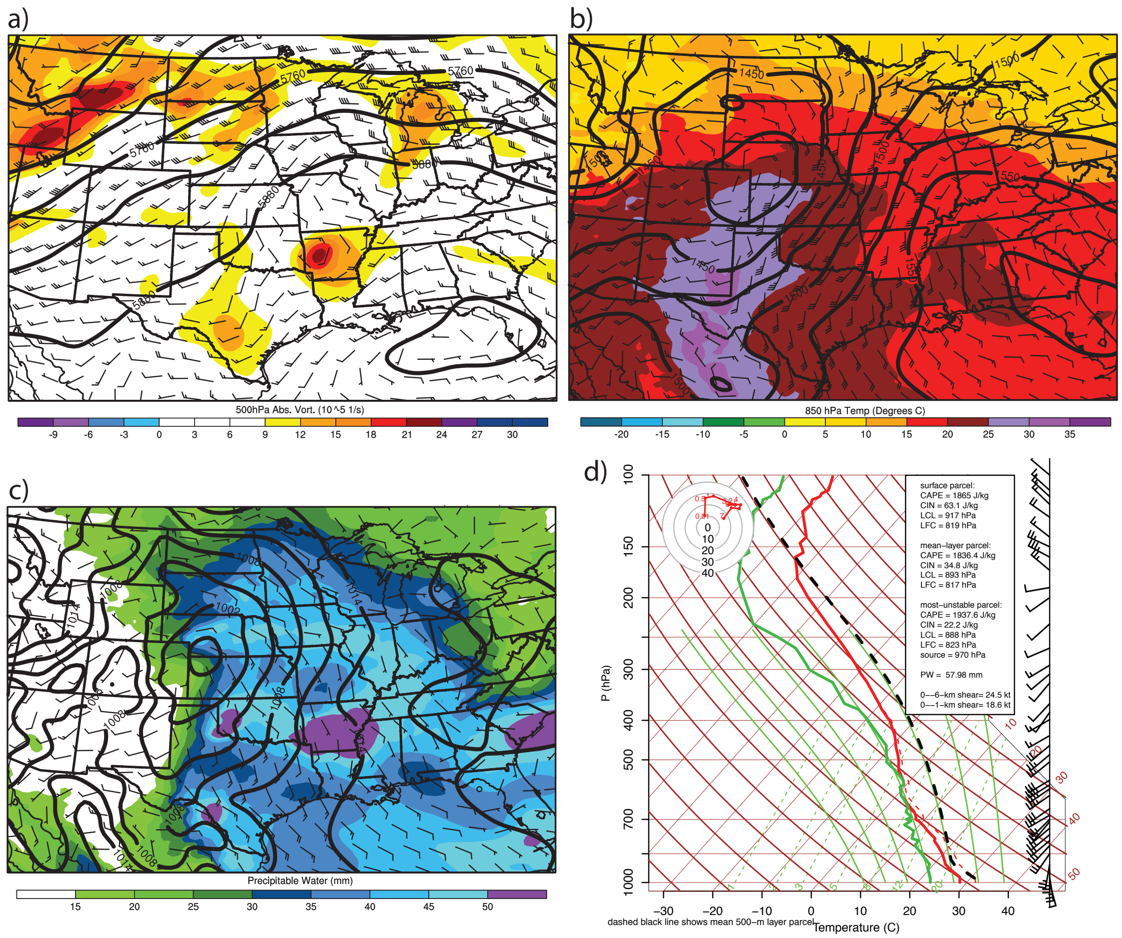

FIGURE 3.5. As in Fig. 3.1 except (a)–(c) NARR analyses at 0600 UTC 11 June 2010, and (d) skewT–logp diagram showing sounding from Shreveport, Louisiana (SHV) at 0000 UTC 11 June 2010.

3.4. MCV Event: 25 May 2013

On 25 May 2013, convection associated with a quasi-stationary, pre-existing MCV (Fig. 3.6a) produced large amounts of precipitation in the KSAT metro area and other nearby regions of south-central Texas (Fig. 3.2c). The MCV was formed as a result of convection that developed in the Texas panhandle on 23 May 2013. Unlike the June 2010 case, the MCV moved into the KSAT area from a more northerly direction, compared to the 9 June 2010 event. Rain began to fall around 0600 UTC 25 May, and continued until 1800 UTC, at which point convection ceased at the center of the system. During this period, the MCV

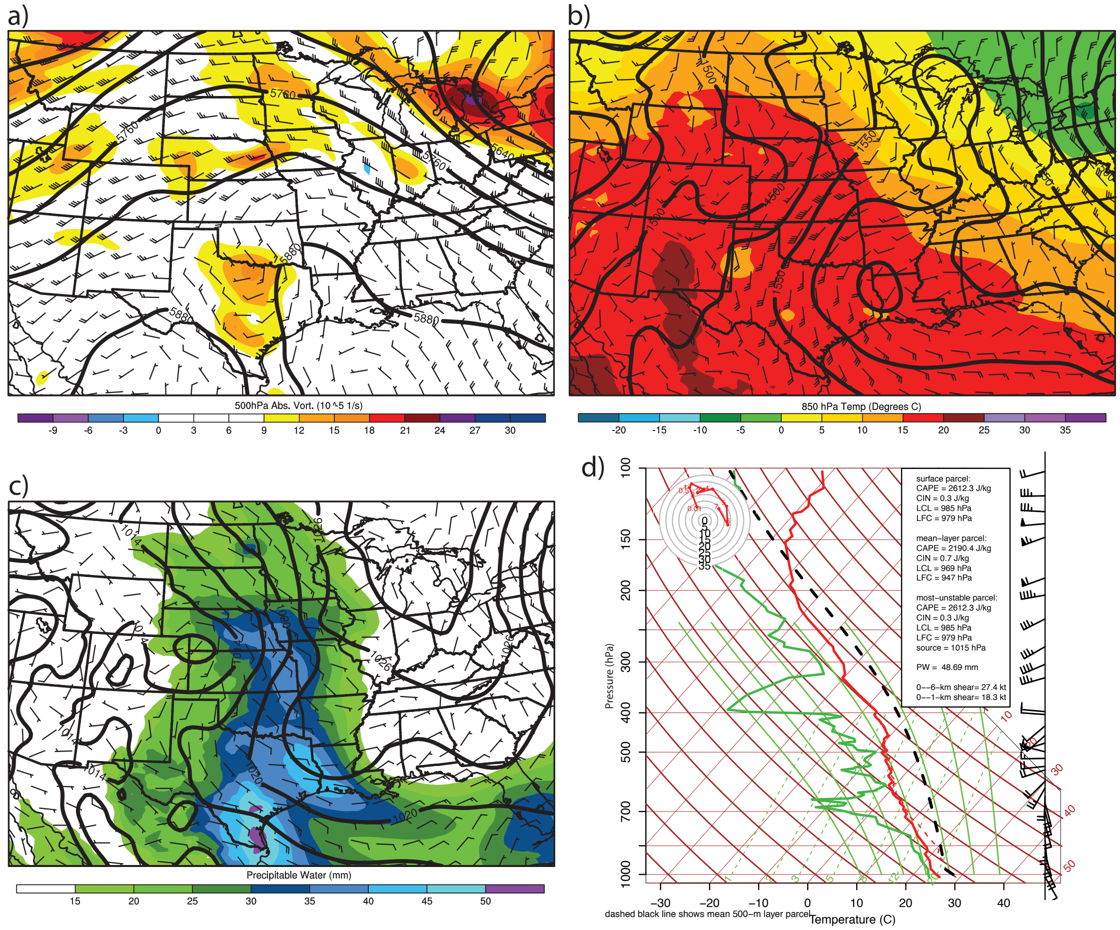

FIGURE 3.6. As in Fig. 3.1 except (a)–(c) NARR analyses at 1200 UTC 25 May 2013, and (d) skewT–logp diagram showing sounding from Corpus Christi, Texas (CRP) at 1200 UTC 25 May 2013.

stayed relatively stationary with warm, moist flow from the southeast providing the moisture supply (Fig. 3.6b,c). This southeasterly, moist flow off the Gulf of Mexico extended over a deep layer, from the surface to around 600 hPa in height (Fig. 3.6d). Further, the 1200 UTC 25 May 2013 CPR sounding (Fig. 3.6d) measured precipitable water values over the 90th climatological percentile for that day (NOAA 2015b) . The San Antonio International Airport recorded 250 mm (9.87 inches) of precipitation between 0800–1700 UTC on 25 May with the heaviest rain rates occurring near 1200 UTC. A United States Geological Survey rain gauge in San Antonio recorded a one-hour rainfall accumulation of 156 mm (6.13 inches) with a 24-hour accumulation of 432 mm (17.0 inches). Once again, the heaviest precipitation occurred near the southeastern edge of the Balcones Escarpment. Due to the high rainfall rates, flash flooding occurred in creeks, streams, and rivers leading to many road closures. Three fatalities were recorded when flood waters swept cars and pedestrians off of roadways (NOAA 2015a) .

3.5. Pre-Frontal Trough: 31 October 2013

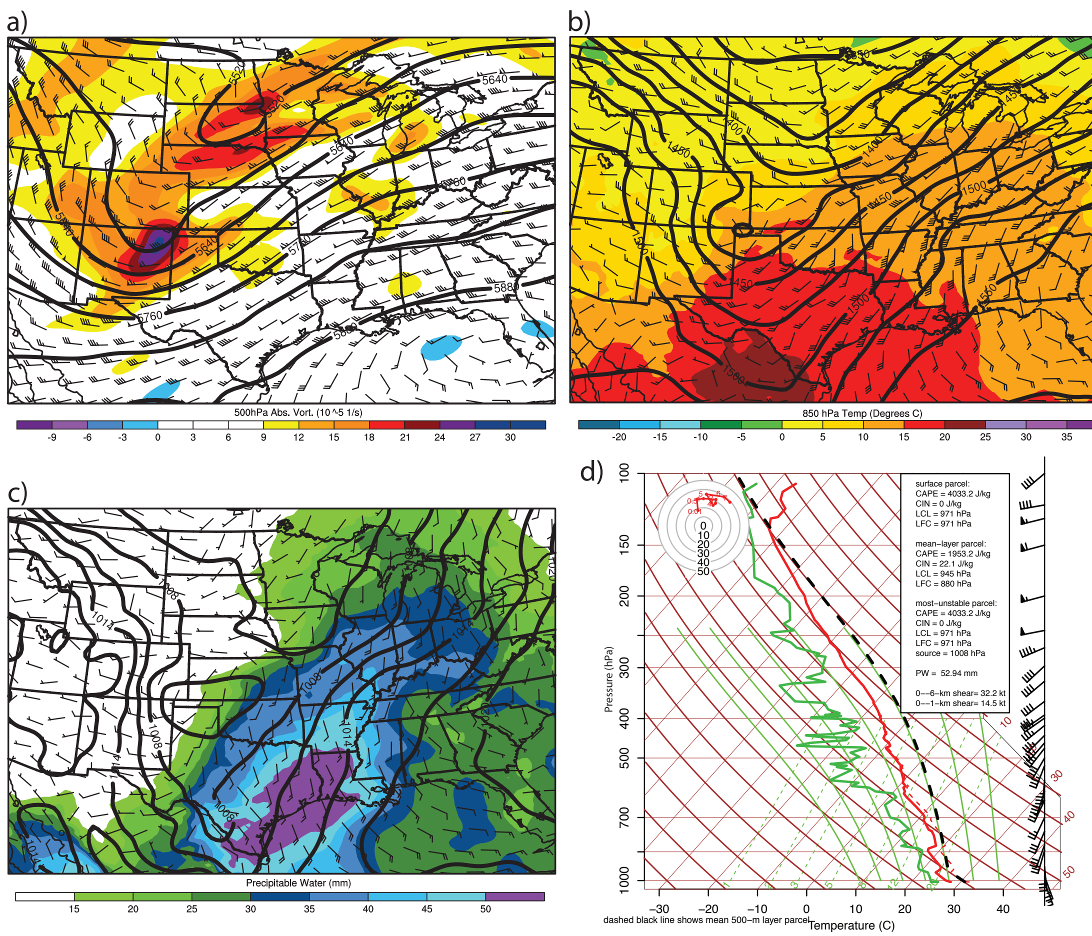

Figure 3.7. As in Fig. 3.1 except (a)–(c) NARR analyses at 0600 UTC 31 October 2013, and (d) skewT–logp diagram showing sounding from Corpus Christi, Texas (CRP) at 0000 UTC 31 October 2013.

An upper-level trough centered over northeastern New Mexico (Fig. 3.7a) was responsible for widespread intense rainfall that occurred in south-central and eastern Texas on 31 October 2013. A developing surface front, combined with a pre-frontal lower level trough and warm air advection (Fig. 3.7b,c), provided sustained lift over the period from 0000 UTC to 1800 UTC that same day. Precipitable water values (Fig. 3.7c,d) above the 90th percentile for the daily average contributed to the strength and intensity of the rainfall (NOAA 2015b) . Furthermore, storm motions resulted in continued "echo training" of intense rainfall over the same regions. Unlike the previously discussed event, the rainfall on 31 October occurred in an environment with strong synoptic-scale forcing for ascent. The largest rainfall totals were observed in a southwest to northeast line stretching from north of KSAT through Austin (KAUS) to Temple, Texas (Fig. 3.2b). The heavy rain that fell in this corridor resulted from convection that repeatedly formed along and ahead of the surface front, and also along the eastern edge of the Balcones Escarpment. Within this belt of large rainfall accumulations, a maximum CoCoRaHS observation of 305 mm (12.0 inches) was recorded. The most intense flash flooding occurred in watersheds near the Austin area where $100 million dollars worth of damage occurred and over 100 homes were destroyed. Four fatalities were reported in the KAUS area due to rapidly rising floodwaters (NOAA 2015a) .

3.6. Bowing MCS: 25 June 2015

On 25 June 2015, during the Plain Elevated Convection at Night (PECAN) field campaign, a bowing MCS, with some characteristics of the bow-and-arrow archetype (Keene and Schumacher 2013), initiated in central Iowa around 0000 UTC and propagated southeastward through Illinois and Missouri producing maximum 12-hr precipitation accumulations in Iowa (Fig. 3.2f). A zonal upper-level pattern dominated the northern part of the U.S., while an upper-level ridge was in place in the southeastern part of the country (Fig. 3.8c). Central Iowa was located at the time in the right entrance region of an upper level jet streak embedded in the zonal flow, which enhanced synoptic scale forcing for ascent. Substantial

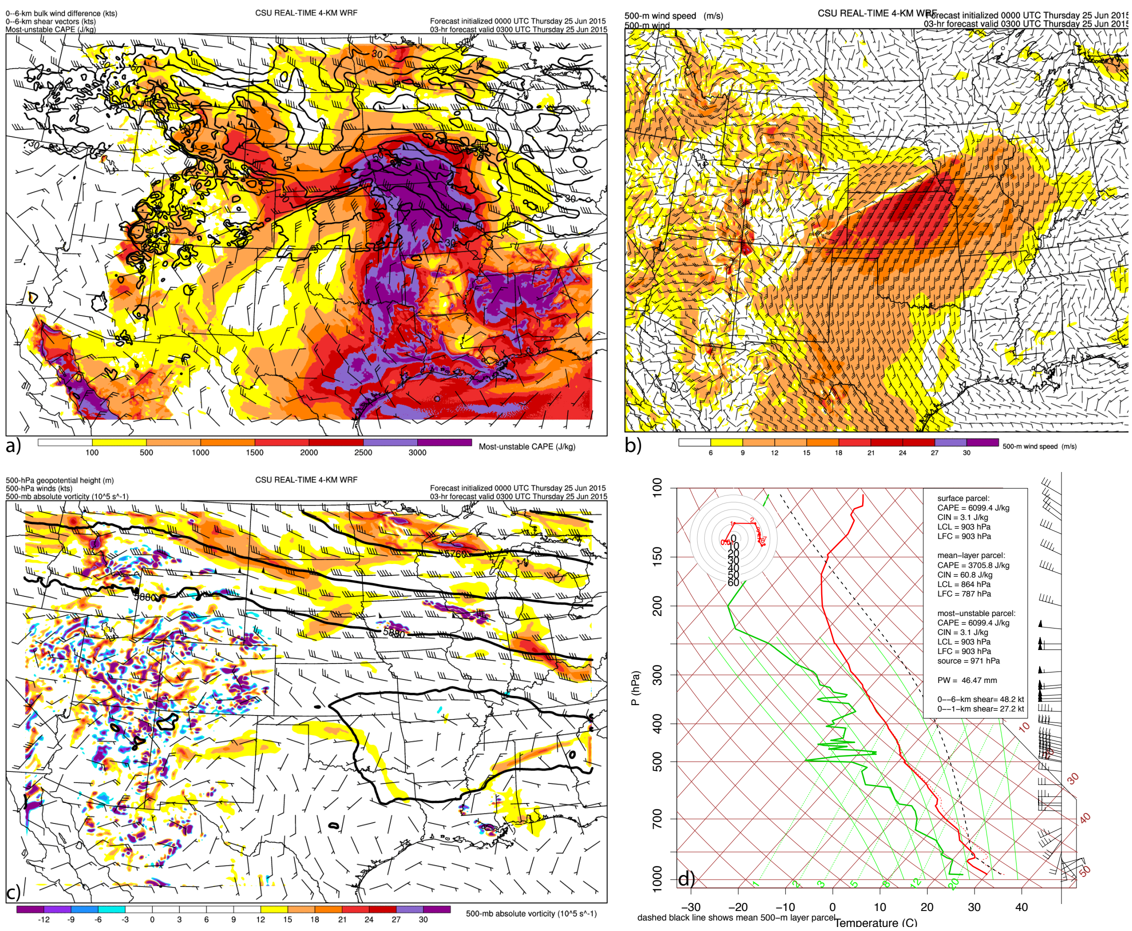

FIGURE 3.8. (a)–(c) Colorado State University 4 km WRF-ARW forecast valid F003 at 0300 UTC 25 June 2015, and (d) skewT–logp diagram showing sounding from Omaha, Nebraska (OAX) at 0000 UTC 25 June 2015. (a) MUCAPE, shaded every 500 J/Kg about 100 J/Kg; 0–6 km shear wind barbs (half barb = 5 kt, full barb = 10kt, pennant = 50 kt, 1 kt = 0.5144 ms^{-1}); and 0–6 km bulk wind difference in black contours. (b) 500 m wind speed, shaded every 3 kt above 6 kt, and 500 m wind barbs. (c) Absolute vorticity at 500-hPa ($\times 10^{-5}\mathrm{s}^{-1}$), shaded every $3 \times 10^{-5}\mathrm{s}^{-1}$ above $-9 \times 10^{-5}\mathrm{s}^{-1}$), 500-hPa geopotential height (contoured every 60 m), and 500-hPa wind barbs. Dashed black line in (d) shows the temperature of a lifted parcel with the mean characteristics of the lowest 500 m.

instability was in place for elevated parcels leading up to the event with observed soundings in the area containing over 6000 J/Kg of MUCAPE and precipitable water values over 45 mm (Fig. 3.8d). Furthermore, an east-west temperature gradient left over from previous convection was draped across the area (as seen by wind shift in Fig. 3.8b). Short term high-resolution model forecasts had over 3000 J/Kg of MUCAPE persisting in an environment with around 60 kt of 0–6 km shear through the overnight hours (Fig. 3.8a). Further, the development of over a 40 kt low-level jet out of the southwest was forecast to develop during this same period (Fig. 3.8b) and precipitable water values were forecast in some areas to reach over 50 mm (not shown). The combination of the low-level convergence associated with the low-level jet (Fig. 3.8b), small embedded short waves in the upper-level flow (Fig. 3.8c), and warm air advection at mid-levels (not shown) led to convective initation around 2300 UTC June 24 2015. The cells quickly grew upscale and organized in the presence of the significant instability and shear. By 0500-0600 UTC 25 June several imbedded bowing line segments, in both the bow and arrow portions of the MCS, moved through southern Iowa, northern Missouri, and western Illinois. Several severe wind reports occurred throughout the effected areas (NOAA 2015a) .

CHAPTER 4

Data and Methods

In order to evaluate the ensemble predictability and terrain induced variability of extreme precipitation, two different sets of experiments are performed in this study. The first evaluates the spread characteristics of a convection allowing ensemble for extreme precipitation events that occurred in Texas, Arkansas, and Iowa. The second experiment evaluates the terrain induced variability of the Balcones Escarpment in central Texas by "removing" the Balcones Escarpment from the NWP model terrain. The following sections outline the NWP model specifics, ICs and lateral boundary conditions (LBCs), cases used, and evaluation specifics for each experiment.

4.1. Ensemble Predictability Experiments

In this section the numerical model architecture, ensemble initial and boundary conditions, and ensemble spread evaluation strategy for the ensemble predictability experiments are described.

4.1.1. Numerical Model Architecture. In order to test the spread characteristics of a convection allowing ensemble, version 3.6 of the Advanced Research core of the Weather Research and Forecasting model (WRF-ARW; Skamarock et al. 2008) was used to create a 11-member ensemble, which corresponds to the number of members in the ensemble reforecast dataset used for the initial and lateral boundary conditions, at 4-km grid spacing. As discussed in the background section, grid spacing on the order of 4-km has been shown to adequately resolve convective systems, but not the motions of individual convective cells (e.g., Bryan et al. 2003). Convection-allowing EPS are now used in research and semi-operational predictions, such as the CAPS ensemble from University of Oklahoma (e.g., Xue and Coauthors 2007) and the experimental NCAR convection-allowing ensemble (e.g., Schwartz et al. 2015). Each ensemble member is created with only varied initial conditions, and the same set of model physics is applied to each member (Table 4.1). The model domain encompasses the vast majority of the central part of the United States, Mexico, and the Gulf of Mexico (Fig. 4.1). In order to keep the numerical calculations of each run consistent, each member was run on the National Center for Atmospheric Research's (NCAR) Yellowstone super computer in an identical configuration. In addition to the 4-km ensemble runs described above, one 2-km horizontal grid spacing ensemble run was created in the same configuration (i.e., same domain extent and model physics), with the exception of number of compute nodes, to test the effects of grid spacing (Table 4.1). Three cases were chosen for the these experiments to represent various extreme rainfall producing phenomena: a tropical cyclone and PRE associated with Tropical Storm Erin in 2007, a quasi-stationary MCV on 25 May 2013 in Texas, and a quick moving MCS that occurred on 25 June 2015 in Iowa and Missouri. These cases will be be the basis for some predictability experiments that will be described in detail in the following sections. However, three more cases were run for sake of comparison to these three events only: the MCV in Arkansas on 10 June 2010 (described in section 3.1.2), a 48-hr forecast initialized a day early for the Texas MCV case, and a day devoid of upscale convective growth on 10 June 2013.

4.1.2. Boundary and Initial Conditions. The ICs and LBCs used to create the 11 member ensemble were taken from the National Oceanic and Atmospheric Administration's (NOAA's) Second Generation Global Medium-Range Ensemble Reforecast Dataset (Reforecast-2; Hamill et al. 2013). The Reforecast-2 ensemble is a dataset of ensemble reforecasts based upon the 2012 update of the National Centers of Environmental Prediction's

Table 4.1. WRF-ARW model configuration for Ensemble Predictability Experiments

Parameter	Configuration
Horizontal grid	800 X 850 (1600 X 1700), Δx = 4km (2 km)
Vertical grid	50 levels, $\Delta z =\sim$ 50m near surface, $\Delta z =\sim$ 600m aloft
Cumulus Scheme	None
PBL Scheme	YSU (Hong et al. 2006)
Microphysics	Morrison 2-moment (Morrison et al. 2009)
Radiation	RRTMG (Iacono et al. 2008)
Land Surface Model	Noah (Chen and Dudhia 2001)

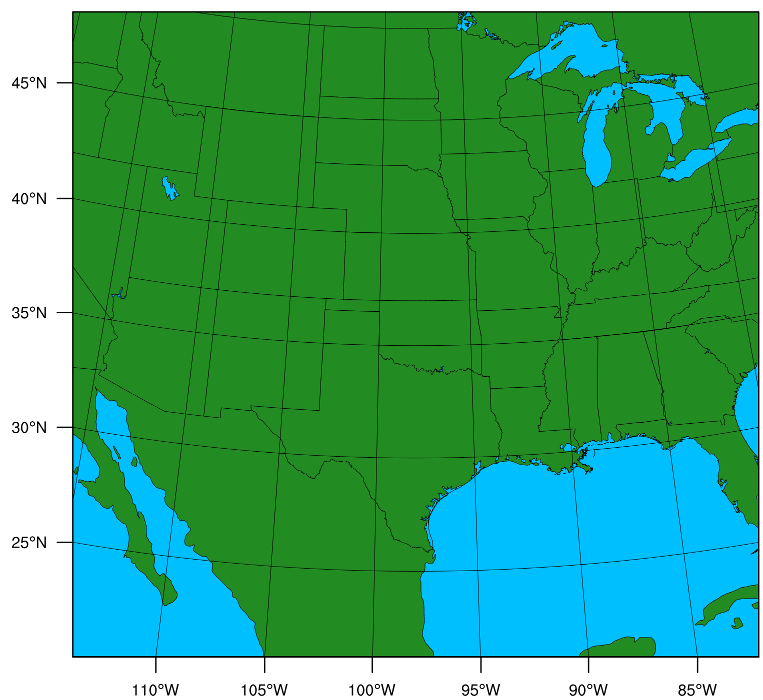

Figure 4.1. WRF-ARW domain for each member of the convection allowing ensemble.

(NCEPs) global ensemble forecast system (GEFS) that has once daily (at 0000 UTC) initializations from December 1984 to the present. Each run of the Reforecast-2 ensemble contains 11 members (10 perturbations and one control) that maintains the ensemble spread of the operational GEFS with fewer members. The first eight days of the Reforecast-2 ensemble is run at T254L42 resolution, which is the equivalent of 40 km grid spacing at 40° latitude. Given this native resolution of the Reforecast-2 ensemble, convection is parameterized and not explicitly represented. The Reforecast-2 ensemble creates an easily accessible, operationally representative, and temporally expansive dataset from which to obtain the ICs and LBCs to create a downscaled, convection allowing ensemble for almost any extreme rainfall event in the past thirty years.

For the five events used in the convection allowing ensemble experiments, all of the ICs and LBCs were taken from the Reforecast-2 ensemble. The forecasts were run at various forecast lengths depending on the timing of the extreme rainfall, and all of the model runs were initialized at 0000 UTC. The model runs associated with Tropical Storm Erin were run for 48 hours from 0000 UTC 18 August 2007, the Iowa MCS for 48 hours from 0000 UTC 25 June 2015, and a 24 hour simulation was performed for the Texas MCV case beginning 0000 UTC 25 May 2013. These three events represent the cases that will be used in the ensemble predictability experiments. Further, an ensemble associated with the Arkansas MCV was run for 48 hours from 0000 UTC 10 June 2010, the Texas MCV was run a day earlier for 48 hours starting 0000 UTC 24 May 2013, and the no upscale growth case for 36 hours from 0000 UTC 10 June 2013. These last three only have a control simulation and are used for comparison only. These per case initialization times, forecast lengths, and base ICs and LBCs (i.e., Reforecast-2 was the base ICs and LBCs for each experiment) were used for all of the ensemble experiments described in the next section (Table 4.2). A similar process of using the Reforecast-2 members to initialize the ICs and LBCs of a convection-allowing ensembles has been used previously in Galarneau and Hamill (2015) and Lawson and Horel (2015).

4.1.3. Ensemble Spread Evaluation. There are many ways to diagnose the evolution of a NWP ensemble's spread characteristics. For the purposes of this study, the ensemble spread will be quantified using the difference total energy (DTE) as a basis for evaluation

(Zhang et al. 2003; Zhang 2005; Melhauser and Zhang 2012). The DTE is defined in Zhang (2005) as:

$$DTE_{i,j,k,t,m} = \frac{1}{2}((u'_{i,j,k,t,m})^2 + (v'_{i,j,k,t,m})^2 + k(T'_{i,j,k,t,m})^2) \tag{3}$$

where the u', v', and T' are the differences of the zonal wind, meridional wind, and temperature from the ensemble mean, respectively, and $k = C_p T_r^{-1}$ ($C_p = 1004.9$ J kg^{-1} K^{-1} and $T_r = 270$ K). u', v', and T' are five dimensional variables that are functions of grid points in x-direction (i) and y-directions (j), vertical level (k), time (t), and ensemble member (m). DTE can be thought of as a representation of the energy difference per unit mass between the ensemble mean and a specific ensemble member. Further, one can define the root mean difference total energy (RMDTE) by taking the square root of the average DTE summing across each ensemble member in either the horizontal or vertical (Zhang 2005). The horizontal RMDTE as a function of the horizontal grid points and time can be expressed as:

$$RMDTE_{i,j,t} = \sqrt{\sum_{m=1}^{n_{members}} \frac{1}{n_{members}} \sum_{k=0}^{n_{levels}} \frac{p(k+1)-p(k)}{p(n_{levels})-p(0)} \frac{1}{2}((u'_{i,j,k,t,m})^2 + (v'_{i,j,k,t,m})^2 + k(T'_{i,j,k,t,m})^2)} \tag{4}$$

where $n_{members}$ is the number of ensemble members, n_{levels} is the number of vertical levels from the surface ($k = 0$) to model top ($k = n_{levels}$), and p is pressure on the vertical levels. For this study the horizontal RMDTE (Eqn. 4) was calculated by summing the DTE from each ensemble in the vertical and taking a pressure weighted average (Eqn. 4). This creates a two dimensional horizontal depiction of the ensemble spread growth and evolution. This, while good for diagnosing specific regions of evolving ensemble divergence, does not quantify the temporal evolution of the entire ensemble spread. In order to accomplish this, an area averaged version of the RMDTE was calculated to arrive at a time series of RMDTE throughout the ensemble forecast, which can be described as:

$$RMDTE_t = \sum_{i=0}^{n_{xpoints}} \frac{1}{n_{xpoints}} \sum_{j=0}^{n_{ypoints}} \frac{1}{n_{ypoints}} RMDTE_{i,j,t} \tag{5}$$

where $n_{xpoints}$ is the total number of grid points in the x-direction, $n_{ypoints}$ is the total number of grid points in the y-direction, and $RMDTE_{i,j,t}$ is the solution to Eqn. 4. The solutions resulting from Eqn. 5 yield a time series of the domain averaged RMDTE that is representative of the spread compared to the ensemble mean. This time series creates a simple metric that is used to compare the ensemble spread between different runs and evaluate the results of any ensemble predictability experiments.

Several experiments were designed to test the predictability associated with the convection allowing ensemble performed in this study. The presence of the control member in the Reforecast-2 ensemble allows for calculation of the atmospheric perturbation off the control associated with each member of the ensemble. Once calculated, the perturbation was scaled or altered and added back to the control run to create a new set of ensemble ICs and LBCs still based on the original Reforecast-2 ensemble. For example, the atmospheric perturbation of the ICs and LBCs associated with each ensemble member off the control run were halved (this corresponds to the “Half Magnitude” ICs and LBCs in Table 4.2) to artificially narrow the initial spread of the ensemble. Additionally, various mixtures of scaled ICs and LBCs for each flooding event were created. The newly created ICs and LBCs were used to re-run the ensemble and the resulting RMDTE calculated. Table 4.2 describes the ensemble predictability experiments and their associated ICs and LBCs performed for each case described in the previous section. The last column of Table 4.2 depicts the abbreviations that

Table 4.2. Summary of ICs and LBCs used in ensemble experiments. "Half Magnitude" or "One Third Magnitude" specifically means that the IC or LBC perturbation off the control Reforecast-2 member for each ensemble member was cut in half or one third, respectively. The TX_2km ensemble run uses the same IC and LBCs as TX_control except at 2 km grid spacing.

Case	ICs	LBCs	Short Name
Tropical Storm Erin Initialized 0000 UTC 18 August 2007			
—	Reforecast-2	Reforecast-2	Erin_control
—	Half Magnitude	Half Magnitude	Erin_half
—	Half Magnitude	Reforecast-2	Erin_IC_half
—	Reforecast-2	Control Member LBC	Erin_const_LBC
Texas MCV Initialized 0000 UTC 25 May 2013			
—	Reforecast-2	Reforecast-2	TX_control
—	Reforecast-2	Reforecast-2	TX_2km
—	Half Magnitude	Half Magnitude	TX_half
—	One Third Magnitude	One Third Magnitude	TX_third
Iowa MCS Initialized 0000 UTC 25 June 2015			
—	Reforecast-2	Reforecast-2	Iowa_control
—	Half Magnitude	Half Magnitude	Iowa_half
—	Half Magnitude	Reforecast-2	Iowa_IC_half
Arkansas MCV Initialized 0000 UTC 10 June 2010			
—	Reforecast-2	Reforecast-2	Ark_control
Texas MCV Initialized 0000 UTC 24 May 2013			
—	Reforecast-2	Reforecast-2	TX_24_control
No Upscale Growth Initialized 0000 UTC 10 June 2013			
—	Reforecast-2	Reforecast-2	No_up_control

are used throughout the rest of the manuscript when referring to each run of the ensemble predictability experiments.

The scaling of the ensemble ICs and LBCs allows for the determination of what meteorological factors, in terms of the ICs and LBCs, have the largest impact on the precipitation forecasts for each event. Further, the differences in the precipitation forecasts, or lack their of, between the control ensemble (e.g., Erin_control) and scaled ensemble runs (e.g., Erin_half) can speak to the practical and intrinsic predictability of each extreme precipitation event (e.g., Melhauser and Zhang 2012). Thus, in addition to the evaluation of the overall ensemble spread evolution, some discussion of the meteorological factors that affect or, perhaps surprisingly, do not affect the accuracy of the precipitation forecasts of the ensemble are given. The full model domain RMDTE for the all cases/experiments and the RMDTE for specific regions corresponding to the most extreme precipitation were calculated, which allows for the comparison of the ensemble spread characteristics across different spatial scales, precipitation magnitudes, and synoptic to mesoscale forcing mechanisms. In addition to the regions subsetted over the most extreme precipitation for each case, one region devoid of convection was chosen and the RMDTE calculated for each case. The areas encompassed by the subsetted regions in each case (i.e., Tropical Storm Erin, Texas MCV, and Iowa MCS) were kept equal and those same regions applied to each of the experiments for that case (i.e., Erin_half, Erin_IC_half, and Erin_const_LBC for Tropical Storm Erin). This allowed for direct comparison of the RMDTE between the ensemble experiments performed for each case at both the full domain and regional scales.

Lastly, an effort was made to quantify the spread of the precipitation forecasts for each experiment that would be depicted on a "spaghetti plot" —a single plot that overlays the precipitation accumulation contours for each member on the same chart. This is accomplished using the area spread (AS) metric as defined in Schumacher and Davis (2010), which is calculated by dividing the total area of predicted rainfall by all ensemble members over a specified threshold by the average area over that threshold predicted by each ensemble member. Mathematically this can be expressed as:

$$AS = \frac{\sum_{j=1}^{m} P_j}{\frac{1}{n}\sum_{i=1}^{n}\sum_{j=1}^{m} p_{i,j}}, \text{where } P_j = \begin{cases} 1 & \text{if} \sum_{i=1}^{n} p_{i,j} \geq 1 \\ 0 & \text{otherwise} \end{cases} \tag{6}$$

Here $p_{i,j} = [p_{1,j}, ..., p_{n,j}]$ is the precipitation forecasts for a n-member ensemble at the jth of m grid points which has been converted to a binary grid where $p_{i,j} = 1$ if the forecasted precipitation reaches or exceeds the prescribed threshold and $p_{i,j} = 0$ if it does not. $AS = 1$ is the minimum possible value and is represents the case where all forecast contours exactly overlap. Conversely, $AS = n$, where n=number of ensemble members (11 in this case), is the maximum value possible and represents when none of the ensemble member's forecasts overlap. In other words, higher values indicate more ensemble spread in the precipitation field. The AS metric was then compared to the RMDTE to see if overall ensemble spread is directly comparable to forecasted precipitation spread.

4.2. Terrain Induced Variability of Extreme Precipitation

In this section, the numerical model architecture, model initial and boundary conditions, and terrain modification procedure for the terrain induced precipitation variability experiments are presented.

4.2.1. Numerical Model Architecture. To test the influence of the Balcones Escarpment on the intensity and distribution of precipitation in central Texas, version 3.6 of the Advanced Research core of the Weather Research and Forecasting model (Skamarock et al. 2008) is used to conduct numerical simulations of these three cases. All simulations use 4-km horizontal grid spacing and 50 vertical levels on a stretched grid ($\Delta z =\sim$ 50m near surface, $\Delta z =\sim$ 600m aloft) with a model top of 50 hPa. For the 9 June 2010, 25 May 2013, and 31 October 2010 cases, a control and a terrain-modified model run, in which the Balcones Escarpment is removed, are performed. Identical lateral boundary conditions (LBCs) and model physics (Table 4.3) are used across both the control and terrain-modified simulations, and the initial conditions (ICs) are identical except for the minor changes related to the terrain modification discussed below. The extent of the model domain used is illustrated in Fig. 2.9.

Table 4.3. WRF-ARW model configuration for Balcones Escarpment Experiments

Parameter	Configuration
Horizontal grid	649 X 649, $\Delta x = 4$km
Vertical grid	50 levels, $\Delta z =\sim$ 50m near surface, $\Delta z =\sim$ 600m aloft
Cumulus Scheme	None
PBL Scheme	YSU (Hong et al. 2006)
Microphysics	Morrison 2-moment (Morrison et al. 2009)
Radiation	RRTMG (Iacono et al. 2008)
Land Surface Model	Noah (Chen and Dudhia 2001)

4.2.2. Boundary and Initial Conditions. The ICs and LBCs for the aforementioned events are chosen based upon the parent model's depiction of the precipitation field in order to obtain a control run that reasonably simulated the observed precipitation. The ICs and LBCs for the 25 May 2013 and 31 October 2013 cases were obtained, similar to the ensemble predictability experiments, from members of the Reforecast-2 ensemble described earlier (Table 4.4) (Hamill et al. 2013). The ICs and LBCs for the 9 June 2010 case were obtained from a member of one of the ensembles described by Schumacher and Clark (2014), namely member 20 of the "single_24hr" configuration (Table 4.4). This member was found to have the heavy precipitation in approximately the same location as it was observed, and was used because none of the Reforecast-2 ensemble members provided an accurate precipitation forecast at lead times of interest to this study. Each model simulation is initialized at 0000 UTC (Table 4.4) and run for either 48 (9 June 2010; 31 October 2013 cases) or 24 hours (25 May 2013 case). The heaviest precipitation associated with each event began at least 6 hours into the numerical simulation, which allowed the model to come into balance with the new topography.

TABLE 4.4. Model initialization times and boundary conditions

Case	Boundary Conditions	Initialization Time
9 June 2010	Schumacher and Clark (2014), "single_24hr", Member 20	0000 UTC 8 June 2010
31 October 2013	Reforecast-2, Member 2	0000 UTC 30 October 2013
25 May 2013	Reforecast-2, Member 9	0000 UTC 25 May 2013

4.2.3. TERRAIN MODIFICATION PROCEDURE AND EXPERIMENT DESIGN. In order to remove the Balcones Escarpment and not introduce model physical imbalances, the terrain modification is done prior to the execution of the WRF-ARW preprocessing for the October and May 2013 cases. The terrain was manually removed after this step for the June 2010 case, since the initial conditions were derived from model runs already completed from another study on this event. The underlying model terrain is specified at a ten arc-minute resolution taken from the standard WRF-ARW geography files to create a slightly smoothed terrain field for modification. The Balcones Escarpment is removed in the model by extending the Texas Coastal Plain westward from Houston to Del Rio and northward to the Red River at the Texas-Oklahoma border (Fig. 2.9b). A slight terrain gradient approximately equal to the slope from the Gulf of Mexico to the Balcones Escarpment is maintained through the entire region of terrain modification to ensure the proper representation of an extension of the Texas Coastal Plane (Fig. 2.9d). At the grid points where the model terrain is lowered, atmospheric information must be supplemented from the parent model initial conditions to "fill in" the atmosphere that was previously below ground. This is accomplished by obtaining pressure level information that was previously below ground from the parent model, which contains information on all pressure levels even if below the terrain surface. The initial thermodynamic data on these pressure levels in the model is obtained from the U.S. Standard Atmosphere, and the wind at the lowest pressure level above ground is applied at all levels that were previously below ground but now above. Similar terrain modification procedures have been used previously in Alcott and Steenburgh (2013), Schumacher et al. (2015), and Morales et al. (2015). Figure 2.9 depicts the prescribed model elevation used in the control and terrain-modified runs, as well as the extent of the model domain.

In order to rule out the possibility that changes in precipitation were associated with random chance, experiments were carried out on the 25 May 2013 case in which the perturbations to the initial atmospheric conditions were reduced in magnitude. The LBCs and ICs for this case were obtained from member nine of the Reforecast-2 ensemble, which allowed for the determination of the IC and LBC perturbation off the control for this member. The original IC and LBC perturbation was scaled by 0.5 and 0.75 to create two modified sets of ICs and LBCs for the 25 May 2013 case. These ICs were used to perform two additional experiments, as described above, containing a control and terrain-modified run, where the Balcones Escarpment was removed. This in total, for the 25 May 2013 case, created three numerical experiments based upon scaled perturbation versions of the same Reforecast-2 ensemble member ICs. Any precipitation shifts associated with the removal of the Balcones Escarpment in these three runs for the 25 May 2013 case were then analyzed, along with a closer look at relevant meteorological differences. Furthermore, the entire Reforecast-2 ensemble (all 11 members) for this day was run in a similar WRF-ARW configuration to quantify the atmospheric variability associated with this event.

CHAPTER 5

Results: Ensemble Predictability Experiments

The following sections present the ensemble spread evolution results for the experiments performed on Tropical Storm Erin, the Texas MCV, and Iowa MCS. Some discussion of the each member's event total precipitation and apparent associated differences will also be presented for the control ensemble run only.

5.1. Tropical Storm Erin, August 2007

The ensemble for the Tropical Storm Erin case was initialized (at 0000 UTC 18 August 2007) with the associated vortex already present in the model initial conditions located inland over west Texas. There was some slight difference in the location of the vortex at initialization between the different ensemble members, and many members were located generally to the south and east of the analyzed best track location at the time (Fig. 5.1). As time progressed through each ensemble member's respective forecast, divergence in Erin's vortex tracks occurred. Almost all of the members moved the vortex center over the next 42-hr south and east of the National Hurricane Center (NHC) best track analysis (Knabb 2008). Furthermore, many of the members showed Erin recurving much slower than the NHC analysis with some members stalling in west Texas (Fig. 5.1). This was shown also to be true in the GFS initialized controls runs performed in Schumacher et al. (2011) and Evans et al. (2011). However, three members continued to keep the vortex on a faster northeasterly track into north central Oklahoma (most northern three members in Fig. 5.1).

The precipitation forecasts varied between each member of the control ensemble; however, consistent features were predicted across all of the members. The main point of variability in the precipitation forecasts is associated with differences in the track of Erin's central vortex.

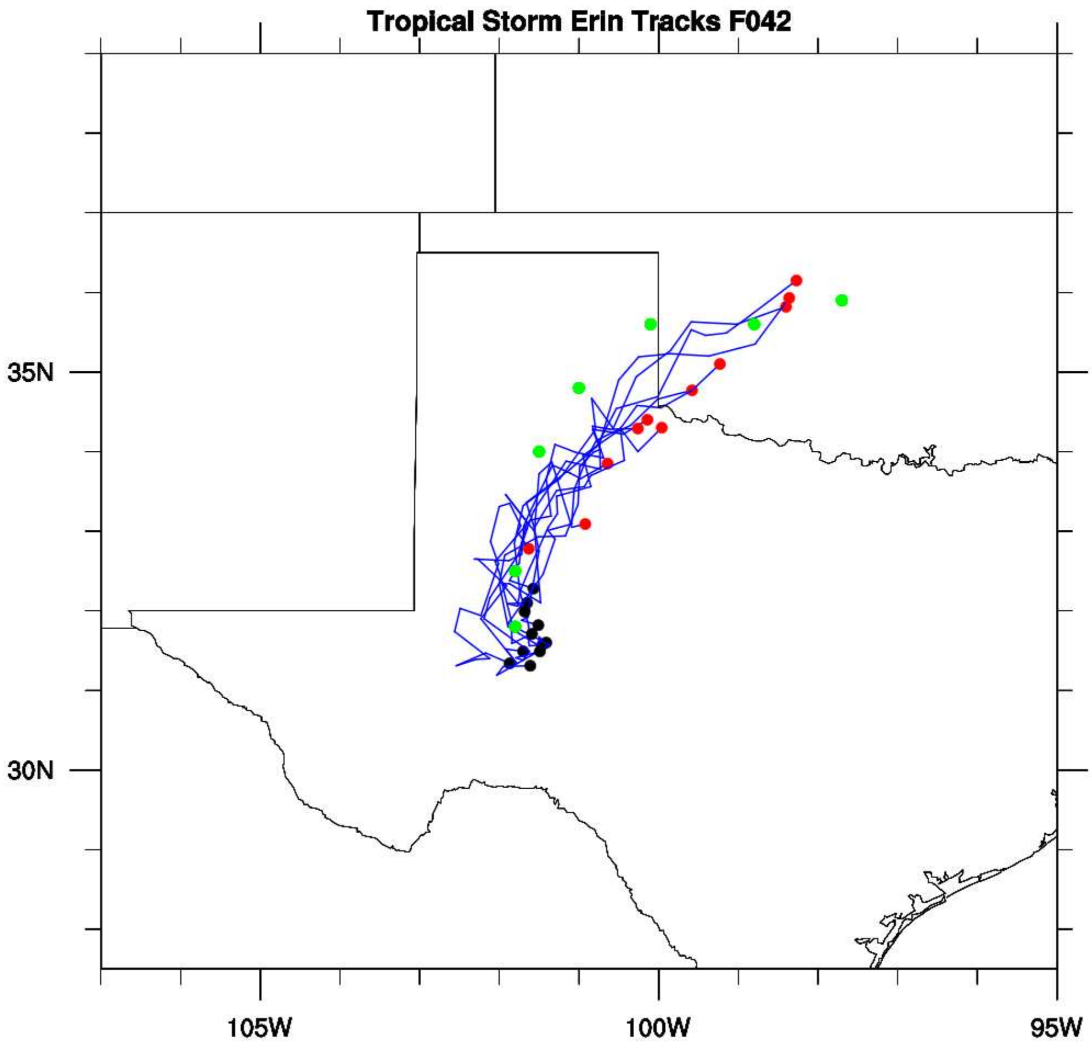

FIGURE 5.1. Tropical Storm Erin central vortex tracks valid through the 42-hr forecast for each member of the control ensemble. Vortex center was determined by the location of highest averaged vorticity between the 500-700 hPa levels. Black dots represent the initialization point of Erin in each ensemble, blue lines are the tracks, and red dots represent the vortex center at 42-hr into the forecast. Green dots represent the NHC best track analysis.

Members that had Erin moving slower over the period had more precipitation accumulation in west Texas and less or none (e.g., Fig. 5.2b-e,g,i-k) over the observed area high accumulations in central Oklahoma (Fig. 5.2l). Further, those members that kept Erin located in west Texas developed a local maximum of precipitation higher than the observations along the eastern Kansas border (e.g., Fig. 5.2b-e,g,i-k). The PRE associated with Erin, located

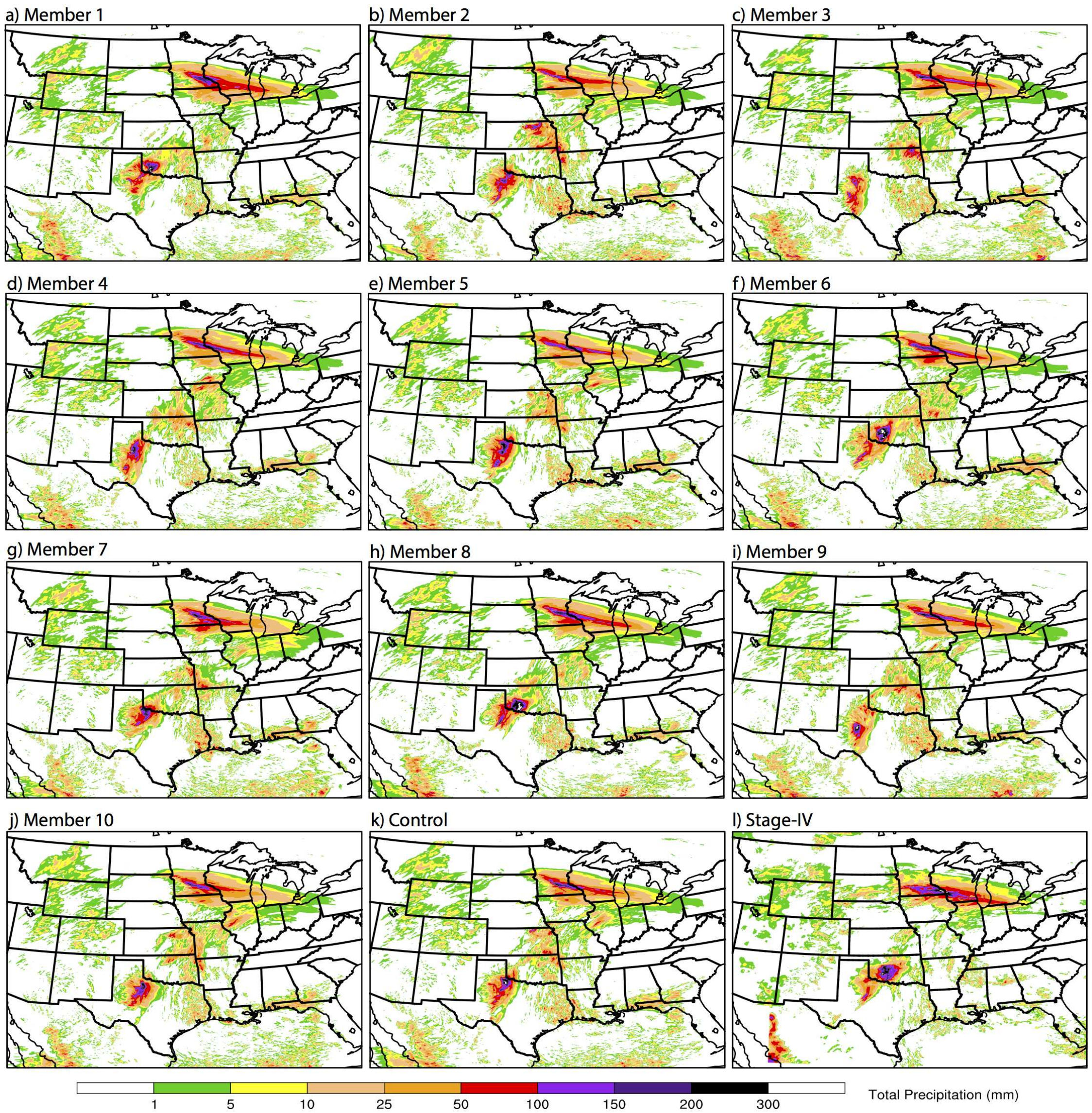

FIGURE 5.2. Erin_control contoured accumulated precipitation valid for the 24-hr period ending 1200 UTC 19 August 2007 for each member of the ensemble, including the control. (a)-(j) correspond to members 1-10 of the ensemble, respectively. (k) corresponds to control member of the ensemble, and (l) is the Stage-IV gridded analysis valid over the same period.

in southern Minnesota and into Wisconsin, is spatially well represented across all the ensemble forecasts, despite the significant variability in the actual track of Erin (Fig. 5.2). The ensemble member forecasts move the PRE slightly north of the Stage-IV observations and have lower total accumulations through the swath as well. However, the consistency of the PRE across all of the members in the control ensemble shows that the creation of a downscaled convection allowing ensemble, despite relatively few members, can add predictive utility to cases of extreme rainfall by adding increased confidence (or, conversely, decreased confidence) of the occurrence of an extreme precipitation event , such as the PRE discussed here.

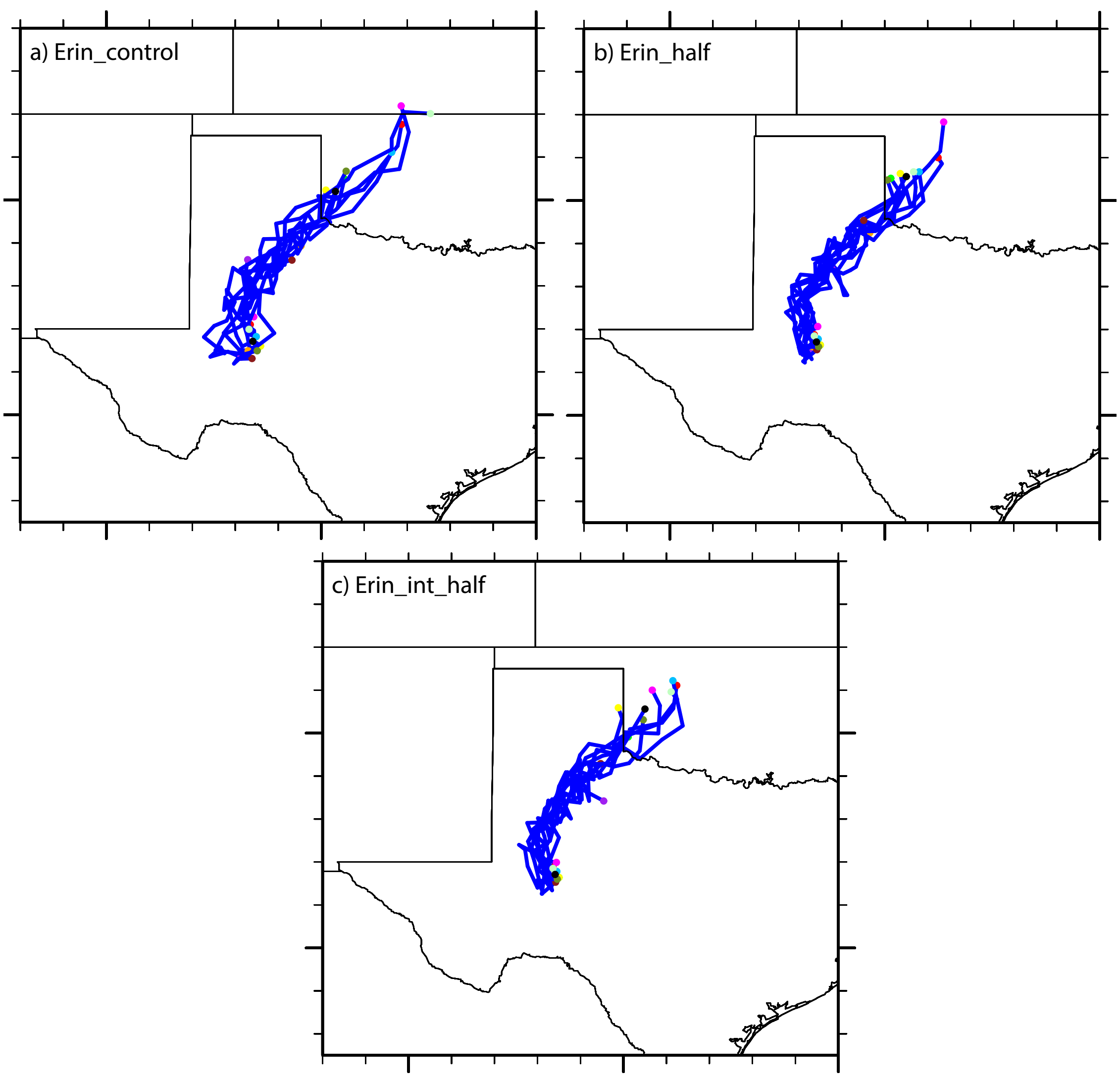

FIGURE 5.3. Tropical Storm Erin central vortex tracks valid through the 48-hr forecast for each member of Erin_control (a), Erin_scaled (b), and Erin_IC_half (c). Vortex center was determined by the location of highest averaged vorticity between the 500-700 hPa levels. Blue lines represent vortex tracks and colored dots correspond to start and ending location of the vortex center of each ensemble member.

The full vortex tracks for Erin_control, Erin_half, and Erin_IC_half are presented in Fig. 5.3 and reveal a dependence of Erin's forecasted track on the respective ensemble ICs. The Erin_control ensemble has Erin's final position fairly evenly distributed along the envelope of possible forecasted tracks (Fig. 5.3a). When the member tracks between Erin_half and Erin_IC_half are compared, there is very little difference between the two ensembles with a large clustering of final positions in western Oklahoma east of the Texas panhandle (c.f., Fig. 5.3b and Fig. 5.3c). Erin_half and Erin_IC_half have different LBCs (Full perturbation off the Reforecast-2 control in Erin_IC_half and half perturbation off the control in Erin_half) and the same ICs (half perturbation off the control), yet similar forecasted final positions were produced in the simulations. Further, the only difference between Erin_control (Fig. 5.3a) and Erin_IC_half (Fig. 5.3c) is the scaling of the IC perturbations by half in Erin_IC_half. The large difference between Erin_control and Erin_IC_half with only the ICs changed for the three northernmost members in Erin_control (Fig. 5.3 pink, red, and very light green members) and the similarities between Erin_half and Erin_IC_half with the same ICs (but difference LBCs) for the same members, led the author to believe that Erin's track was more sensitive to differences in the ICs than the LBCs for these three members that took Erin the farthest north in Erin_control.

The influences of the ICs on the forecast track of Erin were investigated to discern the synoptic scale differences that develop from scaling the IC perturbations by half and led to the changes in Erin's final forecast position seen between Erin_control and Erin_IC_half. The accumulated precipitation fields for members 1, 6, and 8 from Erin_control and Erin_IC_half illustrate the significant differences in the vortex motion between the different ensemble runs (Fig. 5.4). However, very little difference was seen in both the spatial expanse and the magnitude of the PRE across all of the ensemble experiments (e.g., Erin_IC_half, Erin_half,

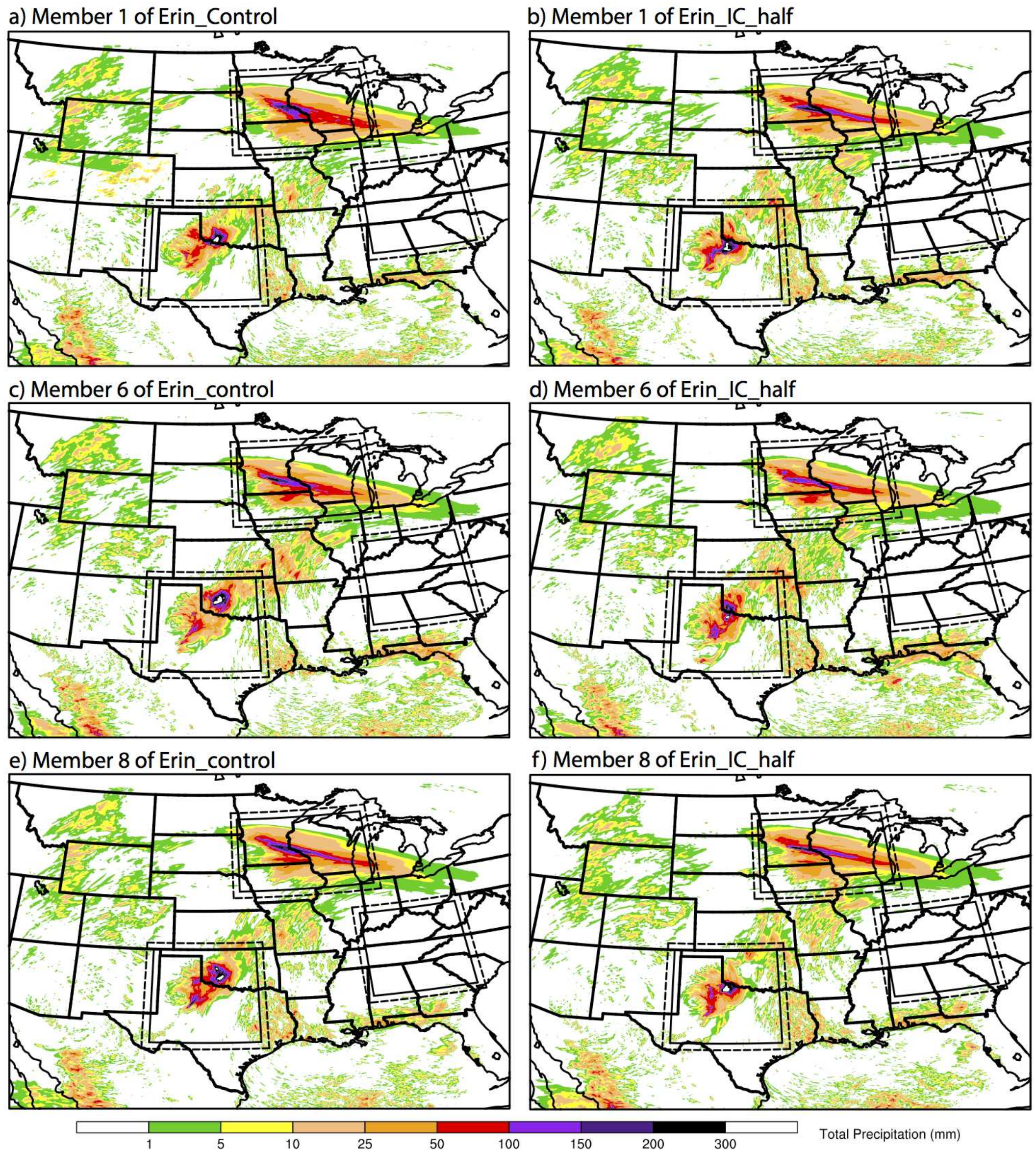

FIGURE 5.4. Erin_control (first column) and Erin_IC_half (second column), contoured accumulated precipitation from members 1 (a,b), 6 (c,d), and 8 (e,f) valid for the 24-hr period ending 1200 UTC 19 August 2007. Boxes indicate regions of equal area associated with Erin's vortex (centered in northern Texas), the PRE (centered on Wisconsin-Minnesota Border), and a region devoid of convection called NOCON (centered in Tennessee) over which the AS metric (solid boxes) and regional RMDTE (dashed boxes) are calculated.

and Erin_const_LBC), which may hint at the model being underdispersive in this region (e.g., Fig. 5.4). The precipitation forecasts produced by members 1, 6, and 8 in Erin_IC_half do not show the northeastward progression of the vortex that is seen by the same members in

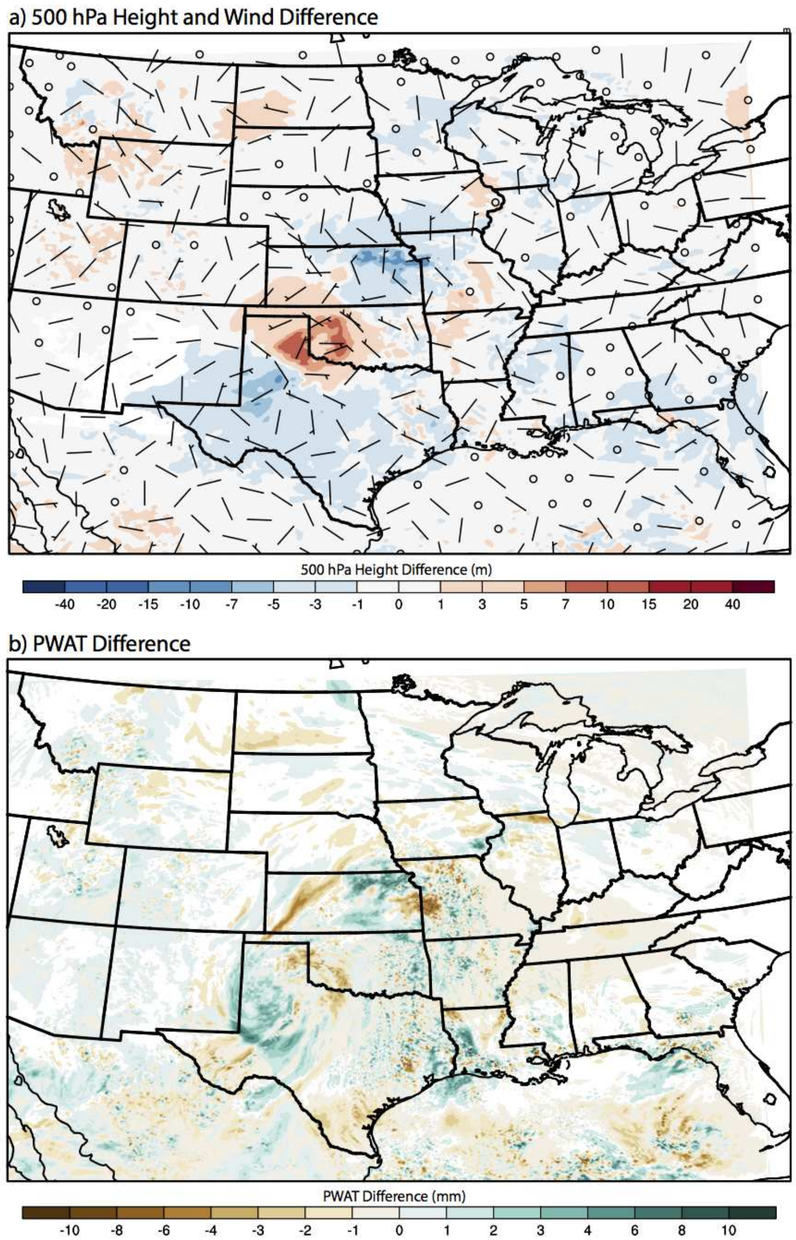

FIGURE 5.5. Contoured precipitable Water (PWAT) (b), countered 500 hPa height (a), and wind difference (wind barbs) (a) fields between the mean of members 1, 6, and 8 from Erin_IC_half and Erin_control. Differences are Erin_IC_half minus Erin_control valid a 2000 UTC 18 August 2007, forecast hour 20.

Erin_control (c.f., left and right columns of Fig. 5.4). The ensemble mean of these three members (1, 6, and 8) that forecasted Erin moving the farthest north (i.e., nearest the last point in the NHC best track) in Erin_control were taken and subtracted from the mean of

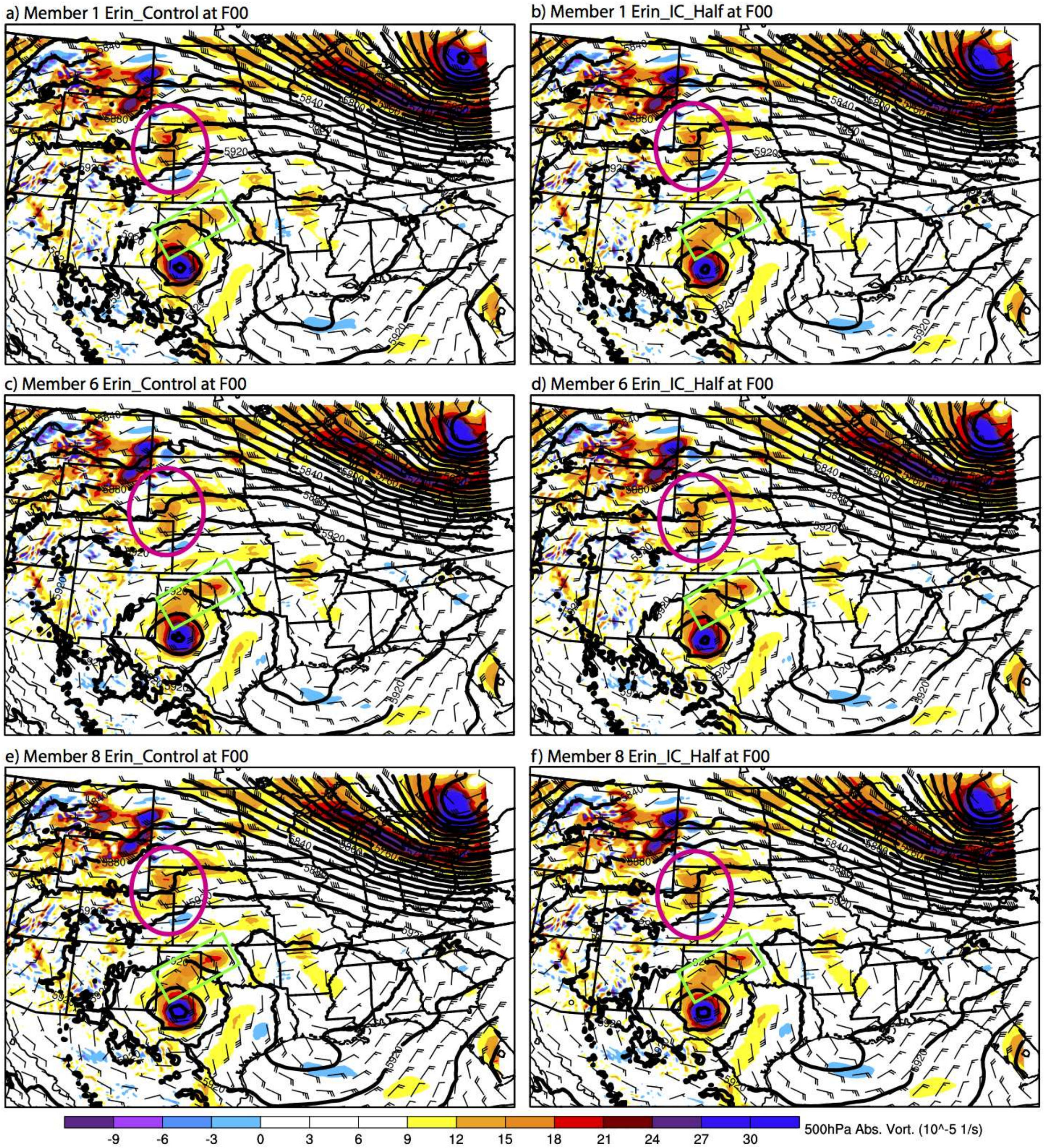

FIGURE 5.6. 500 hPa absolute vorticity (colored contours) and height (black contours every 20 m) valid at 0000 UTC 18 August 2007 (Ensemble initialization, F00) for Erin_control (left column) and Erin_IC_half (right column) for members 1 (a,b), 6 (c,d), and 8 (e,f). Pink circle corresponds to specific shortwave of interest, and green box corresponds to curvilinear vorticity outflow band associated with Tropical Storm Erin.

the same three members in Erin_IC_scaled. The mean difference fields for 500 hPa height and PWAT highlight two main regions of significant difference that develop by 2000 UTC on 18 August 2008. The first, located in the Texas panhandle, as denoted by the dipole in both the 500 hPa and PWAT fields (Fig. 5.5a,b), is associated with a shift in the vortex center to the southwest in Erin_IC_half compared to Erin_control, which is expected because it is the difference between the runs that is being investigated. The second is located in eastern Kansas, northeastern Oklahoma, and western Missouri where a lowering of 500 hPa heights in Erin_IC_half is seen along with a dipole in the PWAT fields (Fig. 5.5a,b). This is associated with increased precipitation accumulation in this area compared to Erin_control that develops in members 1, 6, and 8 when the initial conditions are scaled in Erin_IC_half (Fig. 5.4). A similar signature is also present in the members of Erin_control that produce a slower motion of Erin's vortex as well (e.g., Fig. 5.2b-e,g,i-k). This hints that the increase in precipitation accumulation in this region and the reduced northeastward motion of Erin are related.

A closer look at the initial conditions for members 1, 6, and 8 both Erin_control and Erin_IC_half reveal slight differences in the strength and position of the vorticity signature of Erin's outflow. These three members in both Erin_control and Erin_IC_half both have curvilinear outflow vorticity bands of slightly varying strength stretching from Erin to the northeast (enclosed by green box in Fig. 5.6); however, the vortex centers are slightly further south in Erin_IC_half (Fig. 5.3). Further, there are differences in the strength of the shortwave trough located in the panhandle of Nebraska (enclosed by pink circle in Fig. 5.6). It appears to be slightly stronger in Erin_control, specifically members 1 and 8 (Fig, 5.6a,e). As the simulations go on, the interactions between the outflow structure and the shortwave affect the speed at which Erin recurves. In members 1, 6, and 8 in Erin_control both the outflow band and the vortex center are able to interact with the shortwave embedded in the zonal flow (Fig.5.7a,c,e). The convection that develops on the northeast side of the storm deepens the shortwave and accelerates the recurvature of Erin (Fig. 5.7a,c,e), since

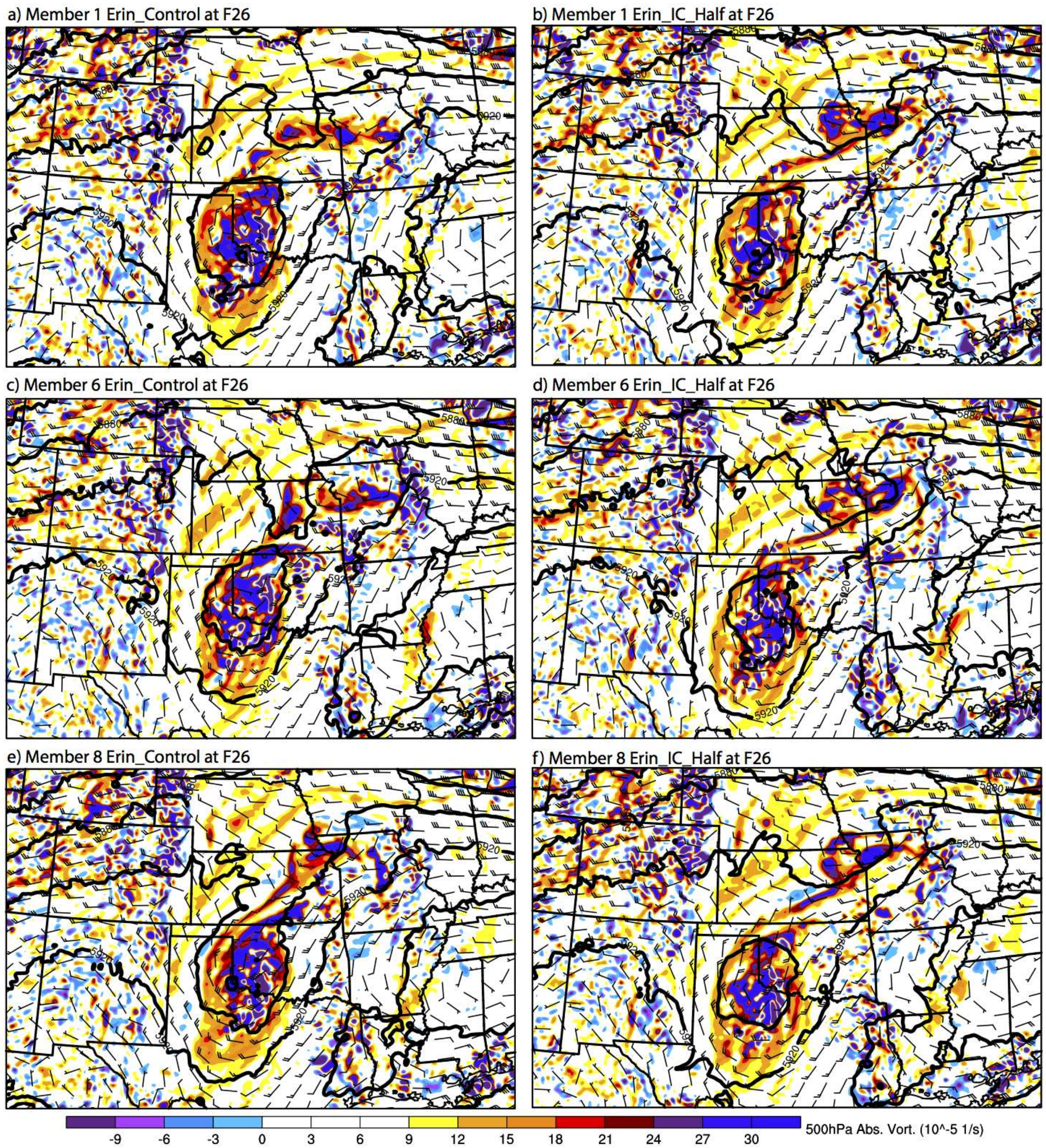

Figure 5.7. 500 hPa absolute vorticity (colored contours) and height (black contours every 20 m) valid at 0200 UTC 19 August 2007(F026) for Erin_control (left column) and Erin_IC_half (right column) for members 1 (a,b), 6 (c,d), and 8 (e,f).

the central vortex of Erin is interacting with the shortwave. When the IC spread is reduced for members 1, 6, and 8 in Erin_IC_half, the curvilinear vorticity signature is influenced by the shortwave and Erin's central vortex does not seem to be (i.e., the curvilinear vorticity band is accelerated eastward by the shortwave and Erin's center is not). This has the effect of reducing the shortwave's steering impact on Erin's central vortex and induces deeper convection, compared to the same members in Erin_control, in eastern Kansas, likely due to this vorticity structure being farther removed from the influence of Erin's vortex (Fig. 5.7b,d,f). This, in turn, deepens and increases the eastward propagation of the shortwave more than what is seen in Erin_control and further removes Erin from the influence of the mean flow, which slows Erin's recurvature (Fig. 5.7b,d,f). In other words, Erin's motion was highly sensitive to how far north the vortex was initialized and the strength of the shortwave originally located in the Nebraska panhandle. That is, the further north (south) Erin and the stronger (weaker) the shortwave were initialized, the quicker (slower) Erin recurved (c.f., Fig. 5.7a to b, c to d, and e to f).

A total of three ensemble simulations, in addition to the control (Erin_control), were performed on the Reforecast-2 data for the Tropical Storm Erin case: Erin_half, where the IC and LBC perturbation off the control for each member were halved; Erin_IC_half, where only the IC perturbation off the control of each member was halved; and Erin_const_LBC, where the control member LBCs were prescribed for each unique ensemble member IC. The time series of the domain averaged RMDTE is presented in Fig. 5.8. A more muted diurnal cycle on the ensemble spread is observed across all ensembles run for Erin (solid color lines in Fig. 5.8) compared to all of the ensemble runs performed across various cases (solid grey lines in Fig. 5.8). The spread growth minimum occurs in the the pre-convective hours, and maximizes during the convectively active times, which are denoted by increases in the percentage of convective points in Erin_control plotted at the bottom of Fig. 5.8. Further, the spread growth slightly dampens after convection but does not saturate in the Erin_control run (see flattening of green line from ∼24–30 hours in Fig. 5.8). The more muted diurnal cycle seen over the full domain for Erin is likely due to

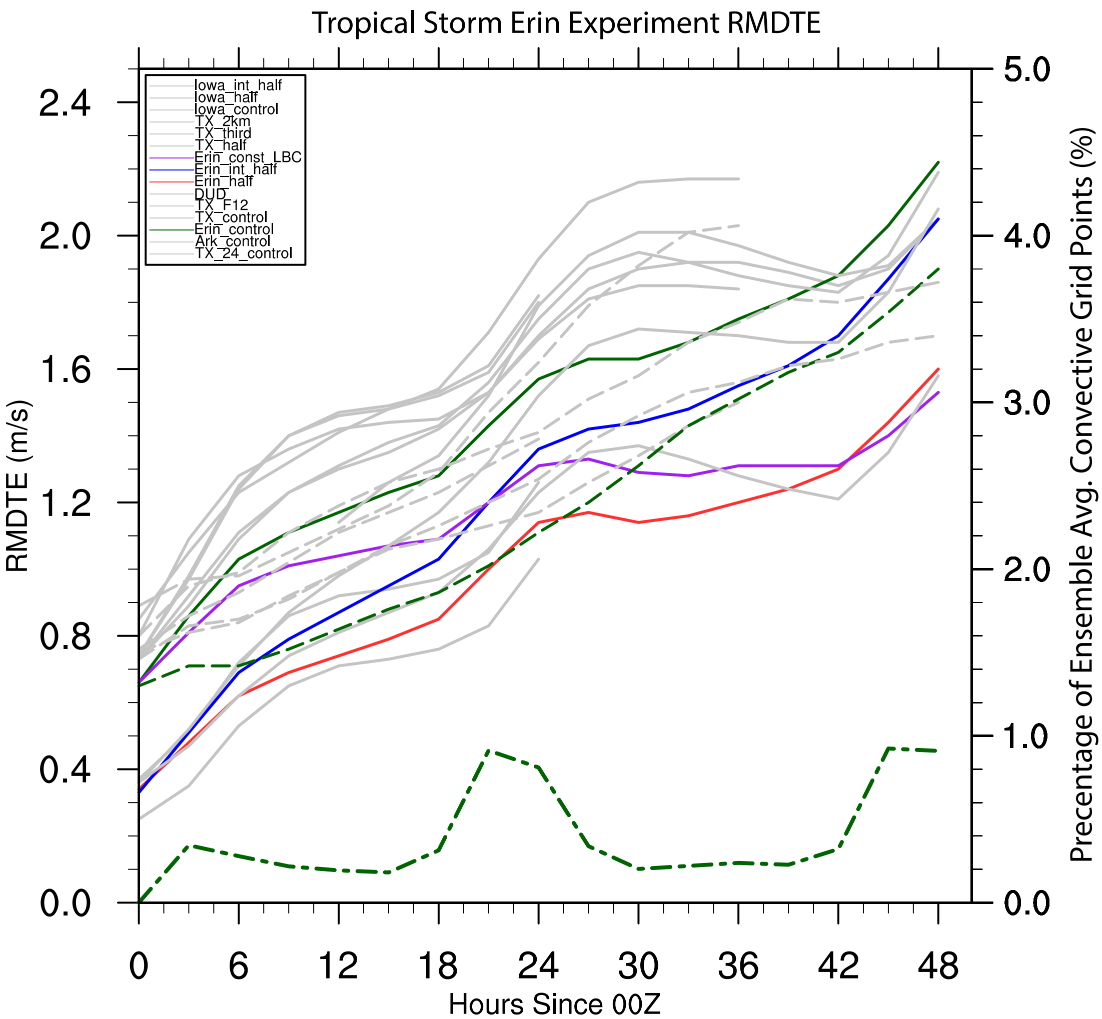

FIGURE 5.8. Time series of the domain averaged RMDTE highlighting the ensemble simulations for the Tropical Storm Erin case. Colored lines correspond to Erin_control (green), Erin_half (red), Erin_IC_half (blue), Erin_const_LBC (purple), and RMDTE from native Reforecast-2 resolution (dashed green). Grey lines represent the RMDTE time series for all of the other ensemble simulations in this study for comparison. Dot-dashed green line at bottom of graph corresponds to percentage of ensemble average grid points that exceed 1 m/s of vertical velocity (w) at 700 hPa (right vertical axis) in Erin_control to denote convectively active times.

convection continuing throughout the day near the vortex center. However, despite the constant source of convection associated with Erin (which can be thought of as a constant source of upscale error growth), the presence of even a slight diurnal cycle shows that the large scale meteorological characteristics and features continue to affect the evolution of smaller scale features. Additionally, the diurnal cycle is almost non-existent for Erin in the ensemble spread evolution of the native Reforecast-2 ensemble (green dashed line in Fig. 5.8), which is likely due to convection being parameterized and the finer scale motions not being as well resolved, compared to the convection-allowing ensemble. Spread growth rates between the Erin_control run (green line) and the native Reforecast-2 ensemble (green dashed line in Fig. 5.8) are similar, despite significant differences in resolution, except for a large increase in the first six hours, due to the 4 km runs spinning up to resolve smaller scales, and a slight increase during peak convective times of Erin_control (Fig. 5.8) (e.g., Clark et al. 2009). This further implies that the large-scale atmospheric features, which are resolved by the individual members at the native Reforecast-2 resolution, have a larger constraint on the overall evolution of the forecasts compared to the upscale error growth from moist convection.

Since the IC but not the LBC perturbations were scaled by half in the Erin_IC_half run (blue line in Fig. 5.8), the lower ensemble spread it has compared to Erin_control at forecast hour forty-eight implies that the choice of the ICs still has an impact on the forecast through at least two convective cycles in this case. Lastly, when the control member boundary condition is imposed on all members, in Erin_const_LBC (purple line in Fig. 5.8), the overall spread is reduced compared to Erin_control; however, only slightly smaller growth rates compared to Erin_control remain during convective times (at ∼24-hr and 48-hr). This shows, despite the same LBC forcing driving all the members of the ensemble, that spread growth due to convection and varying initial conditions is still seen throughout the entire forecast period, which illustrates the impact of smaller scale differences on the spread evolution of the ensemble.

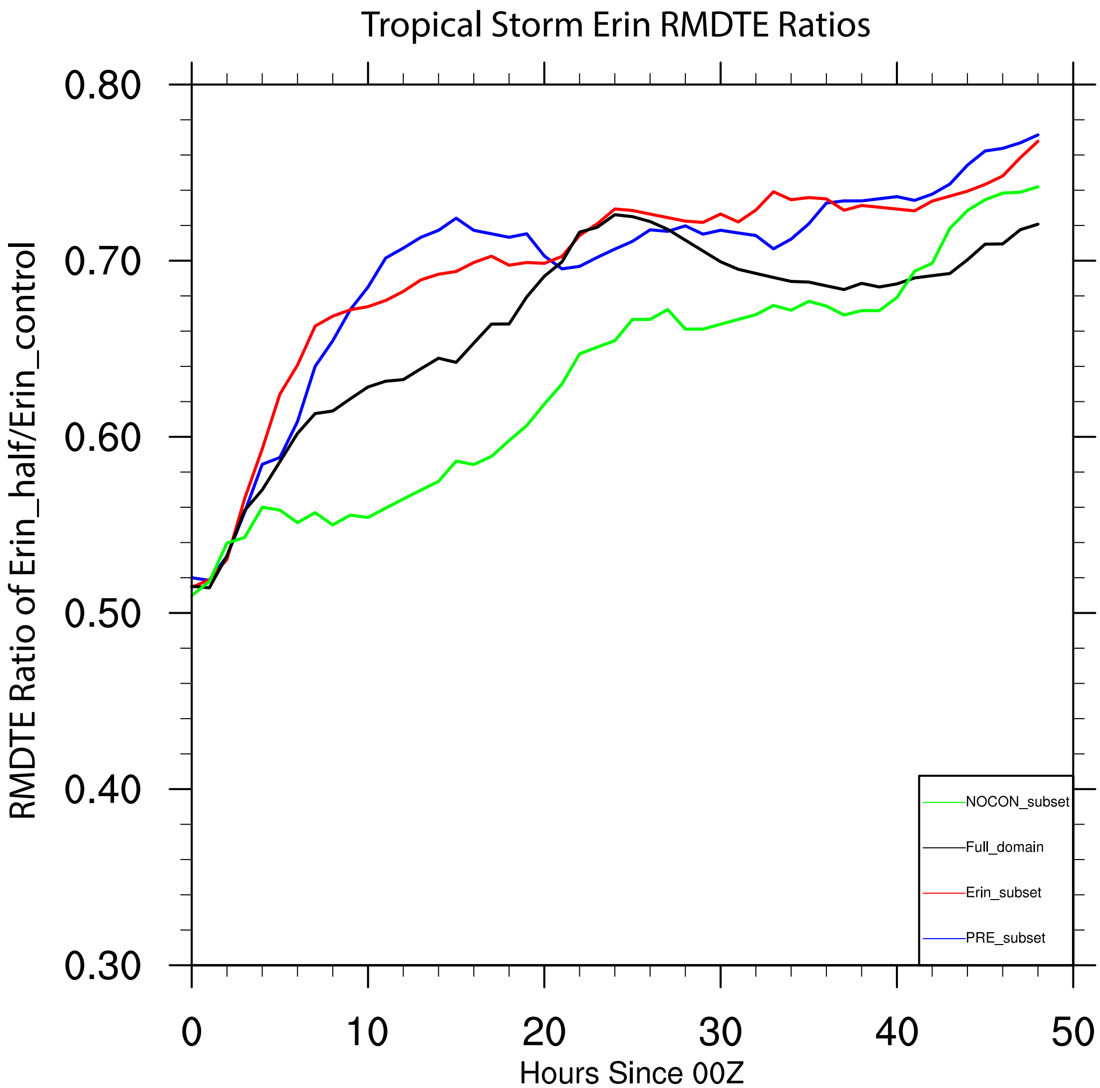

FIGURE 5.9. RMDTE ratio time series for Erin_half over Erin_control for the full ensemble domain (black line), area devoid of convection (green), region bounding the Tropical Storm Erin vortex (red), and the associated Predecessor Rain Event (PRE) (blue).

The scaled ensemble experiments allow for the characterization of the linearity of the ensemble spread for a specific meteorological case. If the error growth was linear (i.e., corresponding to a case at the theoretical limit of practical predictability), the ratio (depicted in 5.9) of the scaled run (Erin_half) over the control (Erin_control) should stay approximately at the factor by which the perturbations were reduced; if the error growth is entirely driven by convection (i.e., the case is purely limited by intrinsic predictability), then the ratios would immediately approach one during the first convective cycle; and, if the spread growth is not purely linear or governed totally by convection (i.e., both intrinsic and practical predictability are influencing the results), the ratio should increase somewhere between the two previous ends of the spectrum. A decrease, in this case, proportionate to the scaling of the ensemble ICs and LBCs in the ensemble spread between the runs of Erin_control and Erin_half over the full domain (black line in Fig. 5.9) is seen at the initial time periods. The linear scaling is, however, not maintained through all forecast times with a steady increase of the ratio of RMDTE between Erin_half to Erin_control seen over the full domain (black line in Fig. 5.9), which implies the RMDTE of Erin_half is increasing faster than Erin_control. There is a slight decrease in the ratio after the the first convective cycle, likely owing to the decrease in convection over the entire domain. This shows that the chaotic moist convective dynamics in Erin_half continue to increase the model spread through time over the exact linear scaling regime. The large overall decrease in the RMDTE time series from Erin_control (green line) to Erin_half (red line in Fig. 5.8) illustrates the importance of the large scale atmospheric forcing on the overall spread growth and magnitude of the ensemble, but the steadily increasing RMDTE ratio between Erin_half and Erin_control shows that upscale spread growth due to the resolution of smaller scales, such as convection, is still present and non-linear. While the ratio of the full domain RMDTE between Erin_half and Erin_control depicts the overall ensemble spread characteristics, this ratio will be used on a regional scale below to discern the practical and intrinsic predictability characteristics of specific precipitation events within the Erin simulations.

Three separate regions of equal area were subsetted from each of the Erin ensemble experiments for a closer look at the spread characteristics of different meteorological scenarios. The three regions applied to all of the ensemble runs are highlighted in Fig. 5.4 by the

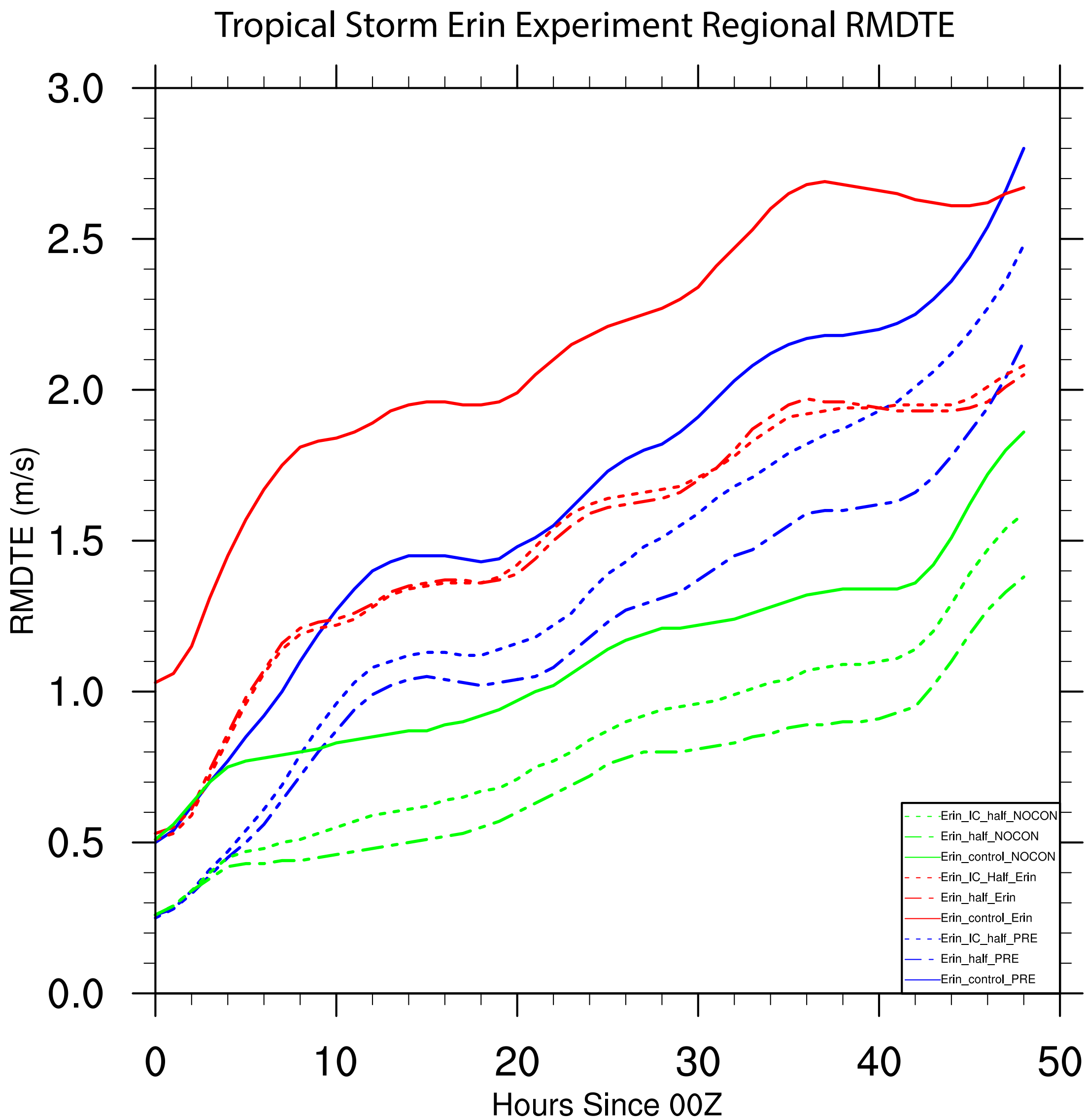

FIGURE 5.10. RMDTE time series for Erin_control (solid lines), Erin_half (dot-dashed lines), and Erin_IC_half (dotted lines) for NOCON regional subset (green), Erin subset (red), and PRE subset (blue) as defined by dashed boxed regions centered in Tennessee, Texas, and the Wisconsin-Minnesota border, respectively, in Fig. 5.4.

dashed-boxed regions. The region centered in Texas encompasses the evolution of Tropical Storm Erin (for the rest of this section will be referred to as the "Erin subset"), the region centered near the Minnesota-Wisconsin border bounds the main region of precipitation associated with the PRE (will be referred to as the "PRE subset"), and a region containing little to no convection centered on the Tennessee Valley (referred to as "NOCON subset"). The results of the subsetted RMDTE depict various characteristics about the spread evolution of each subsetted region. The Erin subset for Erin_control initializes with more RMDTE than the other two regions (Fig. 5.10), likely due to the high energy present in the area associated with Erin's vortex. Interestingly, the Erin regional RMDTE traces for Erin_half and Erin_IC_half lay almost on top of one another, further confirming the sensitivity of Erin's evolution to the initial conditions (Fig. 5.10, red dot-dashed and dotted lines). The NOCON (solid green line in Fig. 5.10) subset of Erin_control maintains a lower spread compared to the PRE (solid blue) and Erin (solid red) subset of the same ensemble, which makes intuitive sense because there is no heavy precipitation within its bounds. Further, there is more spread in the Erin region compared to the PRE (Fig. 5.10), even though similar convective precipitation accumulations and a large spatial coverage are found in the PRE subset. This could be a representation of possible underdispersive tendencies along surface baroclinic zones in this ensemble, or very high confidence in the particulars of the rain event. The AS metric for these two regions follows a similar pattern as the RMDTE. The AS from the Erin subset is larger than that for the PRE region (Table 5.1), as the RMDTE is larger during the time of heaviest rainfall over the Erin vortex. Additionally, the general evolutions of the RMDTE in Erin_IC_half and Erin_half runs for the PRE and NOCON regions follow general patterns seen on the full domain (e.g., Fig. 5.8).

Table 5.1. Area spread (AS) metric for regions in ensemble experiments above 25.0 mm and 50.0 mm precipitation accumulation thresholds. Accumulation period corresponds to windows of most intense rainfall previously identified in Fig. 3.2, and regions correspond to those identified and encompassed by solid boxes in Fig. 5.4.

Case	Region	25.0 mm	50.0 mm
Erin_control	Erin	3.0	3.7
–	PRE	1.7	2.5

The lack of a clear diurnal cycle in the RMDTE on these regional scales (Fig. 5.10) is an important factor to note. As discussed above, the diurnal cycle in the ensemble spread shows the importance of the large-scale atmospheric forcing in not allowing the error growth associated with moist convection to cause rapid divergence of the ensemble members. It could also be thought of as how convective motions transfer energy upscale and, thus, increase the ensemble RMDTE (spread) until the governing large-scale atmospheric characteristics constrain the spread growth. In both the Erin and PRE subsets of Erin_control, convection occurs throughout the majority of the period, which is one way to view the lack of a diurnal cycle. However, for convection to occur over a multi-day period, large to mesoscale forcing must be involved to maintain the ingredients needed for moist convection. Thus, the lack of a diurnal cycle of RMDTE in the Erin and PRE subsets that contain heavy precipitation could be interpreted as situations where there is an increased interaction (energy transfer) between the convective and large-scale atmospheric forcing. This increased interaction drives faster spread growth rates in these regions compared to the full model domain (e.g., Fig. 5.8) or regions devoid of convection (Fig. 5.10 solid green line).

The ratios between the subsetted regions of Erin_control can be used to look further into predictability of this case in different regions of the domain. It is important to note that specific simulated cases can be limited by practical predictability (i.e., ICs and NWP model are not perfect), intrinsic predictability (i.e., the real solution cannot be encompassed by a perfect NWP model and ICs due to chaos), or both at varying levels of influence. In a perfectly theoretical sense, if a meteorological case is at the pure limit of practical predictability (i.e., perfect NWP model), a decrease in the spread of the ensemble perturbations should result in a proportionate decrease in the ensemble spread over time (i.e., the beginning and end RMDTE are scaled by the proportion of the perturbation scaling). This is not seen in the experiments performed for Erin, since the ratio of RMDTE for Erin_half to Erin_control do not remain constant (Fig. 5.9) across the full domain or any of the subsetted regions. In fact, there is a steady increase in the ratio, which implies that the RMDTE in Erin_half is increasing faster than in Erin_control. Furthermore, this rate of increase occurs at different rates depending on the region of interest in the domain (Fig. 5.9). This implies that this modeling system is not at the pure limit of practical predictability and could be improved by advancements in data assimilation, numerics, and parameterizations, among others. It does not mean that the forecast is not improved by reducing the initial uncertainty; it just means that model ICs, physics, and numerics can still be improved. However, the faster increase in RMDTE in Erin_half could also, in addition to practical predictability issues, be caused by approaching, to some degree, the intrinsic predictability limit. If an ensemble system and specific case of interest were limited completely by intrinsic predictability, a scaled decrease in the IC spread would result in a similar spread at the end of the simulations as the non-scaled case (i.e., the RMDTE ratio between the scaled and non-scaled case would be very close to 1), due to the presence of a predictability bifurcation point described in Melhauser and Zhang (2012). This is also not seen in the case of Erin in Fig. 5.9. However, the increased RMDTE ratios over the NOCON subset in the Erin and PRE regions reveal that some spread growth is associated with approaching the intrinsic limit. The RMDTE ratio growth in the NOCON region is likely mostly due to errors associated with not being completely limited by practical predictability, since there is little to no chaotic moist convective dynamics (except at the end of the ensemble run), the main cause of intrinsic predictability limits, in this area. Advection of coherent RMDTE structures into the region could also increase the ratio, but this affect would be of a similar magnitude in both Erin_control and Erin_half. Further, it is not unreasonable to expect the ensemble characteristics that lead to practical predictability limits would be somewhat independent of the flow regime (i.e., region and atmospheric pattern), since, in this case, convection is explicitly allowed and all the members use the same model parameterizations. Thus, any region that has a faster increase in the RMDTE ratio (i.e., the scaled ensemble RMDTE over the control ensemble RMDTE) over a non-convective region (such as NOCON here in the case of Erin) has some level of influence from the intrinsic predictability limit, in addition to limits associated with practical predictability, on the ensemble spread. The influence of the intrinsic limit, to some extent, occurs in the Erin and PRE subsets of the Erin experiments, since the ratios grow at a faster rate than the NOCON region. This is not surprising given the amount of convective precipitation that occurs in these regions over the ensemble simulations. Therefore, in the case of Tropical Storm Erin, it appears that both practical and intrinsic predictability limits are influencing the resulting forecasts to some degree that may not be obvious looking at the entire domain RMDTE. It makes intuitive sense that the there would be a continuum between purely practical and intrinsic predictability limited cases where both predictability limits could be influencing the ensemble spread growth characteristics. The degree to which these limits affect a specific case is highly controlled by the scale of and how much chaotic deep convection is occurring within the ensemble domain and the specific NWP model architecture.

5.2. Texas MCV on 25 May 2013

Similar to the Tropical Storm Erin case, the vortex associated with the MCV that caused substantial flooding in central Texas was already present in the TX_control ensemble at initialization. There were significant differences in the ensemble member's precipitation forecasts in central Texas during the time of the observed extreme rainfall (Fig. 5.11). Most of the members in TX_control produce rainfall accumulations of similar magnitudes to those observed, but have large errors in the location of the heaviest rainfall (e.g., c.f. Fig. 5.11a,b,h to Fig. 5.11l). All of the forecasts have the local maximum of precipitation in central Texas too far to the north and/or west (e.g., Fig. 5.11a,f,j,k). Several of the members create two local precipitation maximums in central Texas directly north and south of one another (Fig. 5.11b,c,k). Outside of Texas, the runs of TX_control produced remarkably consistent precipitation forecasts in Nebraska and Iowa, despite the high variability in central Texas (Fig. 5.11). This region experienced a linear, bowing MCS develop that moved west to east across Nebraska and Iowa during the early morning hours on 25 May 2013. The stratiform remnants continued to move southeast and eventually dissipated in north Kentucky early on 26 May (not shown). The members of TX_control reproduced the precipitation for this Nebraska MCS well both spatially and in overall magnitude, but there were differences in the exact location of the precipitation shield (c.f. Fig. 5.11a-k to Fig. 5.11l). Similar to the Erin_control cases, the TX_control members provided a consistent representation of the mesoscale precipitation accumulations removed from the MCV but maintained significant spread in the rainfall associated with the vortex center.

The nature of the mid-level vorticity anomaly associated with the Texas MCV seems to be the main cause of variability in the ensemble forecast precipitation in central Texas. The model was generally initialized in almost all members with a very elongated north-south local vorticity maximum at 500 hPa (Fig. 5.12a-c), which is similar to the NARR at the time of model initialization (Fig. 5.12d). The initial representation of the vorticity structure in members of TX_control differ in finer scale details (Fig. 5.12a-c), but the initial differences do not intuitively correspond to the resulting precipitation forecasts. For instance, member two of TX_control has a weaker, less organized initial vorticity signature (Fig. 5.12a) when

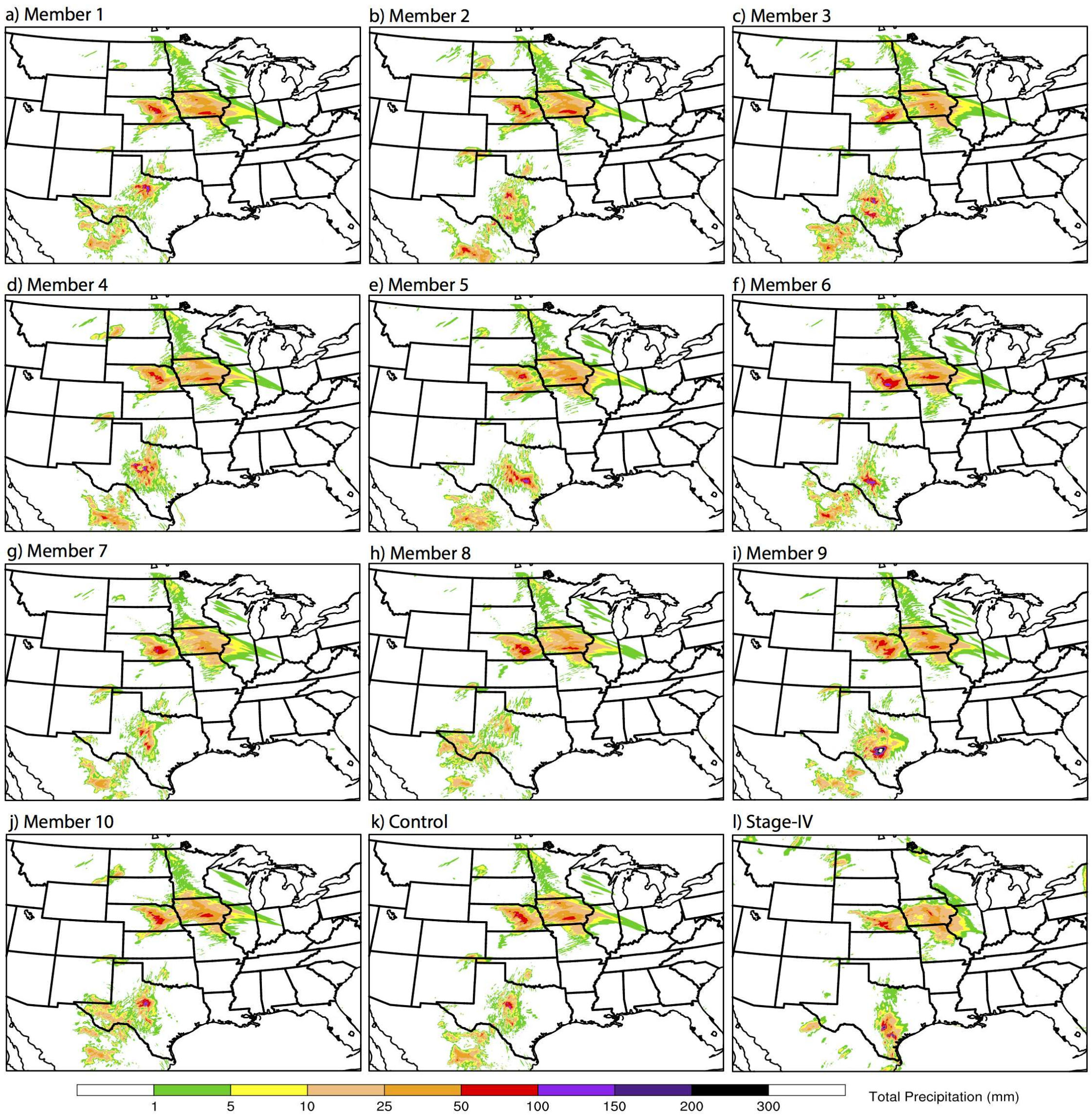

FIGURE 5.11. TX_control contoured accumulated precipitation valid for the 12-hr period ending 1800 UTC 25 May 2013 for each member of the ensemble, including the control. (a)-(j) correspond to members 1-10 of the ensemble, respectively. (k) corresponds to control member of the ensemble, and (l) is the Stage-IV gridded analysis valid over the same period.

compared to member eight at the same time (Fig. 5.12b). However, member eight goes on to produce less intense, scattered precipitation in north-central Texas (Fig. 5.11h), but member two produces a dipole of over 50 mm precipitation accumulations in central Texas (Fig. 5.11b). Model simulated radar reflectivity for members two and eight shows deeper

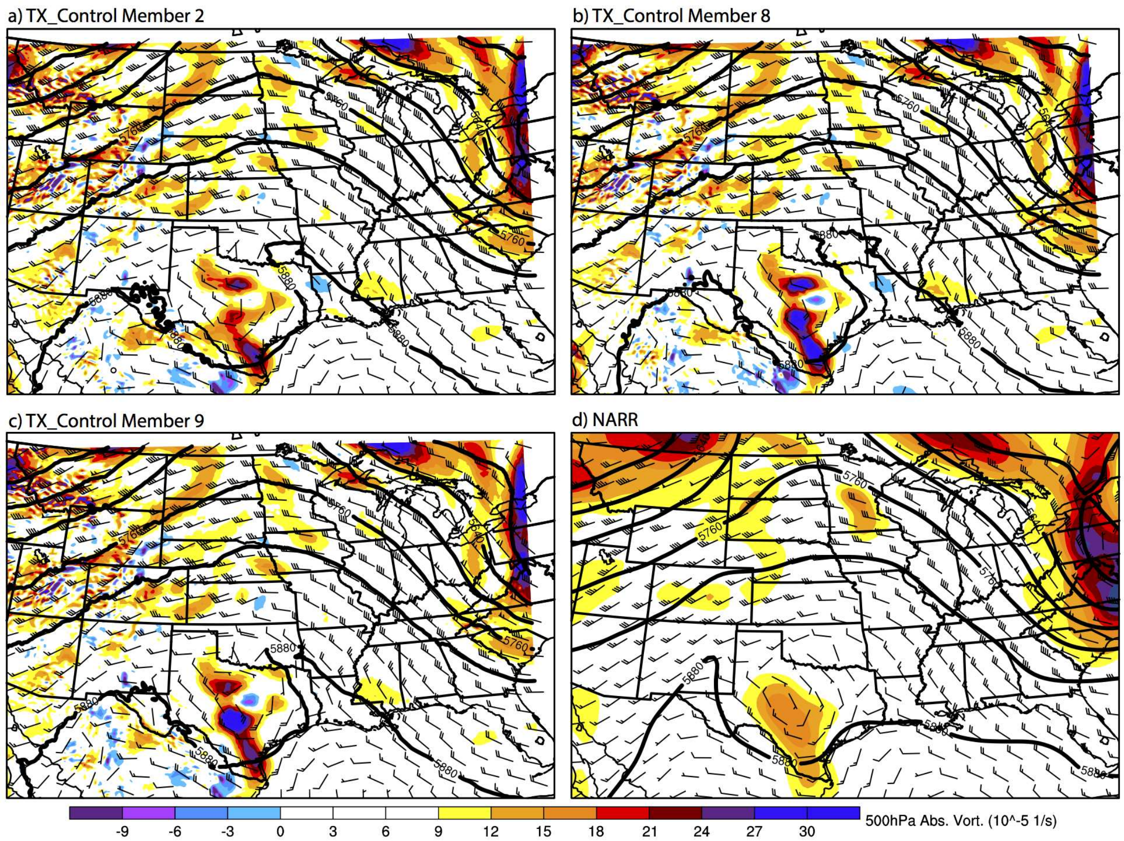

FIGURE 5.12. (a)-(c) Absolute vorticity at 500-hPa ($\times 10^{-5}\mathrm{s}^{-1}$), shaded every $3\times 10^{-5}\mathrm{s}^{-1}$ above $-9\times 10^{-5}\mathrm{s}^{-1}$), 500-hPa geopotential height (contoured every 60 m), and 500-hPa wind barbs(half barb = 5 kt, full barb = 10kt, pennant = 50 kt, 1 kt = 0.5144 ms^{-1}) valid 0000 UTC 25 May 2013 for members 2, 8, and 9 of TX_control, respectively. (d) same as (a)-(c) except valid 0000 UTC 25 May 2013 from the NARR.

convection developing by 0600 UTC 25 May 2013 in north-central Texas in member two (c.f. Fig. 5.13a,b). This convection then continues to exist throughout 1800 UTC in member two, but becomes disorganized and dissipates in member eight (c.f. Fig. 5.13c,d). This illustrates the importance of the presence and location, or lack thereof, of convective initiation along the elongated vorticity maximum in strengthening the MCV and determining the location of each members precipitation forecast. Thus, the forecast variability between members in TX_control is largely due to a combination between the unusual elongated vorticity signature and the low predictability of the initiation and evolution of deep moist convection.

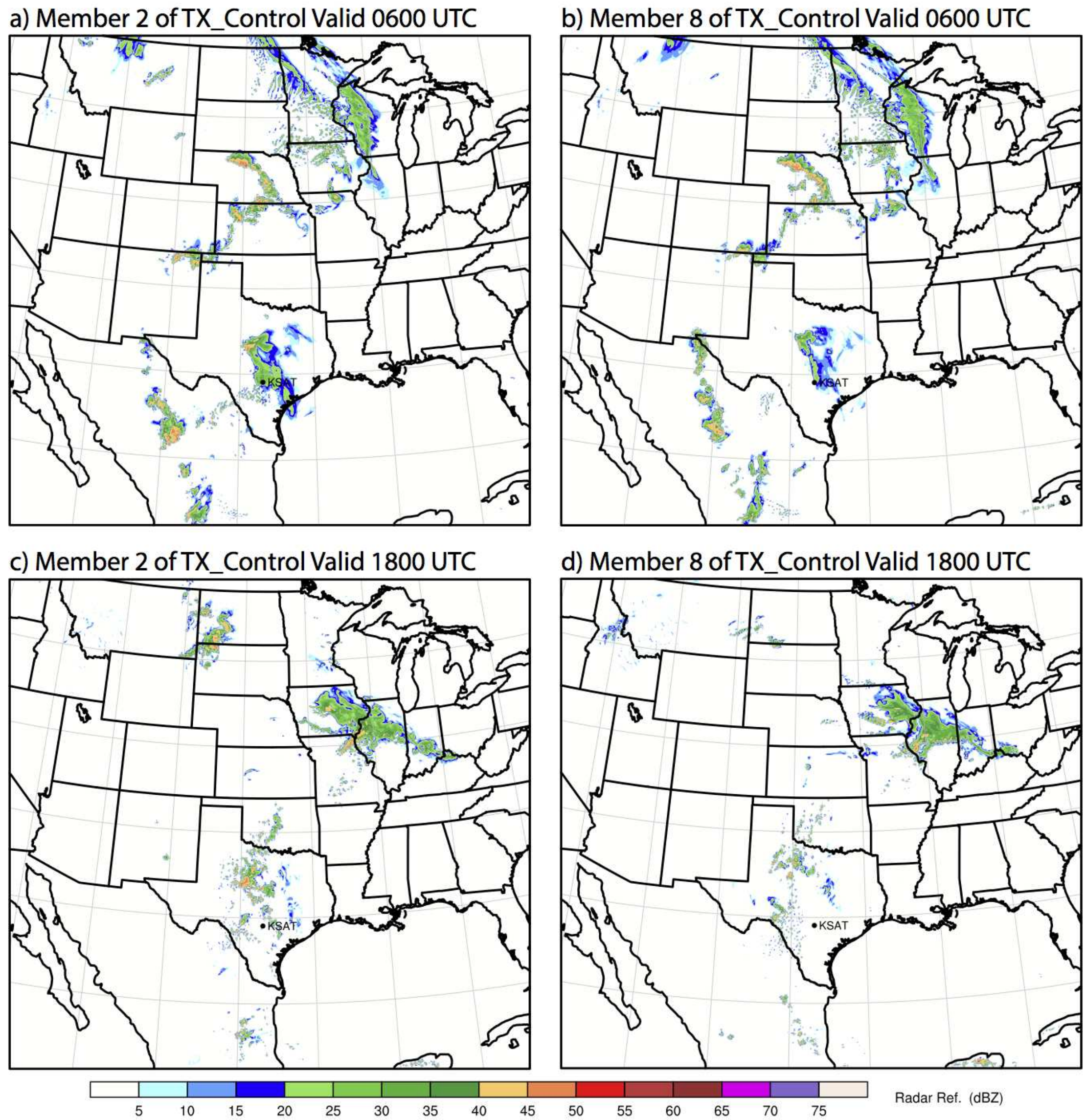

FIGURE 5.13. Simulated radar reflectivity from members 2 (a,c) and 8 (b,c) of TX_control valid at 0600 UTC (a,b) and 1800 UTC (c,d) 25 May 2013. KSAT denotes location of San Antonio International Airport.

The scaled ensemble runs for the Texas MCV case (TX_half and TX_third) produced continued consistency in the precipitation forecasts along the baroclinic zone in Nebraska and Iowa (Fig. 5.14c-f). In fact, almost no variability between ensemble runs in TX_half and, especially, TX_third are seen for this rainfall swath (c.f., Fig. 5.14e and Fig. 5.14f). However, there was little variation between the members for precipitation in Nebraska and Iowa in TX_control (Fig. 5.11), which may imply that this ensemble configuration is underdispersive

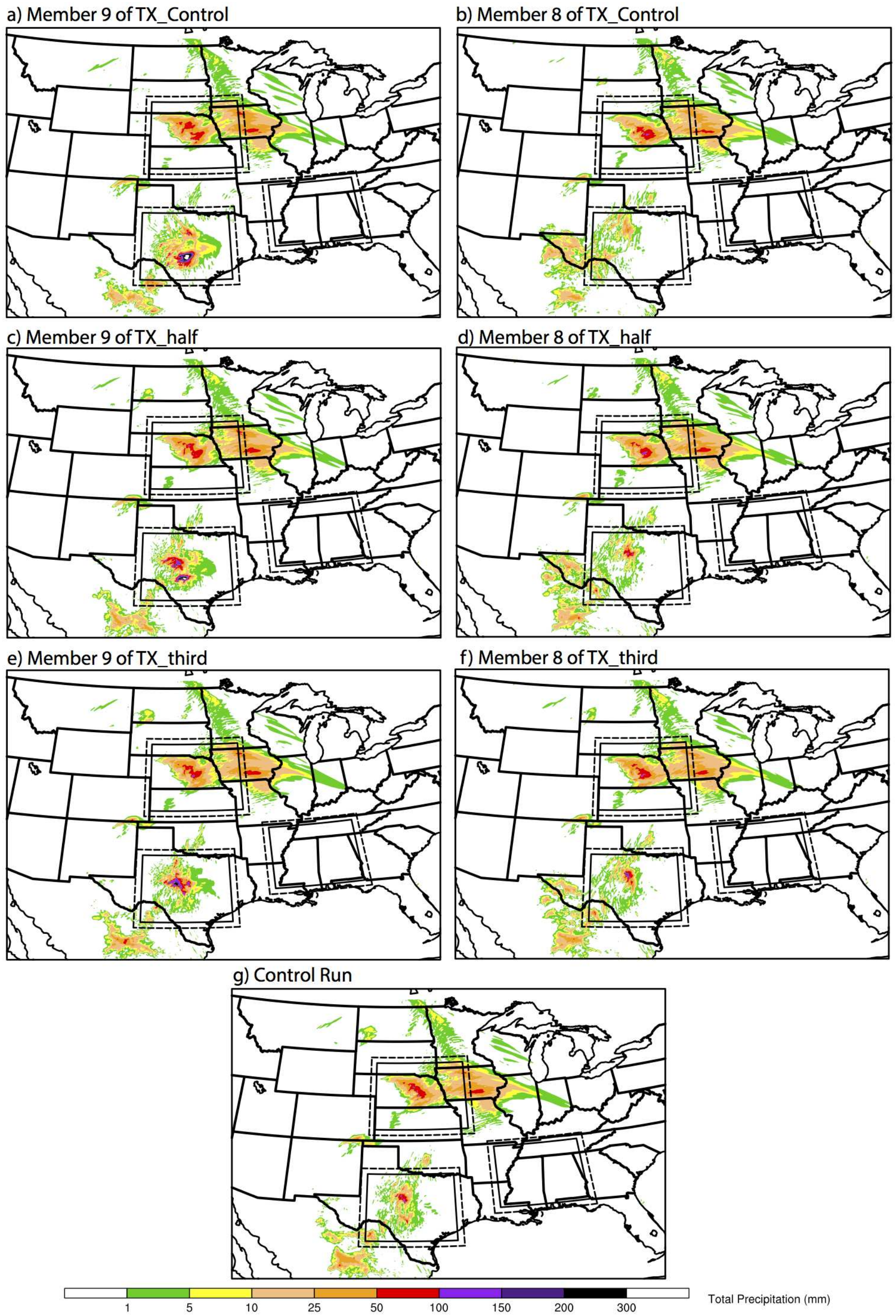

FIGURE 5.14. TX_control (first row), TX_half (second row), and TX_third (third row) contoured accumulated precipitation from members 8 (b,d,f) and 9 (a,c,e) valid for the 12-hr period ending 1800 UTC 25 May 2013. (g) depicts the accumulated precipitation for the control member of the ensemble over the same time period. Boxes indicate regions of equal area associated with the "MCV" vortex (centered in Texas), the baroclinic zones called "MCS" (centered on Nebraska), and a region devoid of convection called "NOCON" (centered along Alabama-Mississippi border) over which the AS metric (solid boxes) and regional RMDTE (dashed boxes) are calculated.

in this region and got "lucky" in creating a good forecast. Further, the precipitation region associated with the Texas MCV continues to converge as the perturbation off the control is reduced, but non-negligible differences still remain. For instance, member eight, which produced the least precipitation in the central Texas region in TX_control, increases the forecasted accumulation as the perturbation is reduced (c.f., Fig. 5.14b,d,f). Member nine, which produced the most representative precipitation compared to the observations, moves the forecast accumulations north and decreases the forecast accuracy (c.f., Fig. 5.14a,c,e). These two members, as the perturbation off the control is reduced, create precipitation forecasts that look more like the control member of the ensemble (Fig. 5.14g). Given that in the scaled experiments the ensemble is artificially being made underdispersive, reduction of the ensemble spread is expected behavior. This reduction in precipitation forecast spread is a depiction of the overall ensemble spread reduction shown in Fig. 5.15 from TX_control to TX_third and discussed below.

In the TX MCV cases, three ensemble simulations, in addition to TX_control were performed based upon Reforecast-2 IC and LBCs: TX_half, where the IC and LBC perturbation off the control for each member were halved; TX_third, same as previous but by one-third; TX_2km, where TX_control was replicated except at a 2 km grid spacing. The domain averaged RMDTE time series for all of these ensemble runs is presented in Fig. 5.15. Upon inspection, similar patterns between this case and the ensemble run for Tropical Storm Erin can be seen. A diurnal cycle of the ensemble spread growth, peaking during the convectively active hours, is again seen across all ensemble runs for the Texas MCV (colored solid lines Fig. 5.15) with the exception, similarly to Erin, of the non-downscaled native resolution Reforecast-2 ensemble (dashed orange line Fig. 5.15). A reduction in the ensemble spread growth is again seen following the convectively active hours, which in this case is maximized

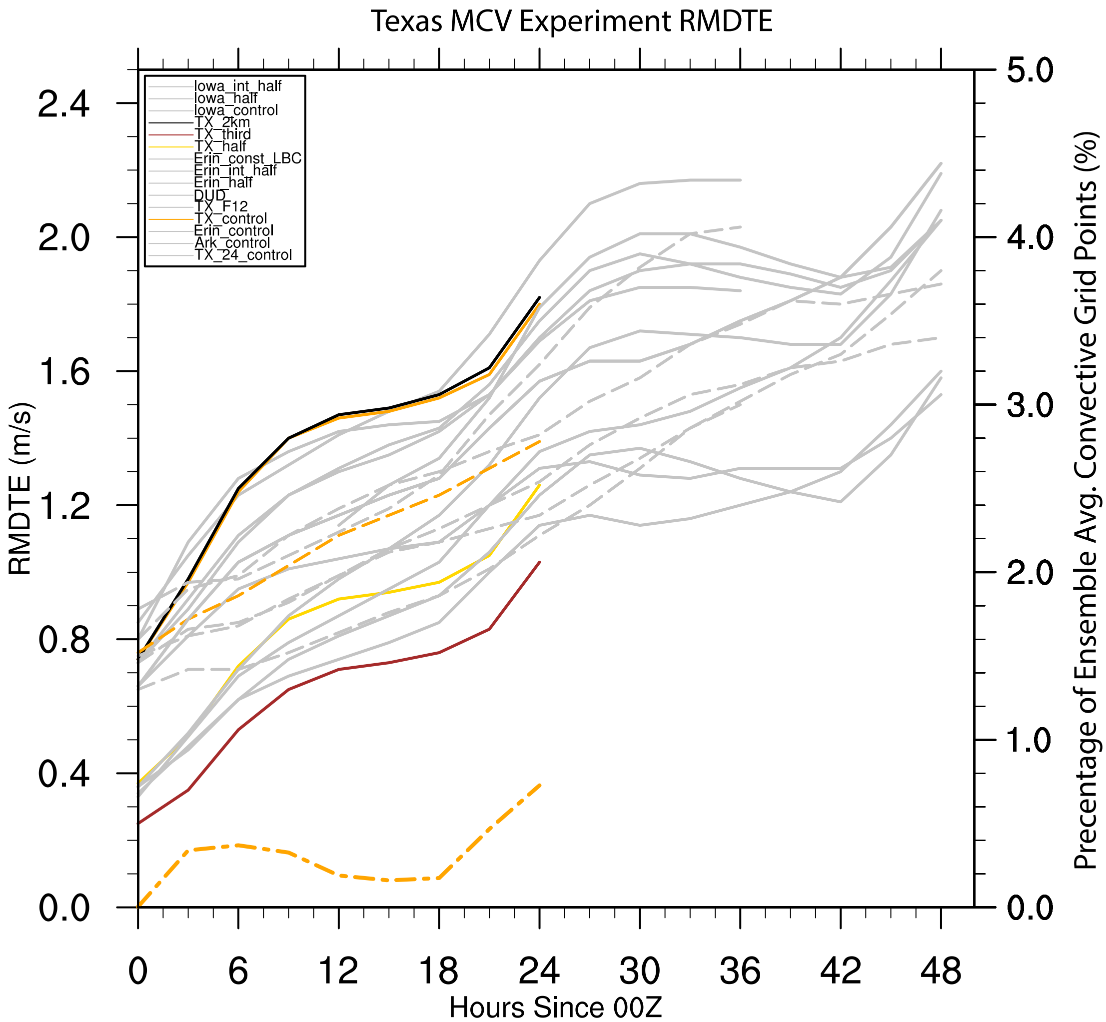

FIGURE 5.15. Time series of the domain averaged RMDTE highlighting the ensemble simulations for the Texas MCV case. Colored lines correspond to TX_control (orange), TX_half (yellow), TX_third (brown), TX_2km (black), and RMDTE from native Reforecast-2 resolution (dashed orange). Grey lines represent the RMDTE time series for all of the other ensemble simulations in this study for comparison. Dot-dashed orange line at bottom of graph corresponds to percentage of ensemble average grid points that exceed 1 m/s of vertical velocity (w) at 700 hPa (right vertical axis) in TX_control to denote convectively active times.

in the nocturnal period of 25 May 2013 (∼first 6 to 12-hr of Fig. 5.15 solid colored lines). This speaks to the viability of using convection-allowing ensembles for prediction beyond the first convective cycle, since the upscale error growth associated with moist convection does not cause rapid divergence of the individual ensemble solutions. The downscaled ensemble runs show a similar RMDTE growth rate compared to the native Reforecast-2 outside of the model spin up time and increased growth rates during convectively active hours (c.f. orange and dashed orange lines), which, similar to Erin, shows the importance of the large-scale atmospheric features on constraining the evolution of the ensemble members.

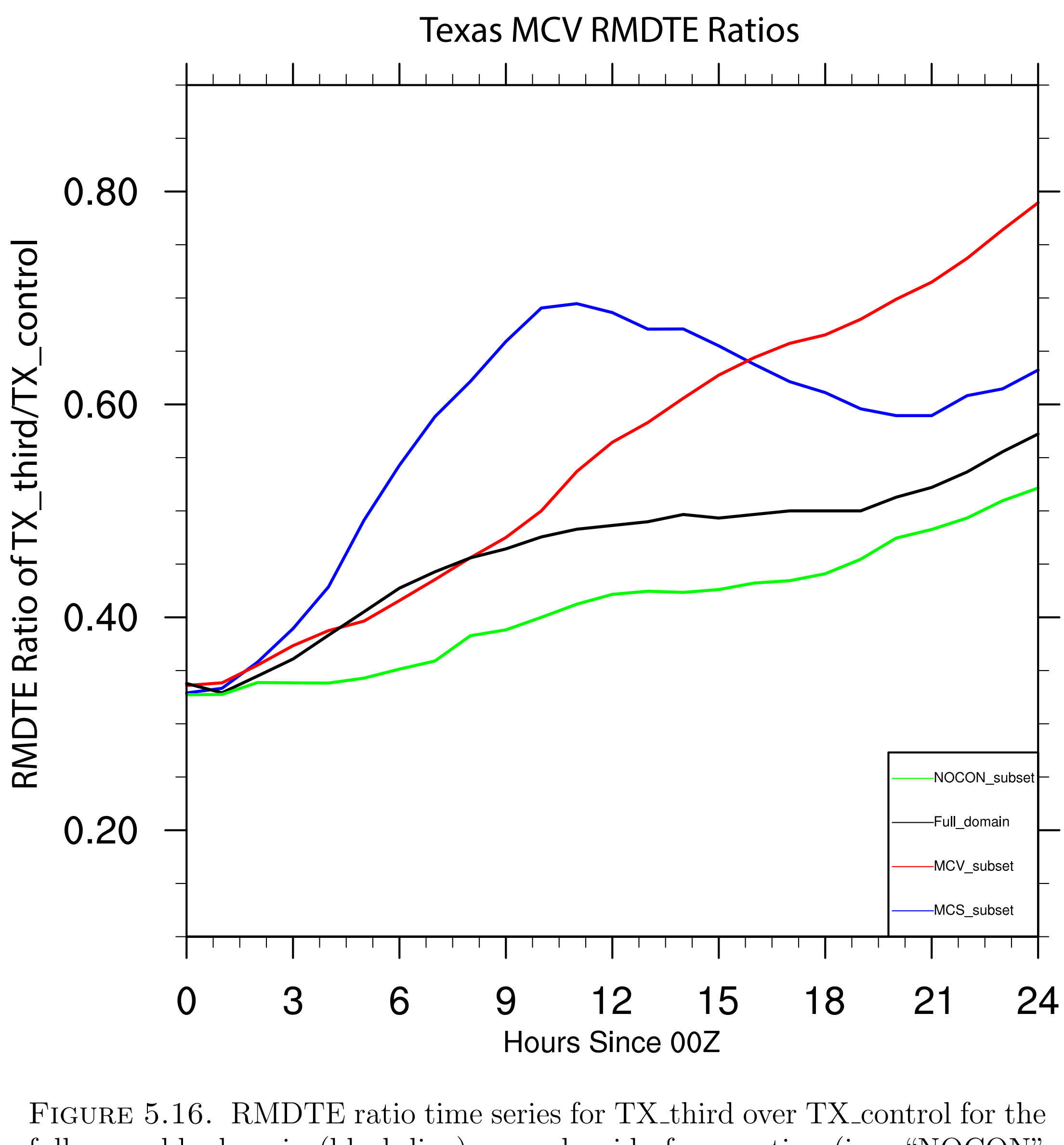

FIGURE 5.16. RMDTE ratio time series for TX_third over TX_control for the full ensemble domain (black line), area devoid of convection (i.e., "NOCON" region in green), region bounding the Texas MCV vortex (i.e., "MCV" region in red), and the associated baroclinic zone (i.e., "MCS" region in blue) defined in Fig. 5.14.

A linear decrease in the initial RMDTE corresponding, roughly, to the perturbation scaling is seen when TX_control (orange line) is compared to TX_half (yellow line) and TX_third (brown line) (Fig. 5.15). However, specifically focusing on TX_third and TX_control, this linear scaling is not maintained throughout the ensemble simulations with the ratio of RMDTE between TX_third and TX_control increasing through time (black line in Fig. 5.16), which illustrates the non-linearity of the spread growth in this case over the entire domain. The significant decrease in the overall RMDTE form TX_control to TX_third shows the importance that the large-scale atmospheric forcing has on the magnitude of the ensemble spread (Fig. 5.15). However, similar to Erin, the steadily increasing RMDTE ratio between TX_third and TX_control shows that the upscale spread growth associated with small scale motions is still present, but second order to the influences of large-scale atmospheric motions. Additionally, increasing the grid-spacing of the ensemble ftom 4 km to 2 km in the TX_2km case, did not increase the overall ensemble spread significantly by the end of the simulation (c.f., black and orange lines in Fig. 5.15). This indicates that the additional small scale motions resolved by doubling the grid-spacing did not, in this case, lead to a substantial increase in the spread of the ensemble. However, the model grid-spacing is still only on the kilometer scale. It would not be surprising to see this result not hold for model grid-resolutions on the sub-kilometer scale, which was not tested due to computation and storage constraints. Even though the ensemble simulations run for the Texas MCV case only go out to 24-hr from initialization, the ensemble spread evolution characteristics seen over the entire model domain are similar to those from Tropical Storm Erin.

The three different subsetted regions chosen, outlined by the dashed boxes in Fig. 5.14, for the Texas MCV include a region centered on the MCV (known as the "MCV subset" for the rest of this section), the area of rainfall associated with the northern baroclinic zone

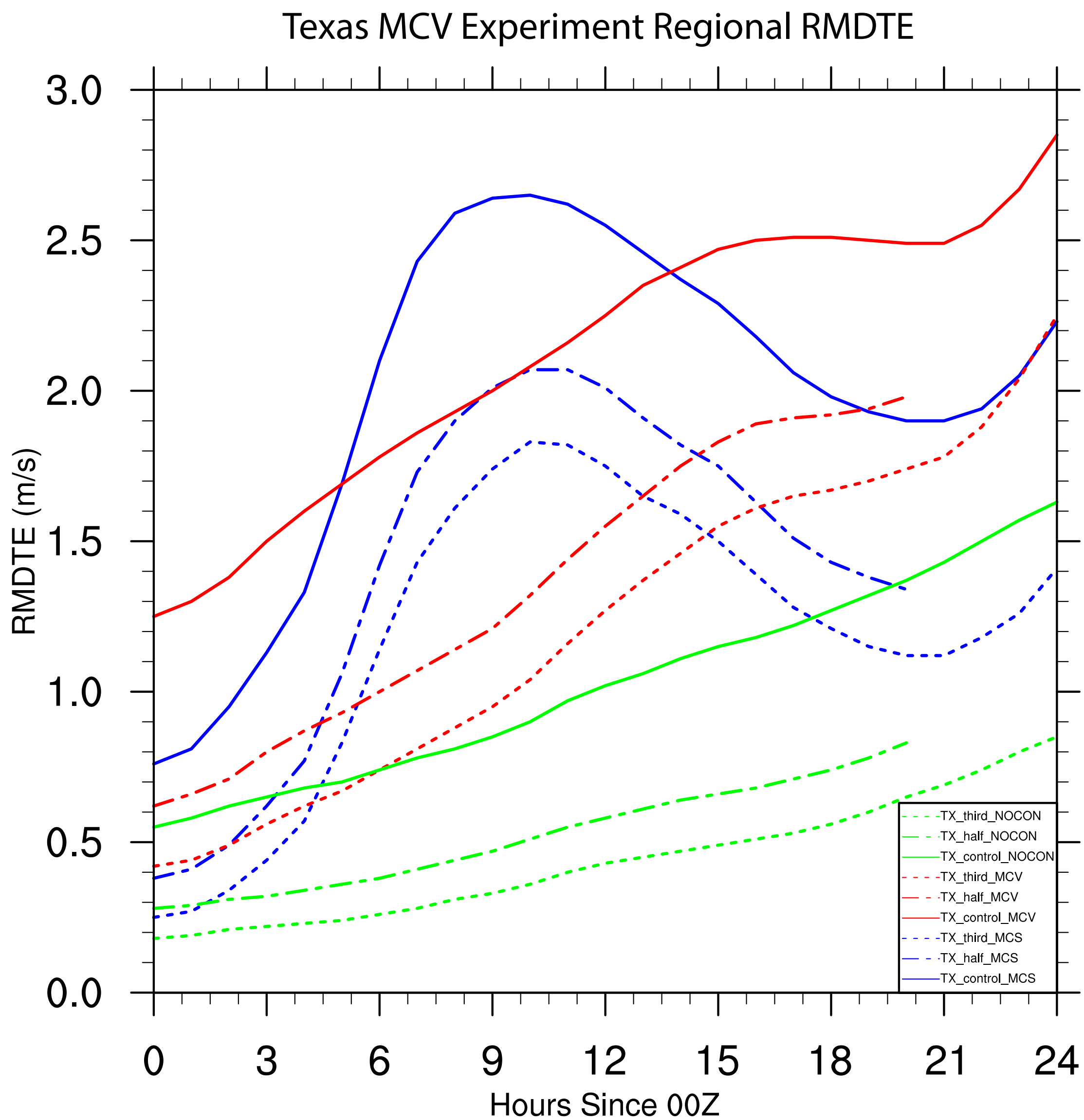

FIGURE 5.17. RMDTE time series for TX_control (solid lines), TX_half (dot-dashed lines), and TX_third (dotted lines) for NOCON regional subset (green), MCV subset (red), and MCS subset (blue) as defined by dashed boxed regions centered in Mississippi-Alabama border, Texas, and Nebraska, respectively, in Fig. 5.14.

("MCS" subset), and a region with little to no convection ("NOCON" subset). Overall, the decrease in the overall RMDTE from TX_control to TX_half and TX_third further show, similarly to Erin, that the large-scale atmospheric forcing is the main constraint on the overall magnitude of the ensemble spread in these three regions (Fig. 5.17). The MCV subset initializes with the highest RMDTE (red lines in Fig. 5.17) and the NOCON region, the lowest RMDTE (green lines in Fig. 5.17), likely due to the significant differences in the nature of the linear vorticity structure, discussed earlier in this section, near the MCV, and the lack of moist convection in the NOCON region, respectively. Very little diurnal cycle is seen in the MCV region over TX_control, TX_half, and TX_third, especially when compared to the same simulations in the MCS region (c.f., blue and red lines Fig. 5.17). A MCV is a very good example of how both the convective and large-scale forcing can interact to produce varying solutions within an ensemble. For instance, the strength, presence, and evolution of an MCV is tied to the initiation, strength, and maintenance of convection through vertical heating profiles, and the MCV motion is largely determined by the large-scale atmospheric flow field. Thus, similarly to the region near Erin's central vortex, the lack of diurnal cycle in the MCV subset is associated with increased energy interactions between the convective and synoptic scales, which in both of the cases has been associated with multi-day convective rainfall. The large diurnal cycle (blue lines in Fig. 5.17) present in the ensemble simulation in the MCS region illustrates the importance of synoptic scale constraint on the ensemble evolution. A significant amount of convection occurs in this region, which leads to a very large RMDTE growth rate and peak magnitude (blue lines in Fig. 5.17). However, despite this large increase, the ensemble spread is reduced by over 20% within ten hours in this region in TX_control. The surface baroclinic zone that is responsible for the MCS development and resulting precipitation accumulation is equally responsible for reduction of RMDTE following the first convective cycle (blue lines in Fig. 5.17). The AS metric for these two regions follows a somewhat contradictory pattern to the RMDTE, unlike what was seen in the Erin case. The largest AS was seen by the MCV case, yet the RMDTE during the time of most intense precipitation for the MCS region is larger (c.f., Table 5.2 and Fig. 5.17). This implies that the RMDTE, which here quantifies the regional spread from an energy perspective, in some cases, may not have a direct relationship to the spread seen in the precipitation forecasts.

TABLE 5.2. Area spread (AS) metric for regions in ensemble experiments for the Texas MCV case above 25.0 mm and 50.0 mm precipitation accumulation thresholds. Accumulation period corresponds to windows of most intense rainfall previously identified in Fig. 3.2, and regions correspond to those identified and encompassed by solid boxes in Fig. 5.14.

Case	Region	25.0 mm	50.0 mm
TX_control	MCV	5.5	7.5
–	MCS	2.4	3.8

Similarly to the Tropical Storm Erin case, the ratios between the TX_third and TX_control can be used to look further into the predictability of specific regions in the Texas MCV case. As discussed in the Erin case, a specific region can be at the theoretical limit of practical predictability, the limit of intrinsic predictability, or be limited by a combination of both. The ratios for the three subsetted regions for the Texas MCV case are presented in Fig. 5.16. Similar to the full domain RMDTE ratios, there is a increase of the ratio across all of the subsetted regions through time, which implies that in these cases the TX_third ensemble RMDTE is growing faster than TX_control. The non-linearity seen in these regional RMDTE ratios, along with the full domain ratio, implies that this case is not at the theoretical limit of practical predictability, similar to the Erin case. Further, the lack of immediate convergence of RMDTE ratio to one between TX_third and TX_control illustrates, as discussed in more detail in the Erin case, that these cases are also not purely limited by intrinsic predictability. The steady increase of the RMDTE ratio associated with the NOCON region (green line in Fig. 5.16) is likely due to not being at the theoretical limit of practical predictability, since no moist convection occurs within this subsetted region over the simulation. If the faster

RMDTE growth in the NOCON region is treated as a generalizable baseline (i.e., independent or region and flow regime) of spread increase due only to practical predictability limits, both the MCV and MCS regions are influenced by aspects of both intrinsic and practical predictability, since the RMDTE ratios grow faster than the NOCON region (i.e., red and blue lines in Fig. 5.16). The rapid increase in the MCS RMDTE ratio (blue line in Fig. 5.16) illustrates the importance of moist convection in creating the spread growth associated with intrinsic predictability limits. The increase in the RMDTE ratio corresponds to the time of maximum rainfall seen in the MCS region, which implies that the convection occurring in TX_third is leading to the faster spread growth compared to the same region in TX_control. However, the reduction of the RMDTE ratio following this time shows that this region is not at the pure intrinsic predictability limit because the spread growth rate in TX_third is reduced (i.e., RMDTE ratio decreases), following the convectively active periods due to the constraints of the large-scale atmospheric flow. Additionally, the MCV subset maintains a constantly increasing RMDTE ratio (red line in Fig. 5.16) throughout the ensemble simulation that exceeds the NOCON region. This shows that aspects of flow in this region are affected by spread growth associated with both intrinsic and practical predictability limits, throughout the simulation. However, since the RMDTE ratio does not rapidly converge to one, the MCV subset is not at the limit of intrinsic predictability. More specifically, the constant increase in the RMDTE ratio implies that TX_third continually has a faster spread growth rate then TX_control, which is likely due to the continuing feedback between the convective and large scales often seen with MCVs (see above). The exact degree to which intrinsic predictability spread growth influences the RMDTE evolution of the MCV and MCS regions, in addition to the growth associated with practical predictability limits, is difficult to discern. However, it is highly dependent on the amount of convection present, and how much that convection can effect the future state of large-scale atmospheric features. Thus, similarly to the Tropical Storm Erin case, the spread evolution of ensemble simulations in Texas MCV case appear to be affected by a combination of intrinsic and practically predictability limits with varying influence on a regional scale.

5.3. Iowa MCS on 25 June 2015

Unlike the previous two cases discussed in this section, the Iowa MCS case was not caused by a mesoscale vortex that was preexisting in the model initial conditions. The Iowa MCS, as mentioned in the case description, was a fast moving, elevated, nocturnal, and convective cold pool driven event. The precipitation forecasts from the members of the Iowa_control ensemble all produced consistent forecasts with a signal for heavy rain in the central to upper Mississippi Valley (Fig. 5.18). Almost all of the Iowa_control members (except members 3 and 9) produced a 50 mm precipitation accumulation in a northwest to southeast line from east-central Iowa into northern Illinois (Fig. 5.18). Further, some members clearly split the MCS into a northern and southern storm over the period (Fig. 5.18b,f,g,i,j,). The observed MCS formed further west and south then the members suggested (c.f. Fig. 5.18a-k to Fig. 5.18l), but the eastward extent of the MCS propagation and the associated precipitation accumulations were well represented in the Iowa_control runs. There was similar spatial variability, compared to the MCS in Iowa and Illinois, between the ensemble runs for the precipitation that was predicted to fall in and around the Gulf coast of Florida (Fig. 5.18a-k). All members (Fig. 5.18a-k) predicted a substantially larger spatial inland extent of the precipitation in the area compared to the Stage-IV analysis (Fig. 5.18l). However, since the Stage-IV analysis can only detect rainfall over or within radar range of land, the system could still have occurred, but further offshore.

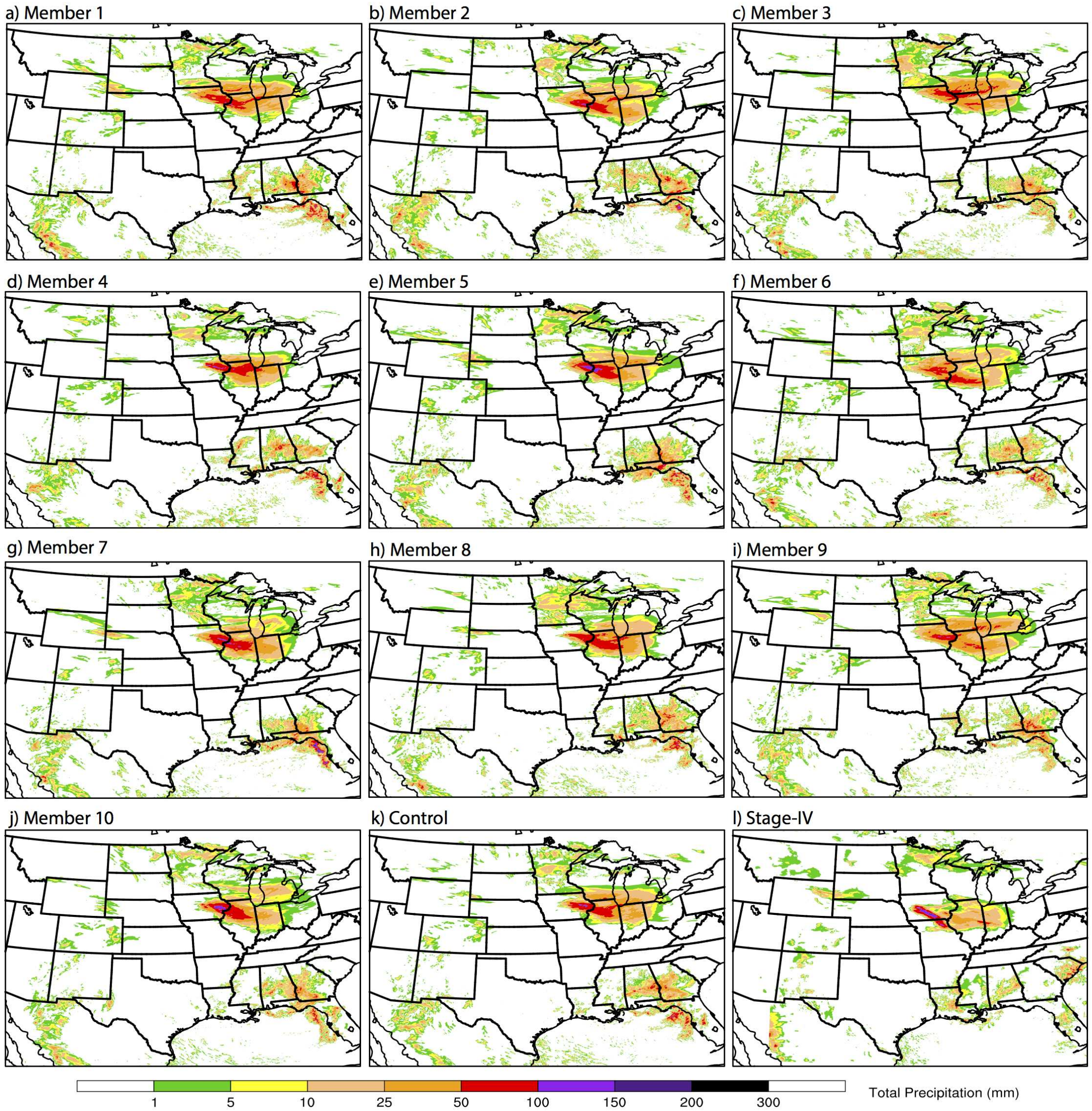

FIGURE 5.18. Iowa_control contoured accumulated precipitation valid for the 12-hr period ending 1200 UTC 25 June 2015 for each member of the ensemble, including the control. (a)-(j) correspond to members 1-10 of the ensemble, respectively. (k) corresponds to control member of the ensemble, and (l) is the Stage-IV gridded analysis valid over the same period.

Upon examination of the forecasts from Iowa_IC_half and Iowa_half, very little difference in the magnitude and spatial extent of the forecasted precipitation in Iowa and Illinois from each ensemble member was seen compared to the Iowa_control run (e.g. for two members, Fig. 5.19). Given the lack of variability between the members in Iowa_control, it is not

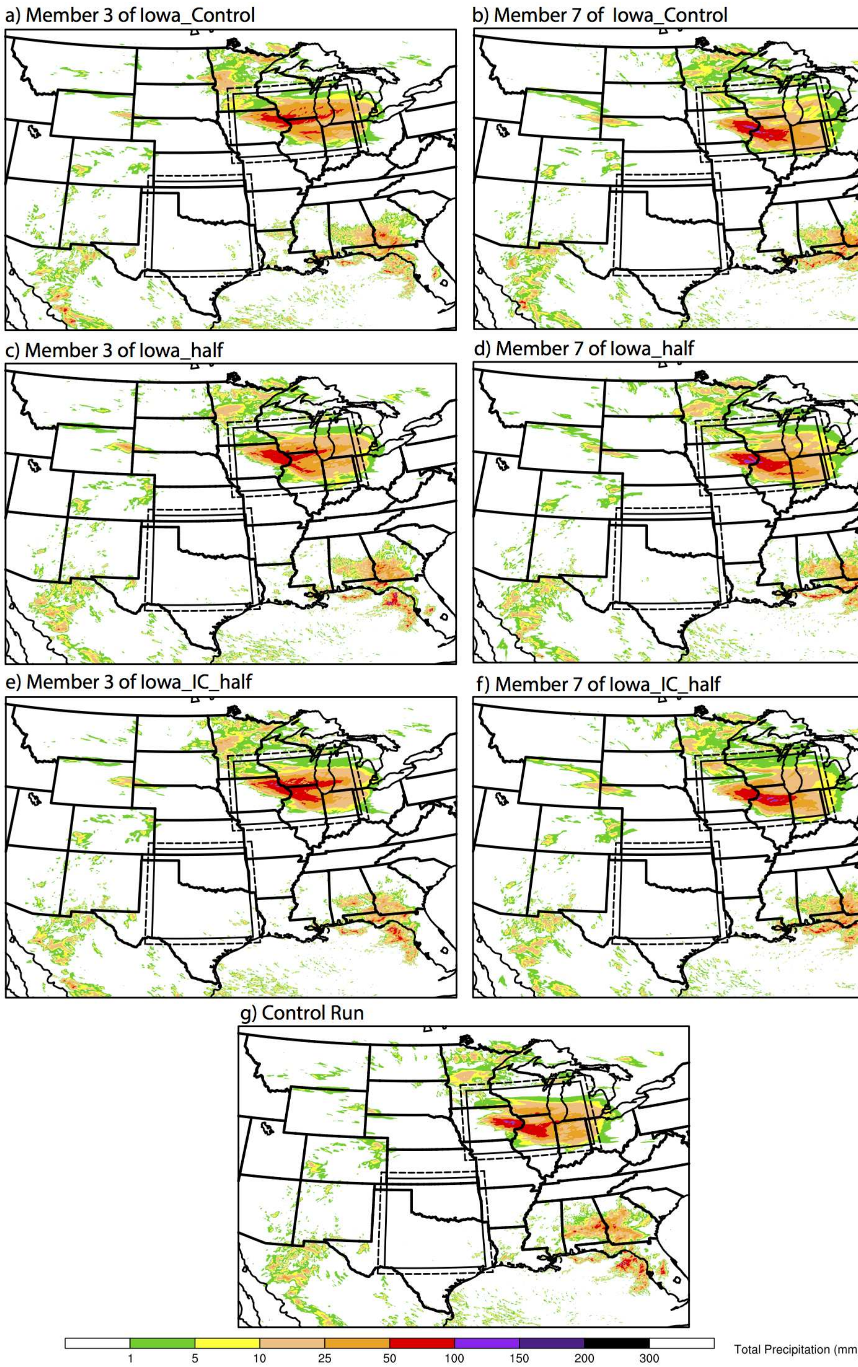

FIGURE 5.19. Iowa_control (first row), Iowa_half (second row), and Iowa_IC_half (third row) contoured accumulated precipitation from members 3 (a,c,e) and 7 (b,d,f) valid for the 12-hr period ending 1200 UTC 25 June 2015. (g) depicts the accumulated precipitation for the control member of the ensemble over the same time period. Boxes indicate regions of equal area associated with the fast moving MCS called "MCS" (centered on Texas) and a region devoid of convection called "NOCON" (centered along Wisconsin-Illinois border) over which the AS metric (solid boxes) and regional RMDTE (dashed boxes) are calculated.

surprising that artificially shrinking the spread of the ICs and LBCs in Iowa_half and just the ICs in Iowa_IC_half does not change the resulting precipitation forecasts for each member. In the Iowa case, however, there does not seem to be as strong convergence of the precipitation forecasts in from Iowa_control to Iowa_half compared to the control run as was seen between TX_control and TX_half and the control run of the Texas MCV case (c.f., Fig. 5.19a,c to Fig. 5.19g with Fig. 5.14a,c to Fig. 5.14g).

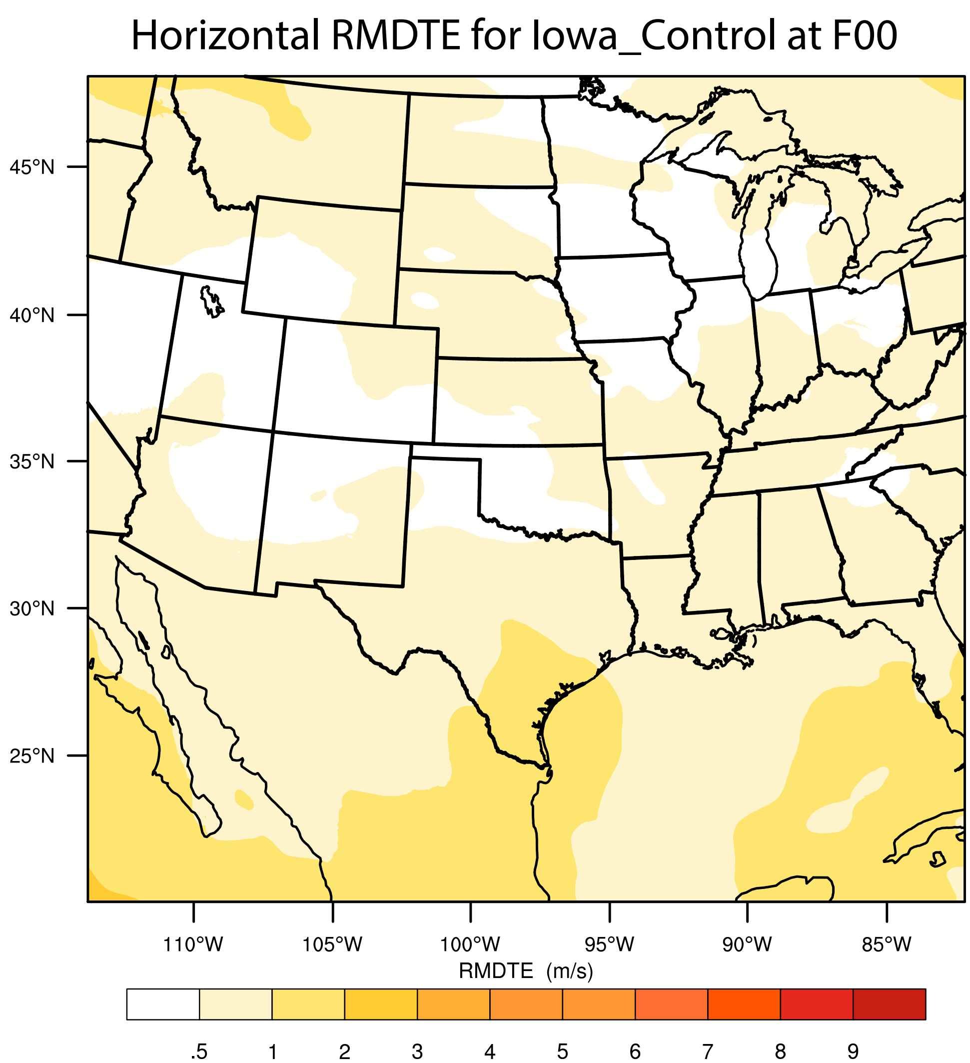

FIGURE 5.20. Horizontal RMDTE defined by Eqn. 4 for Iowa_control valid at 0000 UTC 24 June 2015 (ensemble initialization).

Similarly to the precipitation forecasts of the PRE associated with Erin and the rainfall in Nebraska to Iowa in the Texas MCV cases that did not vary significantly with the scaled ensemble experiments, the Iowa MCS was associated with a surface baroclinic zone. However in the Iowa MCS, unlike the precipitation forecasts that were quite accurate along the baroclinic zone in the Texas MCV and Erin case, the precipitation forecasts were not as accurate in capturing the evolution of the bowing MCS (Fig. 5.18). The initial RMDTE for Iowa_control in this area was lower than the surroundings (Fig. 5.20), which implies high certainty in the ensemble analysis in this region. However, the member forecasts evolved in a way that did not encompass a solution that was similar to reality. This implies that for the Iowa MCS case, this ensemble configuration was underdispersive, since an evolution similar to reality was not contained in the realm of model solutions. One possible cause for this would be the parent Reforecast-2 ensemble being over confident in the location of the baroclinic zone when the individual ensemble members were created, which would shrink the ensemble perturbations off the control in this area and not account for all of the model error appropriately. This behavior could also be caused by the use of a single physics ensemble in these simulations, which tended to produce the same type of MCS despite the varying IC perturbations. Since this underdispersive behavior is seen in MCS formation along baroclinic zones in the Erin and Texas MCV cases using the same model configuration, either cause is plausible. While not done in this study, more simulations will be performed to investigate these issues.

For the Iowa MCS case, two ensemble simulations in addition to the Iowa_control were executed: Iowa_half where the IC and LBC perturbation off the control for each member were halved and Iowa_IC_half where only the IC perturbation off the control of each member was halved. The temporal evolution of the ensemble spread for each simulation, similar to the

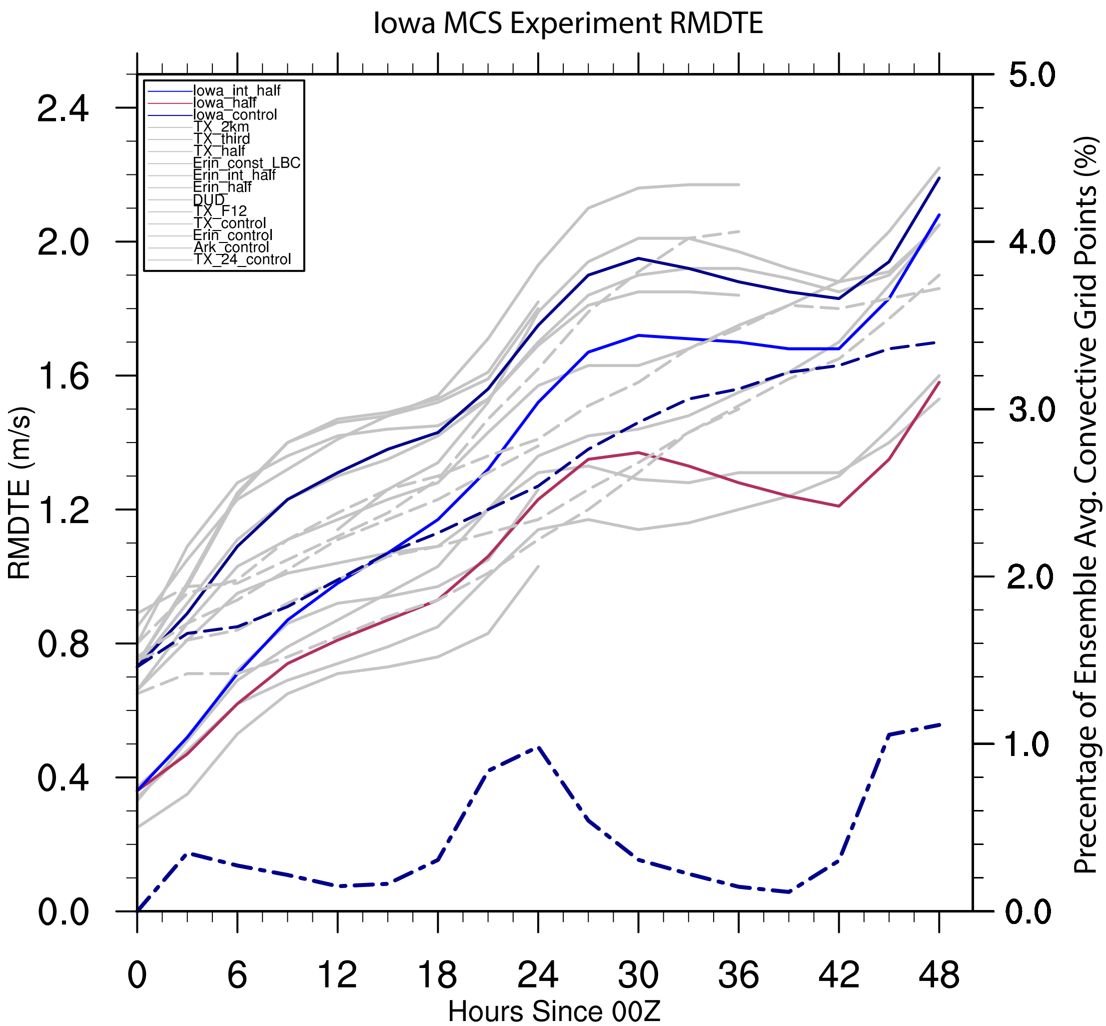

FIGURE 5.21. Time series of the domain averaged RMDTE highlighting the ensemble simulations for the Iowa MCS case. Colored lines correspond to Iowa_control (dark blue), Iowa_half (maroon), Iowa_IC_half (blue), and RMDTE from native Reforecast-2 resolution (dashed blue). Grey lines represent the RMDTE time series for all of the other ensemble simulations in this study for comparison. Dot-dashed blue line at bottom of graph corresponds to percentage of ensemble average grid points that exceed 1 m/s of vertical velocity (w) at 700 hPa (right vertical axis) in Iowa_control to denote convectively active times.

Erin and Texas MCV case, is shown in Fig. 5.21. Once again, a diurnal cycle in the ensemble spread is shown in all downscaled ensemble simulations for the Iowa MCS case (solid colored lines in Fig. 5.21). The peak growth rate is found during the convectively active times and dampens afterwards; however, as with the other cases, this pattern is not as discernible in the native Reforecast-2 ensemble (dashed blue line in Fig. 5.21). Furthermore, a similar growth rate is again observed between the Iowa_control (dark blue line) and native Reforecast-2 ensemble (dashed dark blue line) outside of the periods of convective activity and the model spin up during the first 6-hr of the simulations (Fig. 5.21). This, combined with the presence of a diurnal cycle in spread over the full domain, speaks to the viability of using convection-allowing ensembles beyond the first convective cycle, since no rapid divergence of the ensemble spread is seen after convectively active times, and the RMDTE growth rates associated with large-scale atmospheric features are maintained despite downscaling to the convection allowing scale. Additionally, the lower ensemble spread at 48-hr between Iowa_control and Iowa_IC_half (blue line) implies that the choice of ICs still has effects on the ensemble spread out to the end of the simulation (Fig. 5.21), which was also shown in the Erin and Texas MCV cases. Thus, the ensemble spread characteristics associated with the Iowa MCS are very similar to those of the Erin case, despite not being forced by a preexisting mesoscale vortex.

A scaling of the ensemble RMDTE ratio proportional to the perturbation scaling off the control is seen between Iowa_half and Iowa_control (black line in Fig. 5.22) at ensemble initialization in this case over the entire simulation domain, similar to Erin and the Texas MCV cases. However, a steady increase in the RMDTE ratio is seen through the ensemble simulation. This implies that the RMDTE is growing faster in Iowa_half compared to Iowa_control, which illustrates the lack of linearity in the ensemble spread growth between these two simulations over the entire domain. The decrease seen in the overall RMDTE between Iowa_half and Iowa_control (Fig. 5.21), again, shows the overall importance of the large-scale atmospheric features on the evolution and magnitude of the ensemble spread. Similar to the Erin and Texas MCV cases, the increasing RMDTE ratio through time shows

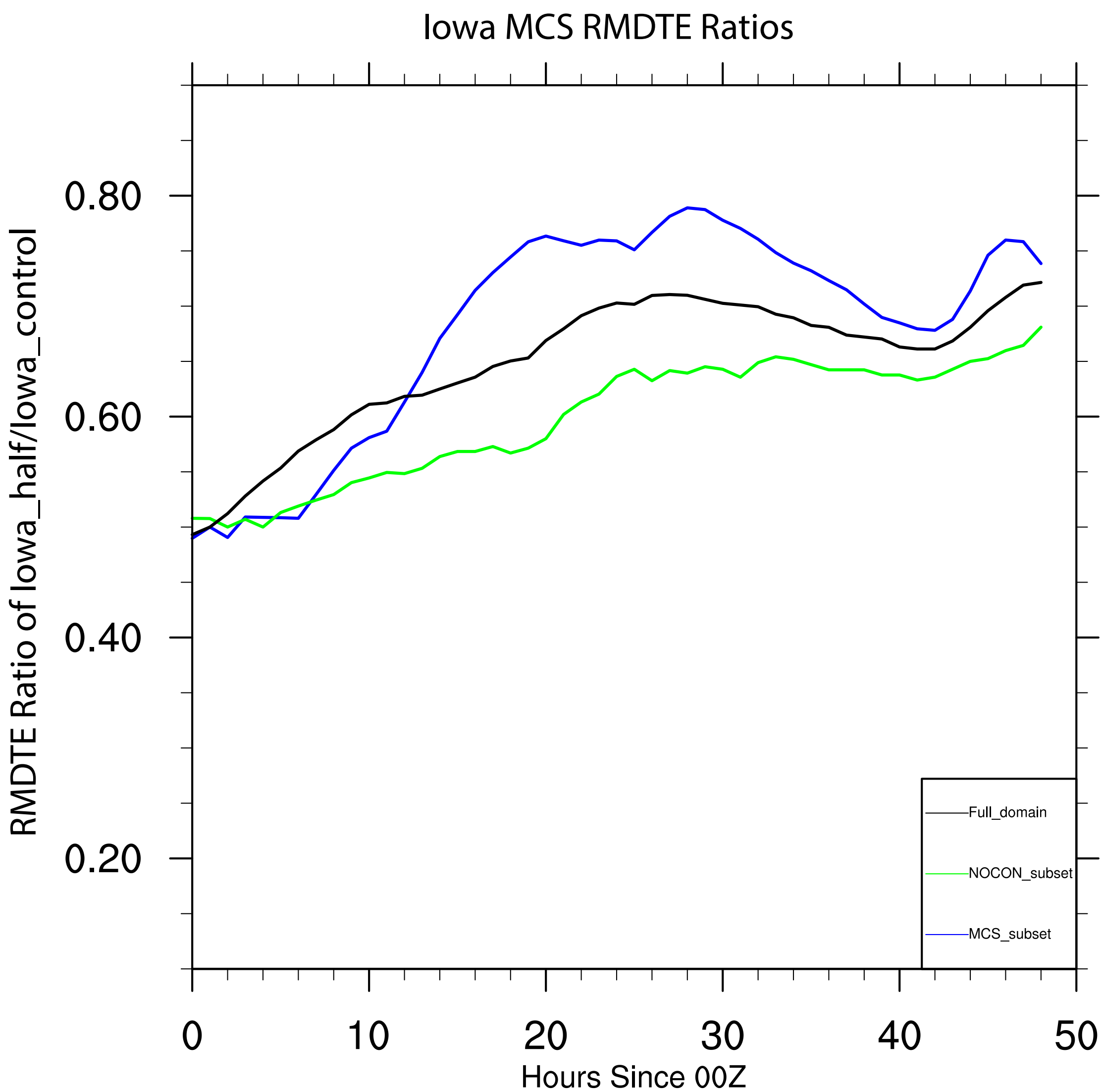

Figure 5.22. RMDTE ratio time series for Iowa_half over Iowa_control for the full ensemble domain (black line), area devoid of convection (i.e., "NOCON" region in green), and the region associated with the fast moving MCS (i.e., "MCS" region in blue) defined in Fig. 5.19.

that upscale spread growth associated with convective motions is still present, but has a largely second order impact on the ensemble spread compared to the large scale atmospheric features. These characteristics have been seen in all three of the cases investigated in this study.

The two regions subsetted out of the ensemble simulations for the Iowa MCS case, outlined by the dashed boxes in Fig. 5.19, include a region centered on the fast moving MCS

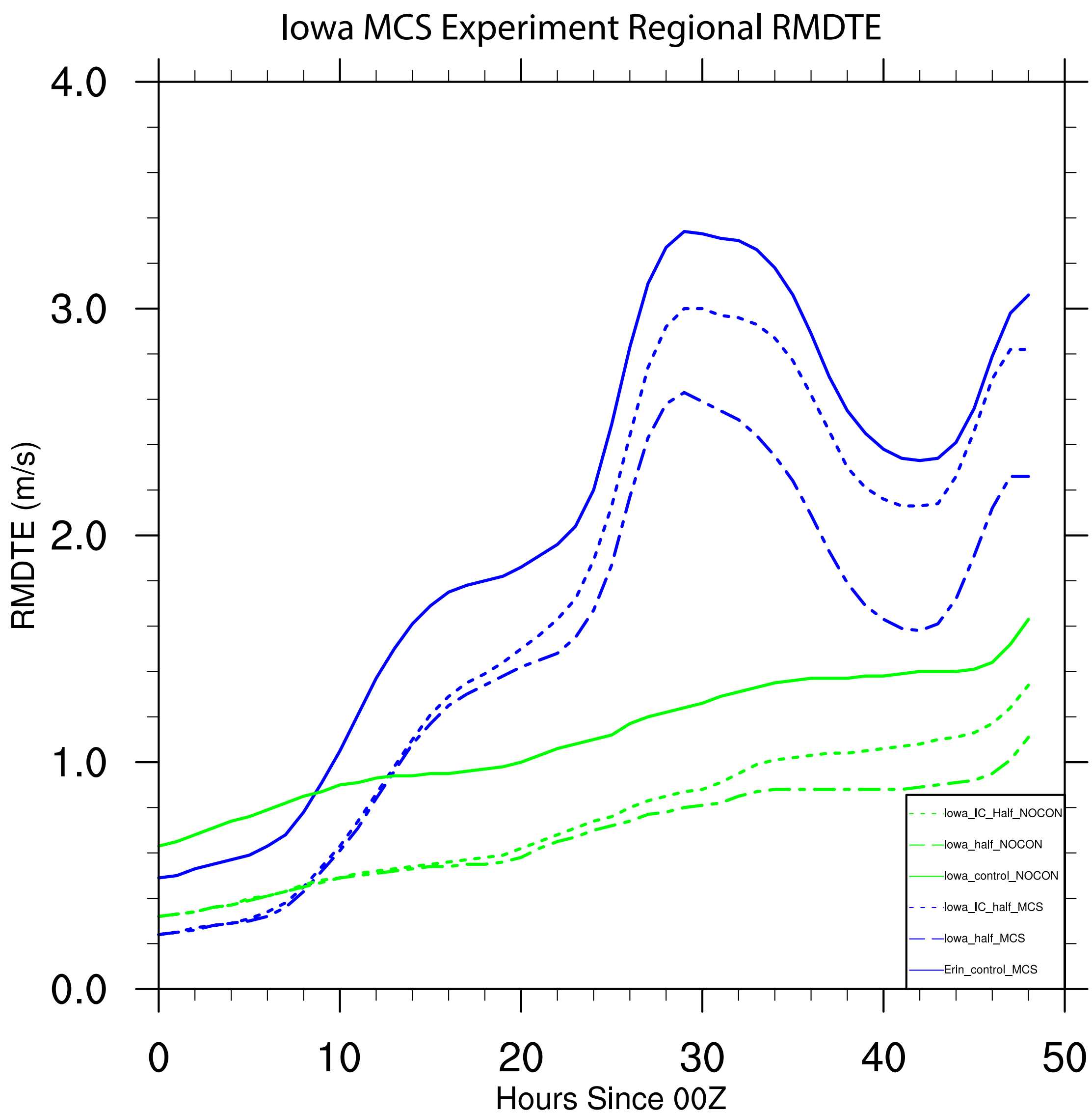

FIGURE 5.23. RMDTE time series for Iowa_control (solid lines), Iowa_half (dot-dashed lines), and Iowa_IC_half (dotted lines) for NOCON regional subset (green) and MCS subset (blue) as defined by dashed boxed regions centered in Texas and Wisconsin-Illinois border, respectively, in Fig. 5.19.

(know as "MCS subset") and a region associated with no significant convective rainfall (known as "NOCON subset"). Interestingly, the NOCON subset initialized with a higher RMDTE compared to the MCS region in Iowa_control (c.f., green and blue solid lines in Fig. 5.23); however, the RMDTE in the MCS region quickly increased with the onset of convection. The lower MCS regional RMDTE at initialization is likely due to large IC agreement in the location of the baroclinic zone in the region, which could be a reason for the underdispersive tendencies of the precipitation accumulations in this area. Conversely, the NOCON region has few defined large-scale atmospheric features identifiable within its boundaries. The lack of a large-scale atmospheric features in this region likely leads to large uncertainty in the state of the atmosphere in the ICs and leads to higher initial RMDE. There is significant reduction in the overall regional RMDTE from Iowa_control to Iowa_half (c.f., solid and dot-dashed lines in Fig. 5.23), which further illustrates the importance of the large-scale atmospheric flows on regional ensemble spread. A clear diurnal cycle is present in the MCS region, while there is a steady increase in the RMDTE of the NOCON region through time (Fig. 5.23). Based upon similar patterns seen in the Erin and Texas MCV cases, it makes sense for the MCS region, where convection is largely driven by various convective instabilities (i.e., Surface and Most-Unstable CAPE), to produce a diurnal cycle in the spread. The diurnal peaks in the case, however, are slightly offset from the normal expected convective times, due to the nocturnal nature of the convection in this case. The large reduction of the MCS regional RMDTE near F40 (Fig. 5.23) in the simulation again illustrates the importance of the large scale flow patterns in constraining the ensemble spread growth. Additionally, the AS metric yields similar results for the MCS subset here (Table 5.3) as the MCS region in the Texas MCV case (Table 5.2).

Table 5.3. Area spread (AS) metric for regions in ensemble experiments for the Iowa case above 25.0 mm and 50.0 mm precipitation accumulation thresholds. Accumulation period corresponds to windows of most intense rainfall previously identified in Fig. 3.2, and regions correspond to those identified and encompassed by solid boxes in Fig. 5.19.

Case	Region	25.0 mm	50.0 mm
Iowa_control	MCS	2.4	3.6

The ratios for these two subsetted regions, similar to the Erin and Texas MCV cases, shed some insight into the predictability of the regions. As discussed previously, the non-linear (Fig. 5.22) scaling between the ensemble runs, denoted by the increasing ratios in scaling seen between Iowa_control and Iowa_half, imply that these regions (including the full ensemble domain) are not at the theoretical limit of practical predictability. This means, as in the previously discussed cases, that the model architecture can be improved by further technical advancements. However, it also does not mean that the forecast cannot be improved by reducing the uncertainty in IC perturbations. Further, the RMDTE ratios do not converge to one for either the MCS or NOCON regions, which shows that these subsets are also not purely limited by intrinsic predictability. The RMDTE ratio increase means that RMDTE of regions in Iowa_half is increasing faster than in Iowa_control. If the increase of RMDTE ratio in the NOCON region can be used as a baseline for the increase in the RMDTE growth rate in Iowa_half due to practical predictability limits, as done in the Erin and Texas MCV cases, then the MCS region has some influence of intrinsic predictability limits on the spread evolution (i.e., since the RMDTE ratio is higher in the MCS subset; Fig. 5.22). The rapid increase in the MCS regional RMDTE ratio (blue line in Fig. 5.22) corresponds to the convectively active periods in the simulation. This, again, illustrates the importance of moist convection in creating intrinsic predictability limits in ensemble simulations of extreme precipitation events. Furthermore, the reduction in the MCS regional RMDTE ratio following its peak shows that the spread growth rate is constrained in Iowa_half by the large-scale atmospheric flow patterns. Thus, the Iowa ensemble experiments, similar to ones performed for Erin and the Texas MCV, spread growth is influenced by a combination of both practical and intrinsic predictability limits that is dependent on the amount of moist convection.

5.4. Summary and Conclusions of Ensemble Predictability Experiments

The ensemble predictability experiments illustrated the spread characteristics of a convection allowing ensemble prediction system for extreme precipitation events in the contiguous U.S. over the full model domain and on regional scales. The observed general spread characteristics over the full model domain were applicable to all cases and experiments performed. The main constraint, to first order, on the magnitude and growth rate of the model spread was found to be associated with large-scale atmospheric features. This was illustrated by several aspects of the ensemble experiments over the full model domain, including the diurnal cycle in the ensemble spread present in all cases, similar spread growth rates in the convection allowing ensemble compared to the native Reforecast-2 outside of model spin up and convectively active times, and the large decrease in the magnitude of the ensemble RMDTE when the ICs and LBCs were scaled. In other words, explicitly allowing convection does not lead to a rapid, unconstrained increase in the ensemble spread after convection develops, which in these cases is associated with extreme precipitation. This speaks to the viability of using convection allowing ensembles for prediction of events on multi-day timescales. Further, the choice of model initial conditions were shown to have impacts on the spread of the ensemble, even after two convective cycles in the Erin and Iowa runs. Additionally, over the full model domain, it was found that the RMDTE of the scaled runs (i.e., Erin_half, TX_third, and Iowa_half) increased at a faster rate than the control simulations (i.e., Erin_control, TX_control, and Iowa_control), as denoted by the increasing RMDTE ratios in all cases. The aforementioned overall large decrease in the RMDTE time series seen between the scaled and control runs illustrates the importance of the large-scale atmospheric forcing on the ensemble spread, since the RMDTE of the control simulations is always larger than the scaled runs. However, the faster rate of RMDTE increase in the scaled runs implies that upscale spread growth due to the resolution of convective scales is still present, but is second order to the large-scale influences. Furthermore, since a proportional scaling in the RMDTE between the scaled and control ensemble runs is not seen, this ensemble configuration is not at the theoretical limit of practical predictability and can be improved by modeling system advancements.

From a regional standpoint, some of the same characteristics that were seen over the full model domain can also be identified. First, the controlling constraint of the large-scale atmospheric features was seen across all of the subsetted regions. Specifically, similar to the full domain, the scaled ensemble runs produced lower RMDTE values across all times in all regions. This is encouraging for the viability of convection allowing ensembles, since the regional RMDTE did not continue to increase rapidly, despite the presence of constant convection within some of the subsetted regions. Interestingly, the magnitude of the ensemble RMDTE is not necessarily directly related to the spread seen in the precipitation accumulation, which here was determined using the area spread (AS) metric. There was a notable lack of the diurnal cycle in the subsetted RMDTE in regions of maintained heavy precipitation where there is an increased interaction between the convective and large-scale forcing (i.e., for instance in the Texas MCV case), which often drives faster spread growth rates. From a forecasting standpoint, this makes sense because regions of sustained convection need some sort of synoptic to mesoscale forcing for ascent to be maintained. Further, as in the full ensemble domain, the scaled ensemble runs RMDTE increased quicker than the control simulations across all of the subsetted regions, showing a similar secondary influence of small-scale error growth on the regional scale. The rate of the increase in the scaled over the control runs RMDTE, however, varied from region to region. Since the proportional scaling of the RMDTE between the scaled and control simulations is not maintained on both the full domain and regional scale, it lends more corroboration that this ensemble system is not at the theoretical limit of practical predictability. Further, no rapid convergence of the regional RMDTE ratio was seen between the scaled and control runs, implying that these regions are also not at the pure limit of intrinsic predictability. However, the subsets with extreme precipitation experienced faster RMDTE ratio increases over regions without any moist convection. The increase in the RMDTE ratio in the regions of no moist convection is most likely associated with not being at the theoretical limit of practical predictability, since there is little to no chaotic moist dynamics present, the main cause of intrinsic predictability limits, in these regions. Consequently, if a region has a larger RMDTE ratio increase than the areas void of convection within the same model run, some aspect of intrinsic predictability is influencing the spread growth in these regions, in addition to any spread growth associated with practical predictability limits. In all the cases and regions that experience heavy precipitation, the RMDTE ratios increased faster than the regions lacking moist convection from the same run. The degree on which the limit of intrinsic predictability affects the spread growth of a region can be seen in the RMDTE plots to be highly dependent on the amount of moist convection present in the simulations. Thus, in the cases of extreme precipitation studied here, the regional spread evolution appears to be influenced by a combination of intrinsic and practical predictability limits that is specific to the region and flow regime in place.

CHAPTER 6

Results: Terrain-Induced Precipitation Variability Experiments[1]

The development of heavy precipitation along the Balcones Escarpment in all of the cases allows for the exploration of the effects of removing the terrain feature. Each case will be discussed individually below. The differences in precipitation, and other possible meteorological reasons for those differences between the control and terrain-modified simulations are examined in the following chapter for each of the identified events.

6.1. 9 June 2010

In the control simulation, the areal coverage of heavy precipitation (>50 mm) (Fig. 6.1a) is smaller than that shown in the precipitation analysis (Fig. 3.2a), and the largest observed accumulations are underpredicted. On the other hand, there is a broader northwest extent of precipitation in the simulation. A slower MCV motion was produced in the control run compared to the observations, which is one possible reason for the difference in accumulated rainfall. Despite these errors in the precipitation placement, the simulation of substantial precipitation along the Balcones Escarpment still provides a modeled environment that is adequate to perform this experiment.

Both simulations produced heavy precipitation in the same area, with the magnitude of the largest accumulations being similar. There were two primary differences between them, however: the development of a region of organized precipitation accumulation to the

[1]This chapter and the associated methods, introduction, and case descriptions will be published by the American Meteorological Society in *Monthly Weather Review*: Nielsen, E. R., R.S. Schumacher, and A.M. Keclik, 2016: The effect of the Balcones Escarpment on Three Cases of Extreme Precipitation in Central Texas. *Mon. Wea. Rev.*, **144 (1)**, 119–138. doi: 10.1175/MWR-D-15-0156.1. ©2015 American Meteorological Society. Used with permission.

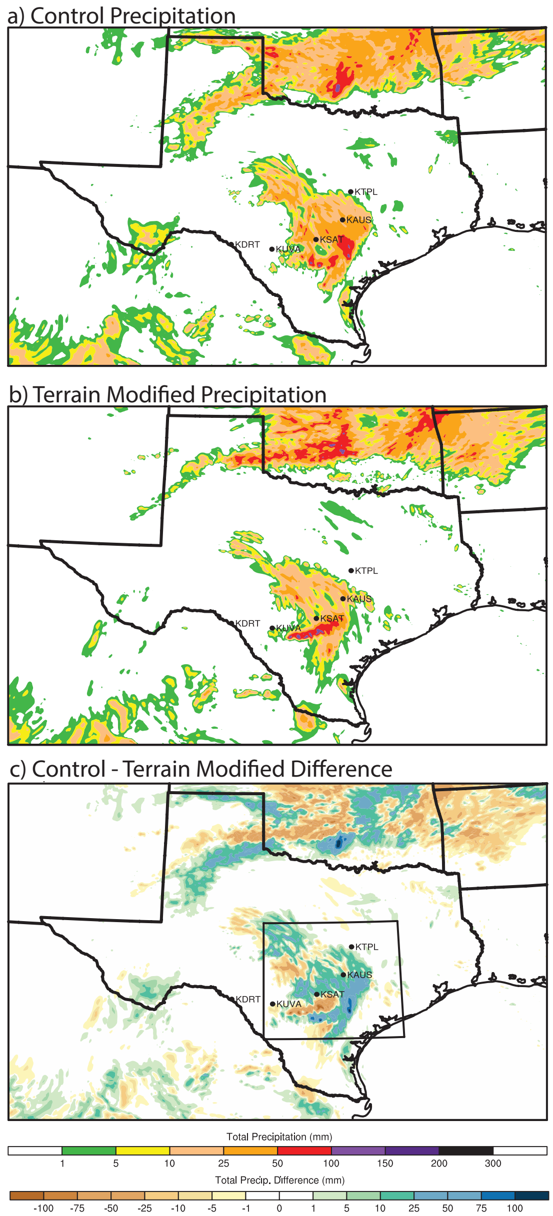

FIGURE 6.1. Modeled precipitation output for 09 June 2010 flooding event valid from for the 18-hr period ending 1800 UTC 09 June 2010. Color scale and time period correspond to NCEP Stage IV observations shown in Fig. 3.2a. Panel (a) corresponds to precipitation simulated by control run, (b) the terrain modified run, and (c) the control run minus terrain modified run precipitation difference where cold (warm) colors represent large values in the control (terrain modified) run. Boxed area in (c) represents the area over which the precipitation was averaged to create the Hovmöller plots to follow.

south of KSAT stretching to Uvalde, TX (KUVA) in the terrain-modified simulation that is not present in the control run (cf. Figs. 6.1a,b), and more precipitation to the southeast

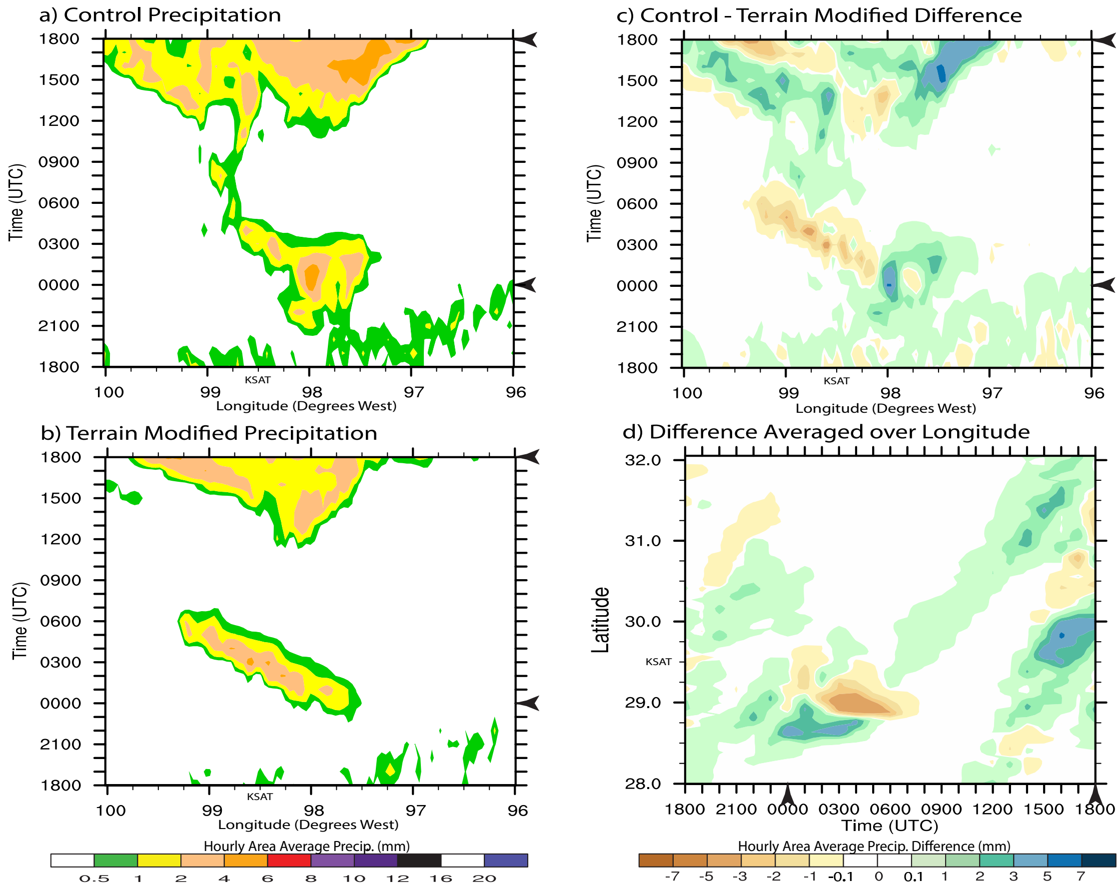

FIGURE 6.2. Hovmöller (time-longitude) diagrams averaged over box in Fig. 6.1c valid for the 24-hr period beginning 1800 UTC 8 October 2010. Panel (a) represents the control run, (b) the precipitation modified run, and (c) the control minus terrain modified run difference, where cold (warm) colors represent larger values in the control (terrain modified) run. Panel (d) is the same as (c), except the area averaging has been done over latitude. The approximate longitude of San Antonio International Airport (KSAT) is noted and will be on future figures. Black arrows on right side of plots denote time period over which precipitation accumulations are plotted in Fig. 3.2a and Fig. 6.1.

of KSAT in the control run compared to the terrain-modified run (Fig. 6.1c). Hovmöller diagrams (Hovmöller 1949) (Fig. 6.2) reveal that the averaged difference between the two runs develops initially around 0000 UTC on 09 June 2010. The precipitation in the control run remains more stationary (Fig. 6.2a) in the KSAT area, while the precipitation in the terrain-modified run has a persistent westward motion with time (Fig. 6.2b). Conversely, the band of heaviest precipitation in the terrain-modified run is better organized, explaining

Table 6.1. Area-averaged precipitation for the control and terrain modified run in each case analyzed. Differences calculated off the control run. Region over which average is taken corresponds to geographic spatial extent shown in all precipitation plots (e.g. Fig. 6.1,6.3,6.5 etc.) bounded by roughly 25°N to 36.5°N and 91°W to 107°W.

Case	Control Run (mm)	Terrain Mod. Run (mm)	Diff. (mm) Diff. (%)
31 October 2013	0.43	0.46	+0.03 (7.0%)
9 June 2010	0.22	0.20	-0.02 (9.0%)
25 May 2013	0.16	0.15	-0.01 (6.2%)
25 May 2013, 3/4 Pert.	0.15	0.16	+0.01 (6.7%)
25 May 2013, 1/2 Pert.	0.13	0.15	+0.02 (15.3%)

the larger accumulations within that band. The precipitation in the control run initiates slightly earlier, further to the east (Fig. 6.2c) and south (Fig. 6.2d) than the terrain-modified run without the Balcones Escarpment. While the location of the precipitation is altered with the removal of the Balcones Escarpment, the occurrence and relative magnitude (Table 6.1) were not affected. In particular, the result that a better-organized MCS emerged in the terrain-modified run, and was in a location parallel to the Escarpment (except with the Escarpment removed), illustrates that this terrain feature is not necessarily the primary mechanism supporting heavy-rain-producing MCSs in this area.

6.2. 31 October 2013

The 31 October 2013 case differs from the other two cases presented here in that it occurred when strong synoptic-scale (rather than mesoscale) forcing for ascent was present. This can be seen in the large area of precipitation accumulation over the 12-hour period ending 1200 UTC 31 October 2013 (Fig. 3.2b). The control run for this case produced a fairly

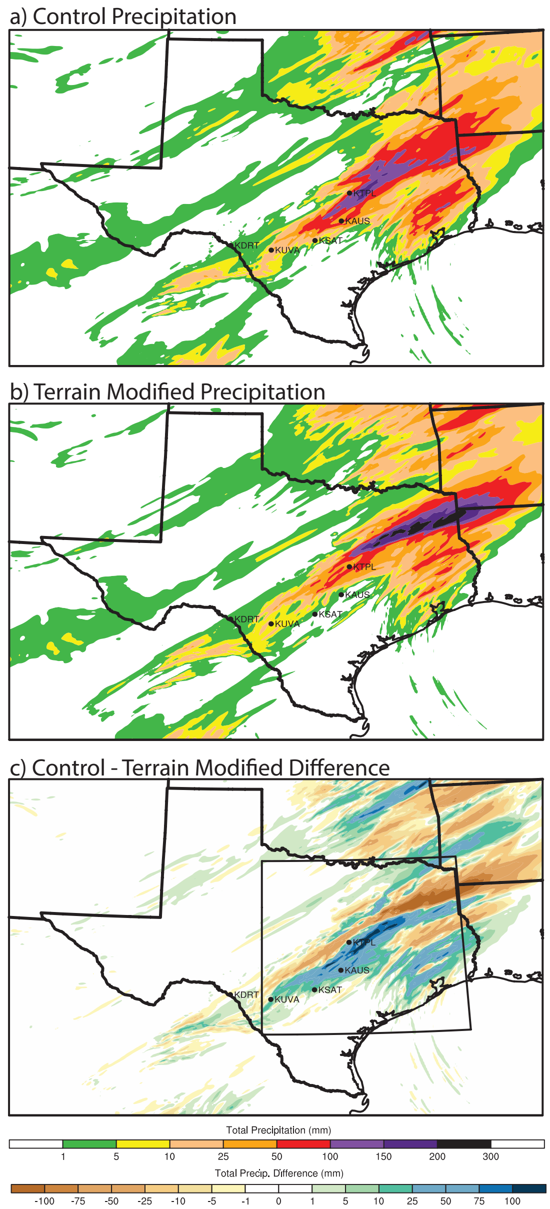

FIGURE 6.3. As in Fig. 6.1 but in reference to the 31 October 2013 flooding event. Precipitation accumulation is for the 12-hr period ending 1200 UTC 31 October 2013.

representative precipitation pattern over this same period (Fig. 6.3a) but did not reproduce the magnitude of extreme precipitation observed near KAUS (Fig. 3.2b). Furthermore, the heaviest precipitation swath in the control run did not reach as far south as in the observations. Similar to the other control runs in this study, the placement of precipitation along the Balcones Escarpment is sufficient to test the influence of the terrain feature.

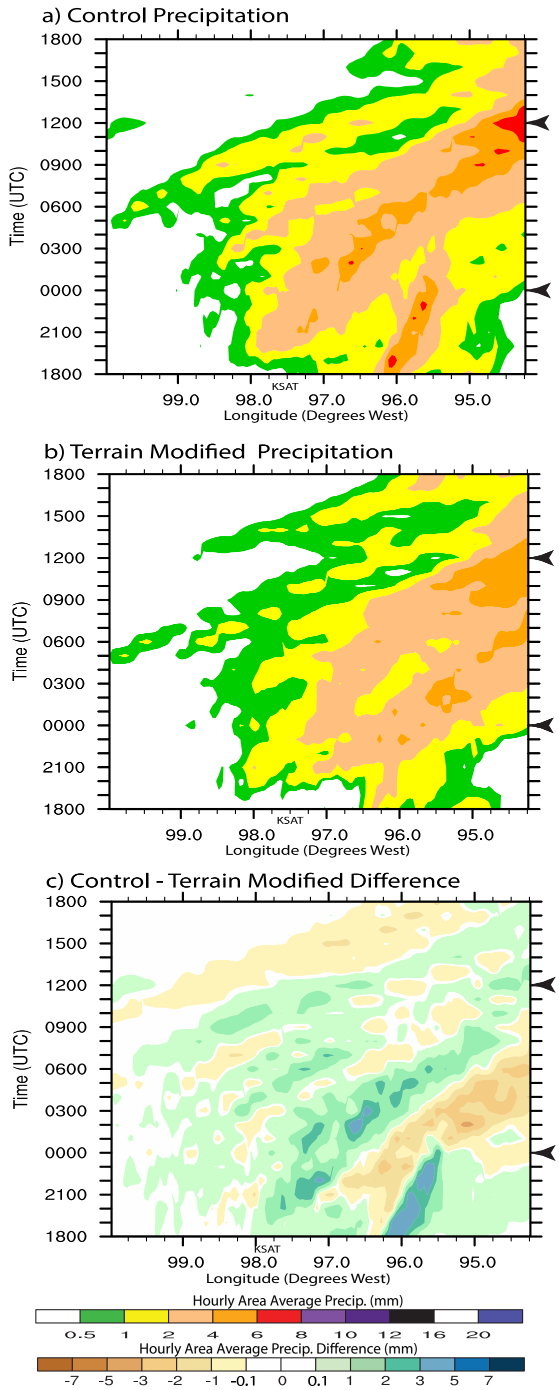

FIGURE 6.4. As in Fig. 6.2a–c, except for the 24-hour period beginning 1800 UTC 30 October 2013).

The overall precipitation pattern between the control run (Fig. 6.3a) and the terrain-modified run are fairly similar, except for spatial shifts in the main bands of precipitation as seen in the accumulation difference plot presented in Fig. 6.3c. The terrain-modified run produces precipitation in the same southwest-northeast line as the control run but is offset to the northwest (Fig. 6.3c). In fact, this pattern is not limited to the region associated with the Balcones Escarpment. Hovmöller diagrams show that the most noticeable difference occurs in the eastern part of Texas between 0200-0400 UTC on 31 October 2013 (Fig. 6.4). The terrain-modified run has a larger amount of precipitation farther to the east around 0300 UTC (Figs. 6.3, 6.4c) compared to the control run. However, this signal is associated with precipitation differences in northeast Texas (Fig. 6.3c) near the terrain-modified run maximum, while the control run has a maximum near Temple, Texas (KTPL). This difference is far removed from the terrain modification, however. Near the region of terrain modification, Fig. 6.4c shows precipitation accumulation being slightly higher for the terrain-modified run and shifted to the west compared to the control run at similar time periods (e.g., 0600 UTC and 1000 UTC). This illustrates over time the eastward (westward) shift in the precipitation maximum when the Balcones Escarpment is included (not included) that is seen in Fig. 6.3c. The precipitation accumulation swaths in both runs do still move from west to east, which is not surprising given the strong upper-level winds associated with this case. Similar to the previous case, a shift in the precipitation patterns to the northwest is observed near the region of terrain modification; however, the overall characteristics and precipitation (Table 6.1) of the event remained comparable.

6.3. 25 May 2013

The control simulation for the 25 May 2013 case produces a broad region of intense rainfall, with localized totals exceeding 300 mm (Fig. 6.5a). The control run precipitation shield is shifted to the northwest in comparison to the analyzed precipitation (Fig. 3.2c), with further precipitation production in west Texas. Numerical simulations, including almost

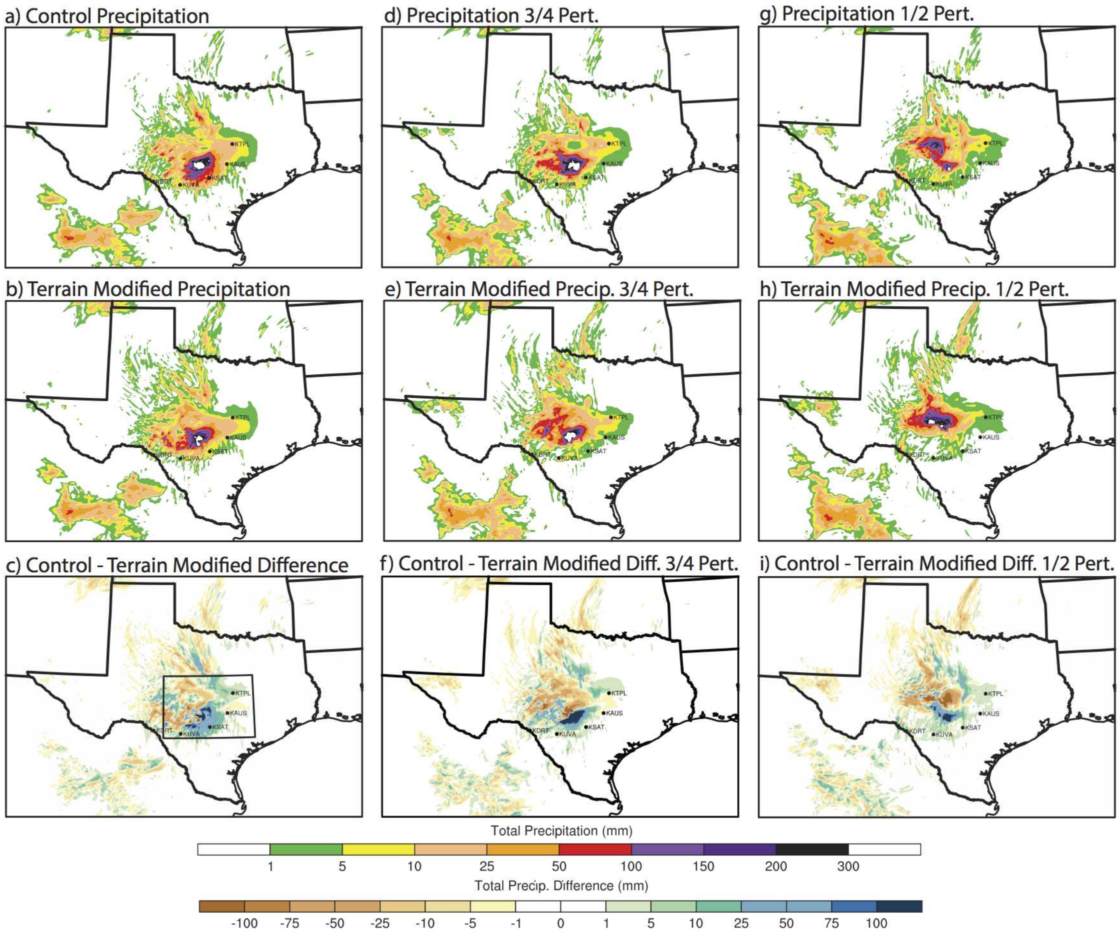

FIGURE 6.5. Modeled precipitation output for the three experiments performed for the 25 May 2013 flooding case valid for the 12-hour period ending 1800 UTC 25 May 2013. The first column (a-c) represents the full perturbation simulation associated with the ICs of member nine of the Reforecast-2 ensemble, second column (d-f) represents three-quarters of the full perturbation, and third column (g-i) represents one half of the full perturbation. Row one (a,d,g) corresponds to the precipitation from the control, row two (b,e,h) to the precipitation from the terrain-modified run, and row three (c,f,i) to the control minus terrain-modified difference, where cold (warm) colors represent larger values in the control (terrain-modified) run. The boxed region in (c) depicts the area over which precipitation was averaged to create the Hovmöller plot for the control simulation in Fig.6.6.

all members of the Reforecast-2 ensemble, did not move the parent MCV far enough south to replicate the observed precipitation pattern.

The precipitation patterns in the control and terrain-modified simulations are quite similar (cf. Figs. 6.5a,b). Fig. 6.5c illustrates that the precipitation maximum in the control run is located southeast of that in the terrain-modified run, or in other words, implies that the removal of the Balcones Escarpment would serve to shift the maximum precipitation to the northwest. However, similar to the other runs, there is not a substantial change in total precipitation when the Balcones Escarpment is removed (Table 6.1).

The control and the terrain-modified runs initially both produce a nearly stationary region of precipitation to the west of KSAT (Figs. 6.6a,b). However, a general shift in precipitation to the west in the terrain-modified run throughout the analyzed period can be seen. This signal is clearest during the time of heaviest rainfall around 1200 UTC, as seen by the dipole in Fig. 6.6c. The terrain-modified run produces a swath of higher area-averaged precipitation (Fig. 6.6b) compared to the control run (Fig. 6.6a) at the time of heaviest precipitation ($\sim$1200 UTC) from 100.5 to 99.0 degrees west. However, the control run produces a locally more intense region of precipitation around 99.0 degrees west and further east near 98.75 degrees west (Fig. 6.6a). Although precipitation shifts to the north and west and local changes in accumulation maxima are seen when the Balcones Escarpment is removed, both simulations produce a heavy rain event of similar magnitude and spatial distribution.

The evolution of the precipitation and near-surface boundaries in the control and terrain-modified runs is broadly consistent with the observations from the event. A large, north-south oriented squall line (not shown) passed through the region and decayed early on 25 May 2013. This MCS left a broad cold pool over the area (Fig. 6.7a) that influenced the initiation and evolution of new convection associated with the 25 May heavy rain event. The convection responsible for the main flooding event originally initiated and organized between 0500–0800 UTC along the preexisting temperature gradient near the Balcones Escarpment (c.f. Fig. 6.7b and Fig. 6.7e). As convection continued to initiate, cold pools reinforced the

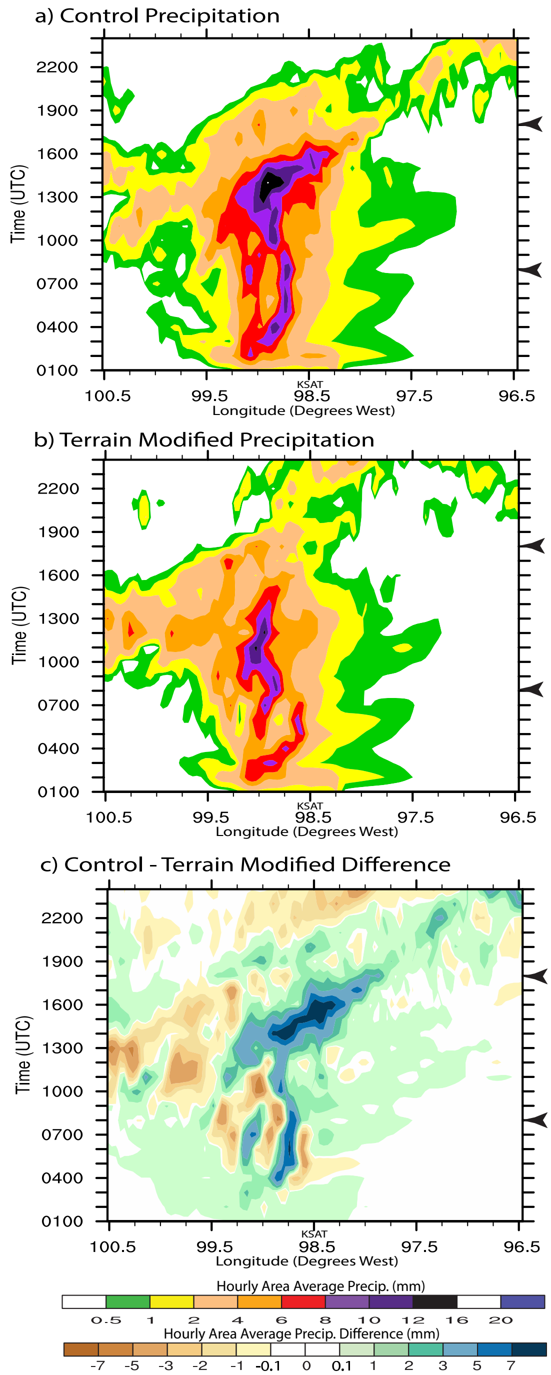

FIGURE 6.6. As in Fig. 6.2a–c, except for the 23-hour period beginning 0100 UTC 25 May 2013).

thermal gradient on the southern flank of the precipitation (Fig. 6.7e). In the control run (Figs. 6.8a,b,c), the preexisting temperature gradient is similarly located along the Balcones Escarpment (Fig. 6.8a) but is lacking a tongue of high-θ_v air to the southwest and is located

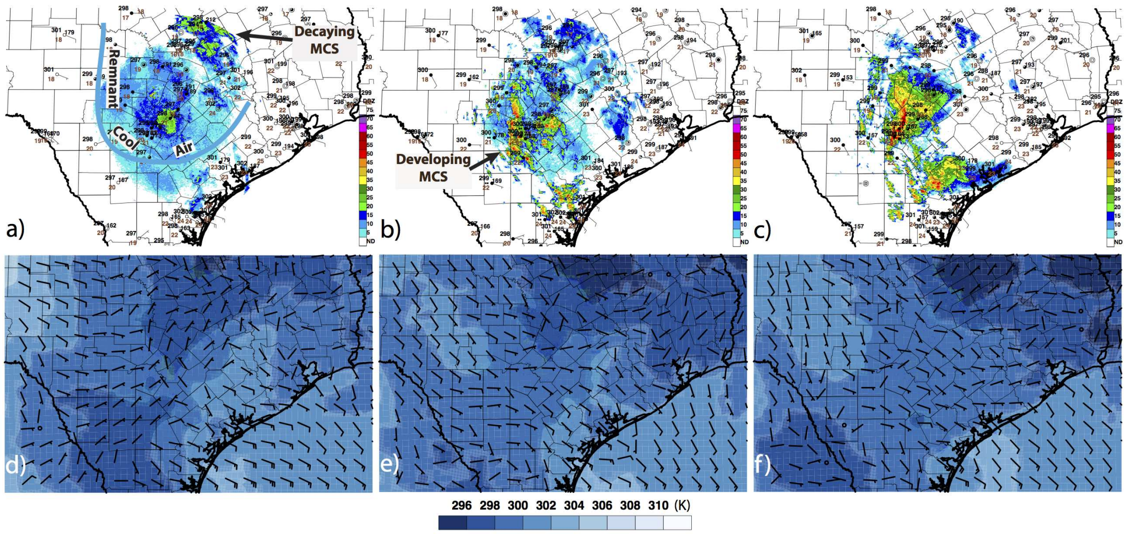

FIGURE 6.7. Surface observations with virtual potential temperature (K) in black and dewpoint temperature (°C) in brown valid (a) 0400, (b) 0800, (c) 1100 UTC 25 May 2013. Base radar reflectivity (dBZ) from the Austin/San Antonio NWS radar (EWX) is overlaid valid (a) 0400, (b) 0804, and (d) 1102 UTC 25 May 2013. Features discussed in the text are marked (e.g., developing/decaying systems and remnant cool air). Virtual potential temperature (contoured every 2K) from the Rapid Refresh (RAP) Hourly Analysis valid (d) 0400, (e) 0800, (f) 1100 UTC 25 May 2013 with wind barbs from 10 m above ground overlaid.

slightly west of the analysis. While convection initiates slightly earlier in the model (around 0400 UTC; Fig. 6.8a) compared to observations, the subsequent evolution of the temperature gradient and cold pool is similar to what was observed. When the Balcones Escarpment is removed, the preexisting thermal gradient is located in the same area as in the control run, although the values of θ_v are different owing to the change in elevation (Fig. 6.8d). In the terrain-modified run, convection initiates at nearly the same time as the control run, and the evolution of the convectively generated cold pools are very similar despite the removal of the Balcones Escarpment (c.f. Figs. 6.8b,c and Figs. 6.8c,f). Although the near-surface temperature gradients set up along the Balcones Escarpment, these results show that they are not caused by the presence of the terrain feature. Thus, in this case, the mesoscale forcing mechanisms and preexisting conditions have a larger impact in determining where the convection initiates than does the Balcones Escarpment.

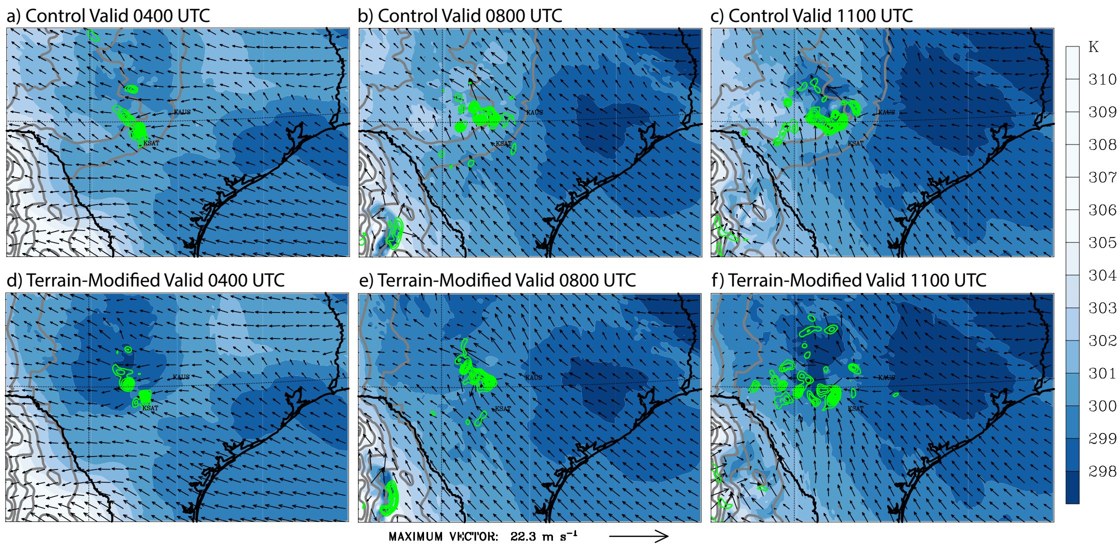

FIGURE 6.8. Contoured (fill colors) virtual potential temperature on the second lowest terrain following model level, wind (vectors) at the same level , and vertical velocity at 3 km above mean sea level (contoured every 50 cm s^{-1} starting at 50 cm s^{-1} in green) for the control (top row) and terrain-modified runs (bottom row). Terrain is contoured every 250 m in grey. Panels (a,d) are valid at 0400 UTC 25 May 2013, (b,e) are valid three hours later at 0800 UTC, and (c,f) are valid at 1100 UTC the same day.

Vertical sections through the MCS during its mature stage reveal that the inflow region is characterized by a strong southerly lower level jet (LLJ) and the gradual isentropic upglide associated with mature MCVs (e.g., Fritsch et al. 1994; Trier et al. 2000c,d; Schumacher and Johnson 2009). At 1100 UTC, the simulated reflectivity pattern is quite similar between the two runs, although a slight shift in the location of the convection can be seen (Figs. 6.9a,b). The meridional inflow in both the control and terrain-modified runs from 1 to 2 km in height above mean sea level exceeds 20 m/s (Figs. 6.9c,d). Furthermore, the inflow in the control run is maximized well above the maximum terrain slope, and the wind speeds are similar between the two runs, suggesting that there is minimal influence of orographic lift on the inflow to the MCS. The inflow in the terrain-modified run is at approximately the same

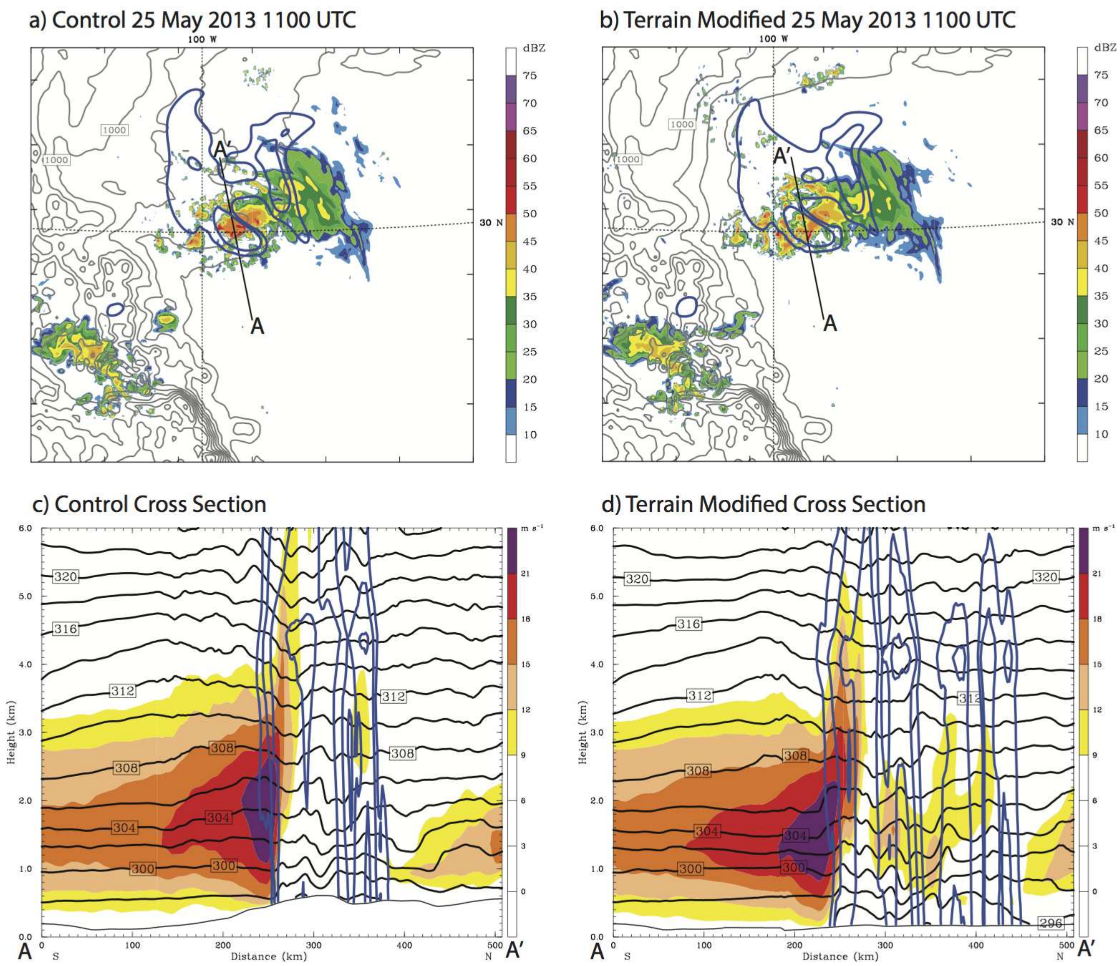

Figure 6.9. Simulated radar view and cross sections valid 25 May 2013 1100 UTC for control (left column) and terrain-modified runs (right column). Panels (a,b) depict simulated radar reflectivity at 1.5-km above mean sea level contoured (fill colors), terrain elevation (gray contours ever 250 m from 250-2500 m), potential vorticity at 600 hPa valid 0600 UTC same day around the time of convection initiation [PVU (potential vorticity unit); 1 PVU = 10^{-6} K kg^{-1} m^{2} s^{-1}] (blue contours at 1 PVU and 1.5 PVU), and black line (A-A’) represents the horizontal depiction of cross section. Panels (c,d) show cross sections along line in (a,b) of meridional wind speed (shaded according to color scale), potential temperature surfaces in black contours every 2 K, and radar reflectivity in blue (contoured every 10 dBZ from 20-50 dBz).

height above ground as the control run, and near surface cold pool of similar magnitude exists in both runs (Figs. 6.9c,d). The spatial pattern and extent of the cold pools differ slightly; however, this may be because negatively buoyant downdrafts have less distance to travel to reach the ground in the control run versus the terrain-modified run. If the downdrafts have less vertical distance to travel, all else being equal, the time available for evaporative cooling is reduced, and more time is available for the cold pool to spread out. The cross sections (Figs. 6.9c,d) show a shift in the highest simulated reflectivities to the north by about 10-20 km, consistent with the plan view precipitation maps shown earlier (Fig. 6.5). In general, the structure and evolution of the atmospheric forcing for convection is nearly identical whether or not the Balcones Escarpment is included, with its main influence being a small shift in the location of the maximum precipitation.

To further investigate the robustness of the northward and westward shift in precipitation discussed above, the perturbation used to create the ICs and LBCs for member nine of the Reforecast-2 ensemble was isolated and scaled by 0.75 and 0.5 to create two new numerical simulations for the 25 May 2013 case. These additional two runs create a mini-ensemble for this case that allows for further examination of the effects of the Balcones Escarpment. A more complete method would have been to run the entire Reforecast-2 ensemble with terrain modification; however, only member nine produced any precipitation near the Balcones Escarpment. With no precipitation predicted, the effects of the terrain modification cannot be analyzed. Thus, the scaling of the ensemble perturbation associated with member nine was undertaken as an alternative.

In both the three-quarter and half perturbation runs, a very similar spatial precipitation pattern develops compared to that in the control run, consistent with a southward moving MCV (Fig. 6.5). The heaviest precipitation in the full-terrain version of these simulations is displaced northwest of that in the control (Fig. 6.5), but the area-averaged precipitation accumulation is similar (Table 6.1). When the Balcones Escarpment is removed in both of the scaled perturbation runs, the precipitation accumulation shifts even farther to the north and west (Figs. 6.5f and 6.5i). There are varying magnitudes and orientations of the precipitation difference dipole in all three cases (Figs. 6.5c, 6.5f, and 6.5i) for the 25 May 2013 event, but the general shift in the precipitation when the Balcones Escarpment is removed is seen in all three. This increases the confidence that the precipitation shift in all of the study simulations are not associated with chaotic convective dynamics but the terrain feature itself.

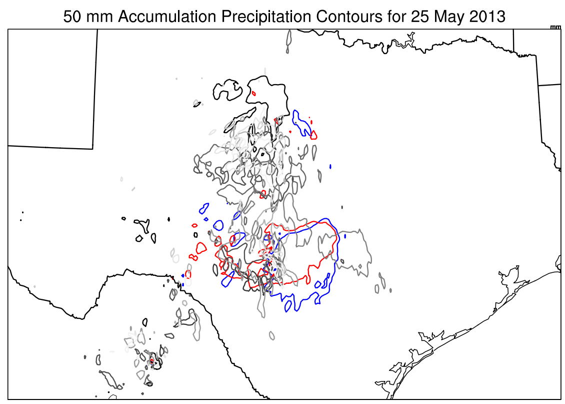

FIGURE 6.10. Contours of 50 mm precipitation accumulation from ensemble output for the 25 May 2013 case valid the 12-hour period ending 1800 UTC 25 May 2013. Contoured in different hues of grey are 50 mm precipitation accumulation for each member of a 4-km WRF ensemble created from the ICs and LBCs of the Reforecast-2 ensemble initialized 0000 UTC 25 May 2013. Blue contours correspond to the full perturbation control run for the 25 May 2013 case, and red contours correspond to the full perturbation terrain-modified run.

The simulations for all of the cases so far have also shown, to first order, very little difference in the pattern or magnitude of the precipitation between the control and terrain-modified runs, but that there are spatial shifts in precipitation pattern. This suggests that atmospheric processes have much more control over the distribution of precipitation than do the details of local topography. One way to put these spatial variations into context is to examine how they compare to the variations associated with uncertainties in the large-scale atmospheric pattern. This was done by comparing the differences between the control and terrain-modified simulations to the output of the full 11-member Reforecast-2 ensemble downscaled to 4-km grid spacing with WRF. Fig. 6.10 shows that the 50-mm rainfall contours from the control and terrain-modified runs largely overlap, but there is much larger spread in the ensemble with varied ICs and LBCs. In other words, the spatial shift in precipitation associated with removing the Balcones Escarpment is much less than the spread in precipitation due to the atmospheric variability represented by the full ensemble. This corroborates the findings from the other simulations that while the Balcones Escarpment does slightly shift the location and in some instances focus the precipitation, it is not alone responsible for the heavy precipitation, nor does it determine the overall magnitude of the event.

6.4. Discussion

In an effort to evaluate the effect that the Balcones Escarpment has on the flow impinging on it, a Froude number analysis of the low-level flow in the three presented cases was undertaken. The mountain Froude number, $Fr = U/Nh_m$, where U is the speed of the flow perpendicular to the obstacle, h_m is the height of topographic feature, and N is the Brunt-Väisällä frequency is often used to determine if flow blocking by terrain will occur (Markowski and Richardson 2010). If $Fr < 1$, then some depth of the flow will be blocked by the terrain feature. The Fr for each case was calculated from the observed sounding presented in Figs. 3.4d, 3.7d, and 3.6d over the lowest 600 m of the atmosphere. The height of the Balcones Escarpment was approximated to be 400 m and the meridional component of the wind, which is approximately perpendicular to the western part of the Balcones Escarpment (Fig. 2.9a), averaged over the lowest three sounding observations was taken to represent U. The analysis resulted in Froude numbers from ~ 2.0 to ~ 2.4, indicating that the flow impinging on the Balcones Escarpment in these three cases is not blocked by the terrain feature. Considering that all three soundings show weakly stable low-level temperature profiles and strong low-level meridional winds, this situation is not conducive to blocking by small topographic variations. While this result is not surprising given the vertical extent of the Balcones Escarpment, it speaks to the nature of the orographic lift and flow interactions in these three extreme rainfall events central Texas. Further, it illustrates one of the problems with comparing the orographic effects associated with the Balcones Escarpment to other topographic features with a larger vertical extent (e.g., Rocky Mountains, Massif Central, Blue Ridge, Black Hills, etc). In similar environmental conditions, obstacles of only 1000 m would be needed to produce regimes where blocking of some depth of the flow is likely (i.e., $Fr < 1$). Given these flow-blocking differences, it would be difficult to directly compare the results from this study to those focused on terrain features with a larger vertical extent. Furthermore, these aforementioned terrain features have a larger spatial expanse and are located closer to other large topographic features (e.g., the Alps in the case of the Massif Central) that create flow patterns that further complicate the orographic influences.

While the simulations show that the Balcones Escarpment is the apparent cause of the precipitation shift, the exact meteorological differences that cause the shift in precipitation when the terrain feature is removed are difficult to discern because the shift is so subtle. The specific mechanisms for the shift appear to be related to a combination of the differences in the spread of cold pools and possibly slight differences in the location where air parcels arrive at their LFCs because of small reductions in ascent when the terrain is removed. The author agrees that understanding these differences is an important scientific goal, and had the differences between the runs been larger (as the author hypothesized they would be) it would be easier to make firm conclusions about the reasons for the differences. Given this, identification of the exact meteorological cause of the precipitation shift would be a good topic for continued research from an idealized modeling standpoint. Consequently, the author is currently developing and running idealized simulations to attempt to address these questions in future work.

6.5. Summary and Conclusions of Balcones Escarpment Experiments

In this study, three different heavy precipitation and flash flood events were examined to evaluate the effect the Balcones Escarpment has on extreme precipitation in central Texas. Each event had different synoptic or mesoscale characteristics but all resulted in flooding damage and fatalities along the terrain feature. Numerical simulations were run using WRF-ARW at a convection allowing grid spacing to ensure that a reasonable representation of the event was produced along the Balcones Escarpment. For each case, an experiment was conducted in which the elevation gradient associated with the Balcones Escarpment was removed.

To first order, the removal of the Balcones Escarpment did not change the precipitation characteristics of the events presented in this study. The occurrence and magnitude of the events were not significantly altered with the overall spatial pattern and area-averaged precipitation showing little change when the terrain feature was removed. However, a shift in the precipitation to the north and west was found in simulations of all three cases. This shift in precipitation associated with removing the Balcones Escarpment, when compared to a WRF-ARW ensemble based on the parent Reforecast-2 ICs and LBCs, was much smaller than shifts associated with typical ensemble variability. Although hydrologic factors associated with the Balcones Escarpment make central Texas prone to flooding, it does not appear to cause the extreme precipitation events, of the scale analyzed in this study, that lead to flooding. Based on the results of this study, it was concluded that when the synoptic to mesoscale ingredients for extreme convective precipitation are in place over the Balcones Escarpment, the terrain does not directly affect the occurrence or magnitude of precipitation in the region. However, it does appear to affect the spatial distribution of the accumulated rainfall in a small but consistent way, namely by shifting the axis of heaviest precipitation slightly to the northwest. Results could be expected to be different for higher topographic features when some depth of the flow is blocked.

CHAPTER 7

Conclusions and Future Work

7.1. Ensemble Predictability Experiments

The various ensemble experiments illustrate the spread characteristics associated with three extreme precipitation events in a 11-member convective allowing ensemble. The main constraint over the full model domain on the ensemble spread was found to be associated with large-scale atmospheric features. This was largely shown by the decrease in the overall RMDTE magnitude when the perturbations off the control member were reduced, and the diurnal cycle in the RMDTE seen across all ensembles run for this study. The latter result is particularly illustrative, since it shows that small-scale errors associated with convection that are created at the convective-allowing scale are constrained by the large-scale features. The increased resolution to explicitly allow convection does not lead to unconstrained ensemble spread growth, which is encouraging for the use of such ensembles for multi-day forecasts. It was also shown that the choice of ICs for the ensemble still have some affect on the ensemble spread out to at least 48-hr. Additionally, the RMDTE of the scaled ensemble runs (i.e., Erin_half) increased faster than the RMDTE of the control simulations (i.e., Erin_control). This illustrates that the upscale spread growth from the convective scales is still present but appears to be a second order to the reduction of the spread observed when the ensemble perturbations are scaled. Further, since a perfectly proportional scaling of the RMDTE is not seen between the scaled and control ensemble runs, this implies that this ensemble is not at the theoretical limit of practical predictability, and its modeling architecture can be improved.

Many of the same aforementioned ensemble spread characteristics were also seen on more regional spatial scales, including the diurnal cycle and reduction in magnitude of the overall RMDTE in the scaled ensemble runs. Regions of sustained convection experienced a significantly muted diurnal cycle in the spread, owing to the maintained interaction between the convective and larger-scales that is necessary to induce multi-day convective events. As over the full model domain, the regional RMDTE of the scaled ensemble runs increased faster than the same regional RMDTE of the associated control ensemble, showing a similar secondary influence of the small-scale error growth on the regional RMDTE. This further hints that this ensemble configuration is not at the theoretical limit of practical predictability because a proportional scaling between the scaled and control ensembles is not maintained. Additionally, no rapid convergence of RMDTE magnitude between the scaled and control ensembles was seen, which shows that these cases are also not at the pure limit of intrinsic predictability. However, the amount of convergence of the regional RMDTE between the scaled and control ensembles varied based upon the amount of moist convection within the region. Thus, it is not unreasonable to conclude (more detailed discussion is given in section 5.4) that the regional spread evolution is influenced by a combination of both intrinsic and practical predictability limits that is highly dependent on the amount of moist convection present.

There are many avenues to advance and elaborate on the conclusions found in the ensemble predictability section of this study. One ongoing set of experiments is creating scaled ensembles for the Texas MCV case that reduce the perturbation off the control member much more significantly (i.e., scaling the perturbations by 1/10, 1/20, and 1/100). This could potentially allow for the isolation of the overall RMDTE spread growth associated with the chaotic nature of moist convective dynamics for these events, since the dominating large-scale spread has been significantly reduced. Expanding on this idea, it would also be illustrative to decompose the RMDTE by wavelength, both on a regional and full domain scale. A spectral decomposition of the RMDTE would allow for the identification of the scales at which the ensemble spread is growing the quickest. Furthermore, it could be used to shed insight on the scales that are the most influenced by convective or synoptic scale processes. This could in turn have could serve to provide a look at the precise scales that are indicative of the spread growth associated with the practical and intrinsic predictability limits. Lastly, given the underdispersive tendencies observed in some regions of the model configuration used, adding small-scale perturbations to the ensemble LBCs (e.g., Nutter et al. 2004b) could be used as a method to increase the dispersion. If the ensemble spread is increased due to the addition of small-scale errors on the LBCs, it could change the relative importance of large-scale atmospheric features on the ensemble spread that was found in this study. Given the large model domain used in these experiments, this influence is potentially more muted (compared to a smaller domain), but should still be investigated. The main goal of these future avenues of exploration will be to nail down the specific atmospheric scales that contribute most to the ensemble spread growth in extreme precipitation events.

7.2. Terrain-Induced Precipitation Variability Experiments

In this study, the terrain-induced precipitation variability associated with the Balcones Escarpment in central Texas, during three recent extreme precipitation events, was examined. Specifically, NWP simulations for these events where conducted with the elevation gradient associated with the Balcones Escarpment removed. The removal of the terrain feature did not significantly change the overall occurrence or magnitude of the precipitation events. Although, in all of the cases examined, a persistent shift in the precipitation accumulations to the north and west was seen. Further, this shift in precipitation associated with the terrain modification was much smaller than precipitation shifts seen in typical atmospheric variability, as represented by the precipitation accumulations of the full downscaled Reforecast-2 ensemble. Therefore, when the atmospheric ingredients for extreme precipitation are present over the Balcones Escarpment, the terrain feature does not directly affect the magnitude or occurrence of the extreme precipitation event. It does, however, affect the spatial distribution of the precipitation, by shifting the rainfall accumulations to the north and west. It should be noted that, while the Balcones Escarpment does not seem to directly affect the occurrence and magnitudes of these extreme precipitation events, the terrain feature does directly lead to an increased hydrological propensity for dangerous flash flooding.

Ongoing work will attempt to examine the effect of the terrain rise on smaller scale atmospheric phenomena, such as an isolated thunderstorms. Since there is a spectrum of convective processes that can produce locally heavy precipitation, it is important to fully understand the meteorological influences the Balcones Escarpment has in this flood-prone region. Further, the effect of the terrain feature on the evolution of convective cold pools will be examined using idealized model simulations. The combination of the cold pool and terrain-induced affects on convective initiation and cell motion are a locally important process to understand, especially due to the high flash flooding risk in the area.

Bibliography

Alcott, T. I., and W. J. Steenburgh, 2013: Orographic influences on a great salt lake–effect snowstorm. *Mon. Wea. Rev.*, **141 (7)**, 2432–2450, doi:10.1175/MWR-D-12-00328.1.

Arndt, D. S., J. B. Basara, R. A. McPherson, B. G. Illston, G. D. McManus, and D. B. Demko, 2009: Observations of the overland reintensification of tropical storm erin (2007). *Bull. Amer. Meteor. Soc.*, **90 (8)**, 1079–1093, doi:10.1175/2009BAMS2644.1.

Ashley, S. T., and W. S. Ashley, 2008: Flood fatalities in the United States. *J. Appl. Meteor. Climatol.*, **47 (3)**, 805–818, doi:10.1175/2007JAMC1611.1.

Baker, V. R., 1975: Flood hazards along the Balcones Escarpment in central Texas alternative approaches to their recognition, mapping, and management. *Geol. Cric.*, 75–5.

Baker, V. R., 1977: Stream-channel response to floods, with examples from central Texas. *Geol. Soc. Amer. Bull.*, **88 (8)**, 1057–1071, doi:10.1130/0016-7606(1977)88⟨1057:SRTFWE⟩2.0.CO;2.

Banta, R. M., 1984: Daytime boundary-layer evolution over mountainous terrain. part 1: Observations of the dry circulations. *Mon. Wea. Rev.*, **112 (2)**, 340–356, doi:10.1175/1520-0493(1984)112⟨0340:DBLEOM⟩2.0.CO;2.

Banta, R. M., 1990: Atmospheric processes over complex terrain. *Meteor. Mongr.*, **45**, 323.

Bartels, D. L., and R. A. Maddox, 1991: Midlevel cyclonic vortices generated by mesoseale convective systems. *Mon. Wea. Rev.*, **119 (1)**, 104–118, doi:10.1175/1520-0493(1991)119⟨0104:MCVGBM⟩2.0.CO;2.

Berner, J., S.-Y. Ha, J. Hacker, A. Fournier, and C. Snyder, 2011: Model uncertainty in a mesoscale ensemble prediction system: Stochastic versus multiphysics representations. *Mon. Wea. Rev.*, **139 (6)**, 1972–1995, doi:10.1175/2010MWR3595.1.

Bluestein, H. B., and M. H. Jain, 1985: Formation of mesoscale lines of pirecipitation: Severe squall lines in Oklahoma during the spring. *J. Atmos. Sci.*, **42 (16)**, 1711–1732, doi:10.1175/1520-0469(1985)042⟨1711:FOMLOP⟩2.0.CO;2.

Bosart, L. F., and F. H. Carr, 1978: A case study of excessive rainfall centered around Wellsville, New York, 20-21 June 1972. *Mon. Wea. Rev.*, **106 (3)**, 348–362, doi:10.1175/1520-0493(1978)106⟨0348:ACSOER⟩2.0.CO;2.

Bosart, L. F., and F. Sanders, 1981: The Johnstown flood of July 1977: A long-lived convective system. *J. Atmos. Sci.*, **38 (8)**, 1616–1642, doi:10.1175/1520-0469(1981)038⟨1616:TJFOJA⟩2.0.CO;2.

Bouttier, F., B. Vié, O. Nuissier, and L. Raynaud, 2012: Impact of stochastic physics in a convection-permitting ensemble. *Mon. Wea. Rev.*, **140 (11)**, 3706–3721, doi:10.1175/MWR-D-12-00031.1.

Brennan, M. J., R. D. Knabb, M. Mainelli, and T. B. Kimberlain, 2009: Atlantic hurricane season of 2007. *Mon. Wea. Rev.*, **137 (12)**, 4061–4088, doi:10.1175/2009MWR2995.1.

Bresson, E., V. Ducrocq, O. Nuissier, D. Ricard, and C. de Saint-Aubin, 2012: Idealized numerical simulations of quasi-stationary convective systems over the northwestern mediterranean complex terrain. *Quart. J. Roy. Meteor. Soc.*, **138 (668)**, 1751–1763, doi:10.1002/qj.1911.

Bryan, G. H., J. C. Wyngaard, and J. M. Fritsch, 2003: Resolution requirements for the simulation of deep moist convection. *Mon. Wea. Rev.*, **131 (10)**, 2394–2416, doi:10.1175/1520-0493(2003)131⟨2394:RRFTSO⟩2.0.CO;2.

Burby, R. J., 2001: Flood insurance and floodplain management: the U.S. experience. *Global Environ. Change Part B: Environ. Hazards*, **3 (3)**, 111–122, doi:10.1016/S1464-2867(02)00003-7.

Caracena, F., and J. Fritsch, 1983: Focusing mechanisms in the Texas hill country flash floods of 1978. *Mon. Wea. Rev.*, **111 (12)**, 2319–2332, doi:10.1175/1520-0493(1983)111⟨2319:FMITTH⟩2.0.CO;2.

Caran, S. C., and V. R. Baker, 1986: Flooding along the Balcones Escarpment, central Texas. *The Balcones escarpment-geology, hydrology, ecology and social development in central Texas: Geological Society of America*, 1–14.

Chappell, C. F., 1986: Quasi-stationary convective events. *Mesoscale Meteorology and Forecasting*, P. S. Ray, Ed., Amer. Meteor. Soc., 289–309.

Chen, F., and J. Dudhia, 2001: Coupling an advanced land surface-hydrology model with the Penn State–NCAR MM5 modeling system. Part I: Model implementation and sensitivity. *Mon. Wea. Rev.*, **129**, 569–585, doi:10.1175/1520-0493(2001)129⟨0569:CAALSH⟩2.0.CO;2.

Cifelli, R., N. Doesken, P. Kennedy, L. D. Carey, S. A. Rutledge, C. Gimmestad, and T. Depue, 2005: The community collaborative rain, hail, and snow network: Informal education for scientists and citizens. *Bull. Amer. Meteor. Soc.*, **86 (8)**, 1069–1077, doi:10.1175/BAMS-86-8-1069.

Clark, A. J., W. A. Gallus Jr, M. Xue, and F. Kong, 2009: A comparison of precipitation forecast skill between small convection-allowing and large convection-parameterizing ensembles. *Wea. Forecasting*, **24 (4)**, 1121–1140, doi:10.1175/2009WAF2222222.1.

Clark, A. J., W. A. Gallus Jr, M. Xue, and F. Kong, 2010: Growth of spread in convection-allowing and convection-parameterizing ensembles. *Wea. Forecasting*, **25 (2)**, 594–612, doi:10.1175/2009WAF2222318.1.

Clark, A. J., and Coauthors, 2011: Probabilistic precipitation forecast skill as a function of ensemble size and spatial scale in a convection-allowing ensemble. *Mon. Wea. Rev.*, **139 (5)**, 1410–1418, doi:10.1175/2010MWR3624.1.

Corfidi, S., J. Meritt, and J. Fritsch, 1996: Predicting the movement of mesoscale convective complexes. *Wea. Forecasting*, **11 (1)**, 41–46, doi:10.1175/1520-0434(1996)011⟨0041:PTMOMC⟩2.0.CO;2.

Corfidi, S. F., 2003: Cold pools and MCS propagation: Forecasting the motion of downwind-developing mcss. *Wea. Forecasting*, **18 (6)**, 997–1017, doi:10.1175/1520-0434(2003)018⟨0997:CPAMPF⟩2.0.CO;2.

Costa, J. E., 1987: Hydraulics and basin morphometry of the largest flash floods in the conterminous United States. *J. Hydrol.*, **93 (3)**, 313–338, doi:10.1016/0022-1694(87)90102-8.

Cote, M., 2007: Predecessor rain events in advance of tropical cyclones. M.S. thesis, Department of Atmospheric and Environmental Sciences, University at Albany, State University of New York, Albany, NY, [Available online at http://cstar.cestm.albany.edu/CAP_Projects/Project10/index.htm].

Cutter, S. L., 1996: Vulnerability to environmental hazards. *Prog. Human Geogr.*, **20**, 529–539, doi:10.1177/030913259602000407.

Davis, R., and P. Jendrowski, 1998: Detecting the time duration of rainfall: A controlling factor of flash flood intensity. *Preprints Special Symposium on Hydrology, Phoenix, AZ*, 258–263.

Davis, R. S., 2001: Flash flood forecast and detection methods. *Meteor. Monogr.*, **(50)**, 481–525.

Doswell, C. A., III, 1994: Flash flood producing convective storms: current understanding and research. *Proceedings, Spain-US Joint Workshop on Natural Hazards, Barcelona, Spain.*

Doswell, C. A., III, H. E. Brooks, and R. A. Maddox, 1996: Flash flood forecasting: An ingredients-based methodology. *Wea. Forecasting*, **11 (4)**, 560–581, doi:10.1175/1520-0434(1996)011⟨0560:FFFAIB⟩2.0.CO;2.

Du, J., J. McQueen, G. DiMego, Z. Toth, D. Jovic, B. Zhou, and H.-Y. Chuang, 2006: New dimension of NCEP Short-Range Ensemble Forecasting (SREF) system: Inclusion of WRF members. *Preprints, WMO Expert Team Meeting on Ensemble Prediction System*, Exeter, United Kingdom, WMO, 5 pp.

Du, J., S. L. Mullen, and F. Sanders, 1997: Short-range ensemble forecasting of quantitative precipitation. *Mon. Wea. Rev.*, **125 (10)**, 2427–2459, doi:10.1175/1520-0493(1997)125⟨2427:SREFOQ⟩2.0.CO;2.

Du, J., and Coauthors, 2009: Ncep short-range ensemble forecast (sref) system upgrade in 2009. *Preprints, 19th Conf. on Numerical Weather Prediction and 23rd Conf. on Weather Analysis and Forecasting, Omaha, Nebraska, Amer. Meteor. Soc. Weather and Forecasting.*

Ducrocq, V., O. Nuissier, D. Ricard, C. Lebeaupin, and T. Thouvenin, 2008: A numerical study of three catastrophic precipitating events over southern France. II: Mesoscale triggering and stationarity factors. *Quart. J. Roy. Meteor. Soc.*, **134 (630)**, 131–145, doi:10.1002/qj.199.

Durran, D. R., and M. Gingrich, 2014: Atmospheric predictability: why butterflies are not of practical importance. *J. Atmos. Sci.*, **71 (7)**, 2476–2488, doi:10.1175/JAS-D-14-0007.1.

Evans, C., R. S. Schumacher, and T. J. Galarneau Jr, 2011: Sensitivity in the overland reintensification of tropical cyclone erin (2007) to near-surface soil moisture characteristics. *Mon. Wea. Rev.*, **139 (12)**, 3848–3870, doi:10.1175/2011MWR3593.1.

Fritsch, J., R. Kane, and C. Chelius, 1986: The contribution of mesoscale convective weather systems to the warm-season precipitation in the United States. *J. Climate Appl. Meteor.*, **25 (10)**, 1333–1345, doi:10.1175/1520-0450(1986)025⟨1333:TCOMCW⟩2.0.CO;2.

Fritsch, J. M., and R. Carbone, 2004: Improving quantitative precipitation forecasts in the warm season: A uswrp research and development strategy. *Bull. Amer. Meteor. Soc.*, **85 (7)**, 955–965, doi:10.1175/BAMS-85-7-955.

Fritsch, J. M., J. D. Murphy, and J. S. Kain, 1994: Warm-core vortex amplification over land. *J. Atmos. Sci.*, **51**, 1780–1807, doi:10.1175/1520-0469(1994)051⟨1780:WCVAOL⟩2.0.CO;2.

Funk, T., 2006: Heavy convective rainfall forecasting: A look at elevated convection, propagation, and precipitation efficiency. *Proc. 10th Severe Storm and Doppler Radar Conf*, Des Moines, IA, National Weather Association.

Galarneau, T. J., Jr, L. F. Bosart, and R. S. Schumacher, 2010: Predecessor rain events ahead of tropical cyclones. *Mon. Wea. Rev.*, **138 (8)**, 3272–3297, doi:10.1175/2010MWR3243.1.

Galarneau, T. J., Jr, and T. M. Hamill, 2015: Diagnosis of track forecast errors for tropical cyclone rita (2005) using gefs reforecasts. *Wea. Forecasting*, **(In Press)**, doi:10.1175/WAF-D-15-0036.1.

Gebhardt, C., S. Theis, P. Krahe, and V. Renner, 2008: Experimental ensemble forecasts of precipitation based on a convection-resolving model. *Atmos. Sci. Lett.*, **9 (2)**, 67–72, doi:10.1002/asl.177.

Gebhardt, C., S. Theis, M. Paulat, and Z. B. Bouallègue, 2011: Uncertainties in cosmo-de precipitation forecasts introduced by model perturbations and variation of lateral boundaries. *Atmospheric Research*, **100 (2)**, 168–177, doi:10.1016/j.atmosres.2010.12.008.

Gochis, D., and Coauthors, 2014: The great colorado flood of september 2013. *Bull. Amer. Meteor. Soc.*, doi:10.1175/BAMS-D-13-00241.1.

Grimit, E. P., and C. F. Mass, 2007: Measuring the ensemble spread-error relationship with a probabilistic approach: Stochastic ensemble results. *Mon. Wea. Rev.*, **135 (1)**, 203–221, doi:10.1175/MWR3262.1.

Gruntfest, E., 1977: What people did during the big thompson flood. M.S. thesis, Institute of Behavioral Science, University of Colorado Boulder, Colorado, Boulder, CO.

Hamill, T. M., 2001: Interpretation of rank histograms for verifying ensemble forecasts. *Mon. Wea. Rev.*, **129 (3)**, 550–560, doi:10.1175/1520-0493(2001)129⟨0550:IORHFV⟩2.0.CO;2.

Hamill, T. M., G. T. Bates, J. S. Whitaker, D. R. Murray, M. Fiorino, T. J. G. Jr, Y. Zhu, and W. Lapenta, 2013: NOAA's second-generation global medium-range ensemble reforecast dataset. *Bull. Amer. Meteor. Soc.*, **94 (10)**, 1553–1565, doi:10.1175/BAMS-D-12-00014.1.

Hamill, T. M., R. Hagedorn, and J. S. Whitaker, 2008: Probabilistic forecast calibration using ecmwf and gfs ensemble reforecasts. part ii: Precipitation. *Mon. Wea. Rev.*, **136 (7)**, 2620–2632, doi:10.1175/2007MWR2411.1.

Hamill, T. M., S. L. Mullen, C. Snyder, D. P. Baumhefner, and Z. Toth, 2000: Ensemble forecasting in the short to medium range: Report from a workshop. *Bull. Amer. Meteor. Soc.*, **81 (11)**, 2653–2664, doi:10.1175/1520-0477(2000)081⟨2653:EFITST⟩2.3.CO;2.

Hapuarachchi, H., Q. Wang, and T. Pagano, 2011: A review of advances in flash flood forecasting. *Hydrological Processes*, **25 (18)**, 2771–2784, doi:10.1002/hyp.8040.

Hong, S.-Y., Y. Noh, and J. Dudhia, 2006: A new vertical diffusion package with an explicit treatment of entrainment processes. *Mon. Wea. Rev.*, **134**, 2318–2341, doi: 10.1175/MWR3199.1.

Hovmöller, E., 1949: The trough-and-ridge diagram. *Tellus*, **1 (2)**, 62–66, doi:10.1111/j.2153-3490.1949.tb01260.x.

Iacono, M. J., J. S. Delamere, E. J. Mlawer, M. W. Shephard, S. A. Clough, and W. D. Collins, 2008: Radiative forcing by long-lived greenhouse gases: Calculations with the AER radiative transfer models. *J. Geophys. Res.*, **113**, D13 103, doi:10.1029/2008JD009 944, doi:10.1029/2008JD009944.

Jonkman, S., 2005: Global perspectives on loss of human life caused by floods. *Natural Hazards*, **34 (2)**, 151–175.

Junker, N. W., R. S. Schneider, and S. L. Fauver, 1999: A study of heavy rainfall events during the great midwest flood of 1993. *Wea. Forecasting*, **14 (5)**, 701–712, doi:10.1175/1520-0434(1999)014⟨0701:ASOHRE⟩2.0.CO;2.

Kain, J. S., and Coauthors, 2013: A feasibility study for probabilistic convection initiation forecasts based on explicit numerical guidance. *Bull. Amer. Meteor. Soc.*, **94 (8)**, 1213–1225, doi:10.1175/BAMS-D-11-00264.1.

Keene, K. M., and R. S. Schumacher, 2013: The bow and arrow mesoscale convective structure. *Mon. Wea. Rev.*, **141 (5)**, 1648–1672, doi:10.1175/MWR-D-12-00172.1.

Kelsch, M., 2001: Hydrometeorological characteristics of flash floods. *Coping with Flash Floods*, Springer, 181–193.

Kirshbaum, D. J., 2013: On thermally forced circulations over heated terrain. *J. Atmos. Sci.*, **70 (6)**, 1690–1709, doi:10.1175/JAS-D-12-0199.1.

Kirshbaum, D. J., and D. R. Durran, 2004: Factors governing cellular convection in orographic precipitation. *J. Atmos. Sci.*, **61 (6)**, 682–698, doi:10.1175/1520-0469(2004)061⟨0682:FGCCIO⟩2.0.CO;2.

Knabb, R. D., 2008: Tropical Storm Erin. National Hurricane Center Tropical Cyclone Report AL052007, 17 pp. [Available online at http://www.nhc.noaa.gov/pdf/TCR-AL052007_Erin.pdf].

Lawson, J., and J. Horel, 2015: Ensemble forecast uncertainty of the 1 December 2011 Wasatch windstorm. *Wea. Forecasting*, **(In Press)**, doi:10.1175/WAF-D-15-0034.1.

Lean, H. W., N. M. Roberts, P. A. Clark, and C. Morcrette, 2009: The surprising role of orography in the initiation of an isolated thunderstorm in southern England. *Mon. Wea. Rev.*, **137 (9)**, 3026–3046, doi:10.1175/2009MWR2743.1.

Leary, M. R., R. Bednarski, D. Hammon, and T. Duncan, 1997: Blowhards, snobs, and narcissists. *Aversive interpersonal behaviors*, Springer, 111–131.

Leith, C., 1971: Atmospheric predictability and two-dimensional turbulence. *J. Atmos. Sci.*, **28 (2)**, 145–161, doi:10.1175/1520-0469(1971)028⟨0145:APATDT⟩2.0.CO;2.

Leith, C., and R. Kraichnan, 1972: Predictability of turbulent flows. *J. Atmos. Sci.*, **29 (6)**, 1041–1058, doi:10.1175/1520-0469(1972)029⟨1041:POTF⟩2.0.CO;2.

Lewis, J. M., 2005: Roots of ensemble forecasting. *Mon. Wea. Rev.*, **133 (7)**, 1865–1885, doi:10.1175/MWR2949.1.

Lin, Y., and K. E. Mitchell, 2005: The NCEP Stage II/IV hourly precipitation analyses: development and applications. *Preprints, 19th Conference on Hydrology*, San Diego, CA, Amer. Meteor. Soc., [Available online at http://ams.confex.com/ams/pdfpapers/83847.pdf].

Lorenz, E. N., 1963: Deterministic nonperiodic flow. *J. Atmos. Sci.*, **20 (2)**, 130–141, doi: 10.1175/1520-0469(1963)020⟨0130:DNF⟩2.0.CO;2.

Lorenz, E. N., 1969: The predictability of a flow which possesses many scales of motion. *Tellus A*, **21 (3)**.

Lorenz, E. N., 1996: Predictability: A problem partly solved. *Proc. Seminar on predictability*, Reading, United Kingdom, Vol. 1.

Maddox, R. A., and G. K. Grice, 1986: The austin, texas, flash flood: An examination from two perspectives-forecasting and research. *Wea. Forecasting*, **1 (1)**, 66–76, doi:10.1175/1520-0434(1986)001⟨0066:TATFFA⟩2.0.CO;2.

Maddox, R. A., L. R. Hoxit, C. F. Chappell, and F. Caracena, 1978: Comparison of meteorological aspects of the Big Thompson and Rapid City flash floods. *Mon. Wea. Rev.*, **106 (3)**, 375–389, doi:10.1175/1520-0493(1978)106⟨0375:COMAOT⟩2.0.CO;2.

Markowski, P., and Y. Richardson, 2010: *Mesoscale meteorology in midlatitudes*. John Wiley & Sons.

Martin, P. L., and R. Edwards, 1995: A severe weather, hurricane, and flood climatology for the Austin/San Antonio WFO county warning area. NOAA Tech. Memo. NWS SR-167.

Melhauser, C., and F. Zhang, 2012: Practical and intrinsic predictability of severe and convective weather at the mesoscales. *J. Atmos. Sci.*, **69 (11)**, 3350–3371, doi:10.1175/JAS-D-11-0315.1.

Mesinger, F., and Coauthors, 2006: North American regional reanalysis. *Bull. Amer. Meteor. Soc.*, **87 (3)**, 343–360, doi:10.1175/BAMS-87-3-343.

Métais, O., and M. Lesieur, 1986: Statistical predictability of decaying turbulence. *J. Atmos. Sci.*, **43 (9)**, 857–870, doi:10.1175/1520-0469(1986)043⟨0857:SPODT⟩2.0.CO;2.

Molteni, F., R. Buizza, T. N. Palmer, and T. Petroliagis, 1996: The ecmwf ensemble prediction system: Methodology and validation. *Quart. J. Roy. Meteor. Soc.*, **122 (529)**, 73–119, doi:10.1002/qj.49712252905.

Moore, B. J., L. F. Bosart, D. Keyser, and M. L. Jurewicz, 2013: Synoptic-scale environments of predecessor rain events occurring east of the Rocky Mountains in association with Atlantic basin tropical cyclones*. *Mon. Wea. Rev.*, **141 (3)**, 1022–1047, doi:10.1175/MWR-D-12-00178.1.

Moore, J. T., F. H. Glass, C. E. Graves, S. M. Rochette, and M. J. Singer, 2003: The environment of warm-season elevated thunderstorms associated with heavy rainfall over the central united states. *Wea. Forecasting*, **18 (5)**, 861–878, doi:10.1175/1520-0434(2003)018⟨0861:TEOWET⟩2.0.CO;2.

Morales, A., R. S. Schumacher, and S. M. Kreidenweis, 2015: Mesoscale vortex development during extreme precipitation: Colorado, September 2013. *Mon. Wea. Rev.*, In Press, doi:10.1175/MWR-D-15-0086.1.

Morrison, H. G., G. Thompson, and V. Tatarskii, 2009: Impact of cloud microphysics on the development of trailing stratiform precipitation in a simulated squall line: Comparison of one- and two-moment schemes. *Mon. Wea. Rev.*, **137**, 991–1007, doi:10.1175/2008MWR2556.1.

Mullen, S. L., and R. Buizza, 2001: Quantitative precipitation forecasts over the united states by the ecmwf ensemble prediction system. *Mon. Wea. Rev.*, **129 (4)**, 638–663, doi:10.1175/1520-0493(2001)129⟨0638:QPFOTU⟩2.0.CO;2.

Nielsen-Gammon, J. W., F. Zhang, A. M. Odins, and B. Myoung, 2005: Extreme rainfall in Texas: Patterns and predictability. *Phys. Geogr.*, **26 (5)**, 340–364, doi:10.2747/0272-3646.26.5.340.

NOAA, 2007: *Storm Data*, Vol. 49, No. 8. 530 pp.

NOAA, cited 2015a: National Weather Service glossary. [Available online at http://w1.weather.gov/glossary/].

NOAA, cited 2015b: Storm events database. [Available online at http://www.ncdc.noaa.gov/stormevents/].

NOAA, cited 2015c: Storm Prediction Center sounding climatology page. [Available online at http://www.spc.noaa.gov/exper/soundingclimo/].

Novak, D. R., C. Bailey, K. Brill, M. Eckert, D. Petersen, R. Rausch, and M. Schichtel, 2011: Human improvement to numerical weather prediction at the hydrometeorological prediction center. *91th Annual AMS Meeting, AMS 24th Conference on Weather and Forecasting/20th Conference on Numerical Weather Prediction*, [Available online at https://ams.confex.com/ams/91Annual/webprogram/Manuscript/Paper181989/HumanNWP_final.pdf].

Nutter, P., D. Stensrud, and M. Xue, 2004a: Effects of coarsely resolved and temporally interpolated lateral boundary conditions on the dispersion of limited-area ensemble forecasts. *Mon. Wea. Rev.*, **132 (10)**, 2358–2377, doi:10.1175/1520-0493(2004)132⟨2358:EOCRAT⟩2.0.CO;2.

Nutter, P., M. Xue, and D. Stensrud, 2004b: Application of lateral boundary condition perturbations to help restore dispersion in limited-area ensemble forecasts. *Mon. Wea. Rev.*, **132 (10)**, 2378–2390, doi:10.1175/1520-0493(2004)132⟨2378:AOLBCP⟩2.0.CO;2.

NWS, 1999: Service assessment: South Texas Floods October 17-22, 1998. National Weather Service, [Available online at http://www.nws.noaa.gov/om/assessments/pdfs/txflood.pdf].

O'Connor, J. E., and J. E. Costa, 2004: Spatial distribution of the largest rainfall-runoff floods from basins between 2.6 and 26,000 km^2 in the United States and Puerto Rico. *Water Resour. Res.*, **40 (1)**, doi:10.1029/2003WR002247.

Parker, M. D., and R. H. Johnson, 2000: Organizational modes of midlatitude mesoscale convective systems. *Mon. Wea. Rev.*, **128 (10)**, 3413–3436, doi:10.1175/1520-0493(2001)129⟨3413:OMOMMC⟩2.0.CO;2.

Patton, P. C., and V. R. Baker, 1976: Morphometry and floods in small drainage basins subject to diverse hydrogeomorphic controls. *Water Resour. Res.*, **12 (5)**, 941–952, doi:10.1029/WR012i005p00941.

Petersen, W. A., and Coauthors, 1999: Mesoscale and radar observations of the Fort Collins flash flood of 28 july 1997. *Bull. Amer. Meteor. Soc.*, **80 (2)**, 191–216, doi:10.1175/1520-0477(1999)080⟨0191:MAROOT⟩2.0.CO;2.

Pielke Jr, R. A., and M. W. Downton, 2000: Precipitation and damaging floods: Trends in the United States, 1932-97. *J. Climate*, **13 (20)**, 3625–3637, doi:10.1175/1520-0442(2000)013⟨3625:PADFTI⟩2.0.CO;2.

Pontrelli, M. D., G. Bryan, and J. Fritsch, 1999: The Madison County, Virginia, flash flood of 27 june 1995. *Wea. Forecasting*, **14 (3)**, 384–404, doi:10.1175/1520-0434(1999)014⟨0384:TMCVFF⟩2.0.CO;2.

Rappaport, E. N., 2000: Loss of life in the United States associated with recent Atlantic tropical cyclones. *Bull. Amer. Meteor. Soc.*, **81 (9)**, 2065–2073, doi:10.1175/1520-0477(2000)081⟨2065:LOLITU⟩2.3.CO;2.

Rappaport, E. N., 2014: Fatalities in the United States from Atlantic tropical cyclones: new data and interpretation. *Bull. Amer. Meteor. Soc.*, **95 (3)**, 341–346.

Raymond, D., and H. Jiang, 1990: A theory for long-lived mesoscale convective systems. *J. Atmos. Sci.*, **47 (24)**, 3067–3077, doi:10.1175/1520-0469(1990)047⟨3067:ATFLLM⟩2.0.CO;2.

Schumacher, R. S., and A. J. Clark, 2014: Evaluation of ensemble configurations for the analysis and prediction of heavy-rain-producing mesoscale convective systems*. *Mon. Wea. Rev.*, **142 (11)**, 4108–4138, doi:10.1175/MWR-D-13-00357.1.

Schumacher, R. S., A. J. Clark, M. Xue, and F. Kong, 2013: Factors influencing the development and maintenance of nocturnal heavy-rain-producing convective systems in a storm-scale ensemble. *Mon. Wea. Rev.*, **141 (8)**, 2778–2801, doi:10.1175/MWR-D-12-00239.1.

Schumacher, R. S., and C. A. Davis, 2010: Ensemble-based forecast uncertainty analysis of diverse heavy rainfall events. *Wea. Forecasting*, **25 (4)**, 1103–1122, doi:10.1175/2010WAF2222378.1.

Schumacher, R. S., and T. J. Galarneau, Jr, 2012: Moisture transport into midlatitudes ahead of recurving tropical cyclones and its relevance in two predecessor rain events. *Mon. Wea. Rev.*, **140 (6)**, 1810–1827, doi:10.1175/MWR-D-11-00307.1.

Schumacher, R. S., T. J. Galarneau, Jr, and L. F. Bosart, 2011: Distant effects of a recurving tropical cyclone on rainfall in a midlatitude convective system: A high-impact predecessor rain event*. *Mon. Wea. Rev.*, **139 (2)**, 650–667, doi:10.1175/2010MWR3453.1.

Schumacher, R. S., and R. H. Johnson, 2005: Organization and environmental properties of extreme-rain-producing mesoscale convective systems. *Mon. Wea. Rev.*, **133**, 961–976, doi:10.1175/MWR2899.1.

Schumacher, R. S., and R. H. Johnson, 2006: Characteristics of United States extreme rain events during 1999–2003. *Wea. Forecasting*, **21**, 69–85, doi:10.1175/WAF900.1.

Schumacher, R. S., and R. H. Johnson, 2008: Mesoscale processes contributing to extreme rainfall in a midlatitude warm-season flash flood*. *Mon. Wea. Rev.*, **136 (10)**, 3964–3986, doi:10.1175/2008MWR2471.1.

Schumacher, R. S., and R. H. Johnson, 2009: Quasi-stationary, extreme-rain-producing convective systems associated with midlevel cyclonic circulations. *Wea. Forecasting*, **24**, 555–574, doi:10.1175/2008WAF2222173.1.

Schumacher, R. S., D. M. Schultz, and J. A. Knox, 2015: Influence of terrain resolution on banded convection in the lee of the rocky mountains. *Mon. Wea. Rev.*, **143 (4)**, 1399–1416, doi:10.1175/MWR-D-14-00255.1.

Schwartz, C. S., G. S. Romine, K. R. Smith, and M. L. Weisman, 2014: Characterizing and optimizing precipitation forecasts from a convection-permitting ensemble initialized by a mesoscale ensemble kalman filter. *Wea. Forecasting*, **29 (6)**, 1295–1318, doi:10.1175/WAF-D-13-00145.1.

Schwartz, C. S., G. S. Romine, R. A. Sobash, K. R. Fossell, and M. L. Weisman, 2015: NCAR's experimental real-time convection-allowing ensemble prediction system. *Weather and Forecasting*, **(2015)**, doi:10.1175/WAF-D-15-0103.1.

Schwartz, C. S., and Coauthors, 2010: Toward improved convection-allowing ensembles: Model physics sensitivities and optimizing probabilistic guidance with small ensemble membership. *Wea. Forecasting*, **25 (1)**, 263–280, doi:10.1175/2009WAF2222267.1.

Sharif, H. O., T. Jackson, M. Hossain, S. Bin-Shafique, and D. Zane, 2010: Motor vehicle-related flood fatalities in Texas, 1959–2008. *J. Trasnsp. Saf. Secur.*, **2 (4)**, 325–335, doi:10.1080/19439962.2010.506596.

Sharif, H. O., T. L. Jackson, M. M. Hossain, and D. Zane, 2015: Analysis of flood fatalities in Texas. *Natural Hazards Rev.*, **16 (1)**, doi:10.1061/(ASCE)NH.1527-6996.0000145.

Skamarock, W., and Coauthors, 2008: A description of the advanced research WRF version 3. NCAR Tech. Note NCAR/TN–475+STR, [Available online at http://www.mmm.ucar.edu/wrf/users/docs/arw_v3.pdf] pp.

Smith, J. A., M. L. Baeck, J. E. Morrison, and P. Sturdevant-Rees, 2000: Catastrophic rainfall and flooding in Texas. *J. Hydrometeor.*, **1 (1)**, 5–25, doi:10.1175/1525-7541(2000)001⟨0005:CRAFIT⟩2.0.CO;2.

Smith, R., 1982: A differential model of thermal advection. *Mon. Wea. Rev.*, **110**, 306–309.

Soderholm, B., B. Ronalds, and D. J. Kirshbaum, 2014: The evolution of convective storms initiated by an isolated mountain ridge. *Mon. Wea. Rev.*, **142 (4)**, 1430–1451, doi:10.1175/MWR-D-13-00280.1.

Špitalar, M., J. J. Gourley, C. Lutoff, P.-E. Kirstetter, M. Brilly, and N. Carr, 2014: Analysis of flash flood parameters and human impacts in the US from 2006 to 2012. *J. Hydrol.*, **519, Part A (0)**, 863 – 870, doi:10.1016/j.jhydrol.2014.07.004.

Srock, A. F., and L. F. Bosart, 2009: Heavy precipitation associated with southern Appalachian cold-air damming and Carolina coastal frontogenesis in advance of weak landfalling tropical storm Marco (1990). *Mon. Wea. Rev.*, **137 (8)**, 2448–2470, doi:10.1175/2009MWR2819.1.

Stevenson, S. N., and R. S. Schumacher, 2014: A 10-year survey of extreme rainfall events in the central and eastern united states using gridded multisensor precipitation analyses. *Mon. Wea. Rev.*, **142 (9)**, 3147–3162, doi:10.1175/MWR-D-13-00345.1.

Sweeney, T. L., 1992: Modernized areal flash flood guidance. NOAA Tech. Memo. NWS HYDRO 44, 32 pp.

Thompson, P. D., 1957: Uncertainty of initial state as a factor in the predictability of large scale atmospheric flow patterns. *Tellus*, **9 (3)**, 275–295, doi:0.1111/j.2153-3490.1957.tb01885.x.

Trier, S., C. Davis, and W. Skamarock, 2000a: Long-lived mesoconvective vortices and their environment. part ii: Induced thermodynamic destabilization in idealized simulations. *Mon. Wea. Rev.*, **128 (10)**, 3396–3412, doi:10.1175/1520-0493(2000)128⟨3396:LLMVAT⟩2.0.CO;2.

Trier, S., C. Davis, and J. Tuttle, 2000b: Long-lived mesoconvective vortices and their environment. part i: Observations from the central united states during the 1998 warm season. *Mon. Wea. Rev.*, **128 (10)**, 3376–3395, doi:10.1175/1520-0493(2000)128⟨3376:LLMVAT⟩2.0.CO;2.

Trier, S. B., and C. A. Davis, 2002: Influence of balanced motions on heavy precipitation within a long-lived convectively generated vortex. *Mon. Wea. Rev.*, **130 (4)**, 877–899, doi:10.1175/1520-0493(2002)130⟨0877:IOBMOH⟩2.0.CO;2.

Trier, S. B., C. A. Davis, and W. C. Skamarock, 2000c: Long-lived mesoconvective vortices and their environment. Part II: Induced thermodynamic destabilization in idealized simulations. *Mon. Wea. Rev.*, **128**, 3396–3412, doi:10.1175/1520-0493(2000)128⟨3396:LLMVAT⟩2.0.CO;2.

Trier, S. B., C. A. Davis, and J. D. Tuttle, 2000d: Long-lived mesoconvective vortices and their environment. Part I: Observations from the central United States during the 1998 warm season. *Mon. Wea. Rev.*, **128**, 3376–3395, doi:10.1175/1520-0493(2000)128⟨3376:LLMVAT⟩2.0.CO;2.

Tuttle, J. D., and C. A. Davis, 2006: Corridors of warm season precipitation in the central United States. *Mon. Wea. Rev.*, **134 (9)**, 2297–2317, doi:10.1175/MWR3188.1.

Uccellini, L. W., and D. R. Johnson, 1979: The coupling of upper and lower tropospheric jet streaks and implications for the development of severe convective storms. *Mon. Wea. Rev.*, **107 (6)**, 682–703, doi:10.1175/1520-0493(1979)107⟨0682:TCOUAL⟩2.0.CO;2.

Vié, B., O. Nuissier, and V. Ducrocq, 2011: Cloud-resolving ensemble simulations of Mediterranean heavy precipitating events: uncertainty on initial conditions and lateral boundary conditions. *Mon. Wea. Rev.*, **139 (2)**, 403–423, doi:10.1175/2010MWR3487.1.

Weckwerth, T. M., L. J. Bennett, L. Jay Miller, J. Van Baelen, P. Di Girolamo, A. M. Blyth, and T. J. Hertneky, 2014: An observational and modeling study of the processes leading to deep, moist convection in complex terrain. *Mon. Wea. Rev.*, **142 (8)**, 2687–2708, doi: 10.1175/MWR-D-13-00216.1.

Xue, M., and Coauthors, 2007: CAPS realtime storm-scale ensemble and high-resolution forecasts as part of the NOAA Hazardous Weather Testbed 2007 spring experiment. *Extended Abstracts, 22nd Conference on Weather Analysis and Forecasting/18th Conference on Numerical Weather Prediction*, Park City, UT, Amer. Meteor. Soc., [Available online at http://ams.confex.com/ams/pdfpapers/124587.pdf].

Xue, M., and Coauthors, 2010: CAPS realtime storm scale ensemble and high resolution forecasts for the NOAA Hazardous Weather Testbed 2010 spring experiment. *Extended Abstracts, 25th Conference on Severe Local Storms*, Denver, CO, Amer. Meteor. Soc., [Available online at https://ams.confex.com/ams/pdfpapers/176056.pdf].

Xue, M., and Coauthors, 2011: Realtime convection-permitting ensemble and convection-resolving deterministic forecasts of CAPS for the Hazardous Weather Testbed 2010 spring experiment. *Extended Abstracts, 24th Conference on Weather Analysis and Forecasting/20th Conference on Numerical Weather Prediction*, Seattle, WA, Amer. Meteor. Soc., [Available online at https://ams.confex.com/ams/91Annual/webprogram/Manuscript/Paper183227/Xue_CAPS_2011_SpringExperiment_24thWAF20thNWP_ExtendedAbstract.pdf].

Zhang, F., 2005: Dynamics and structure of mesoscale error covariance of a winter cyclone estimated through short-range ensemble forecasts. *Mon. Wea. Rev.*, **133 (10)**, 2876–2893, doi:10.1175/MWR3009.1.

Zhang, F., N. Bei, R. Rotunno, C. Snyder, and C. C. Epifanio, 2007: Mesoscale predictability of moist baroclinic waves: Convection-permitting experiments and multistage error growth dynamics. *J. Atmos. Sci.*, **64 (10)**, 3579–3594, doi:10.1175/JAS4028.1.

Zhang, F., A. M. Odins, and J. W. Nielsen-Gammon, 2006: Mesoscale predictability of an extreme warm-season precipitation event. *Wea. Forecasting*, **21 (2)**, 149–166, doi:10.1175/WAF909.1.

Zhang, F., C. Snyder, and R. Rotunno, 2002: Mesoscale predictability of the surprise snowstorm of 24-25 January 2000. *Mon. Wea. Rev.*, **130 (6)**, 1617–1632, doi:10.1175/1520-0493(2002)130⟨1617:MPOTSS⟩2.0.CO;2.

Zhang, F., C. Snyder, and R. Rotunno, 2003: Effects of moist convection on mesoscale predictability. *J. Atmos. Sci.*, **60 (9)**, 1173–1185, doi:10.1175/1520-0469(2003)060⟨1173:EOMCOM⟩2.0.CO;2.